HIGH DEPTH RESOLUTION RUTHERFORD BACKSCATTERING SPECTROMETRY WITH A MAGNET SPECTROMETER: IMPLEMENTATION AND APPLICATION TO THIN FILM ANALYSIS

CHAN TAW KUEI

(BSc. , NUS)

A THESIS SUBMITTED
FOR THE DEGREE OF DOCTOR OF PHILOSOPHY

DEPARTMENT OF PHYSICS

NATIONAL UNIVERSITY OF SINGAPORE

2009

Acknowledgements

It was with the help and support from many people that this thesis is made possible. I would first like to thank my supervisors Associate Professor Thomas Osipowicz and Professor Frank Watt. I am immensely grateful to the advice and guidance given to me by Prof Thomas Osipowicz, who gave me the opportunity to work in this project and literally taught me everything that I know in this field of research. I also thank Prof Frank Watt, for establishing the Centre for Ion Beam Applications (CIBA) and making this project possible. I am also indebted to Mr T. F. Choo for his invaluable help with the laboratory equipment and operations, without whom my experimental data could not have been collected.

Next, I would like to thank my collaborators Mr. Peter Darmawan and Dr. P. S. Lee from the School of Material Science and Engineering, Nanyang Technological University of Singapore for providing me with the ultra-thin Lu_2O_3/Si films.

I would also like to take this opportunity to thank Dr. P. Malar and Mr C. S. Ho Brandon from CIBA for their invaluable help. In particular, I am very grateful to Brandon for his friendship, discussions and help with my research. My thanks also go out to all members in CIBA who provided me with assistance and guidance in any way during the course of my candidature and this thesis.

I also wish to thank my friends – Greg and San Hua for their advice – as well as my family. I am in particularly indebted to my father, who brought me up and saw me

through all these long years of education. It was ultimately through him that made this work possible.

Finally, my most special thanks go to my wife, Li, for her constant love and support through my long, winding journey. It was only with her invaluable help that allowed me to start on this course and it was because of her love that I made it through at all. I dedicate this work to her.

Chan Taw Kuei

詹道揆

February 2009

Table of Contents

Acknowledgements ……ii

Summary ……..viii

List of Acronyms……..x

List of Publications……xii

List of Figures……xiv

Chapter 1 ……..…… 1

1.1 High-resolution Rutherford Backscattering Spectrometry ……...……1

1.2 Spectrometer ion optics studies and MCP gain correction ...……2

1.3 Gate dielectrics research ……...3

1.4 Analysis of Lu_2O_3 ultra-thin films with HRBS in CIBA ……..5

1.5 Structure of this thesis ……...6

Chapter 2 ……...……..7

2.1 Introduction ……...7

2.2 Overview of RBS physical concepts ……7

2.2.1 Kinematic factor ……9

2.2.2 Rutherford scattering cross-section ……12

2.2.3 Stopping cross-section ……17

2.2.4 Energy straggling ……21

2.3 Rutherford Backscattering Spectrometry ……24

2.3.1 Thick elemental substrates ……..25

2.3.2 Thin film systems ……27

2.3.3 Effects of straggling in RBS spectra ……...29

2.3.4 Numerical simulation of RBS spectra using SIMNRA ……...30

Chapter 3 ……...……32

3.1 CIBA Facilities ……...32

3.2 Singletron^{TM} accelerator …….33

3.2.1 RF Ion source ……..34

3.2.2 High voltage power supply ……..34

3.2.3 High voltage insulation and Electron suppression ……..36

3.3 Beam steering and stabilization ……..36

3.4 HRBS Endstation ……38

3.4.1 Main chamber, load lock and vacuum system ……40

3.4.2 Goniometer ……42

3.4.3 Control cabinet ……43

3.5 HRBS Detection system ……44

3.5.1 Micro-Channel Plate ……45

3.5.2 Focal Plane Detector and HRBS electronics ……...46

Chapter 4 …….....48

4.1 Introduction ……48

4.2 HRBS Spectrometer magnet ……...49

4.3 Overall layout of the HRBS detection system ……50

4.4 Effect of curvature of spectrometer exit edge ……51

4.5 Analytical studies of spectrometer ion optics ……53

4.5.1 Beam Entry parameters ……...54

4.5.2 Fringe field correction ……55

4.5.3 Direct calculations ……...57

4.5.4 Matrix calculations ……..61

4.5.5 Comparison of results from Direct and Matrix calculations ……...68

4.6 Numerical simulation of ion trajectories using SIMION ……69

4.6.1 Drawing the magnet ……69

4.6.2 Maxwell's and Laplace's equations ……71

4.6.3 Refining the magnet array ……...72

4.6.4 Calculation of ion trajectories ……74

4.6.5 Numerical integration of acceleration components ……75

4.6.6 Simulation details ……76

4.7 Experimental data using a HRBS calibration run ……...78

4.7.1 Calibration experimental details ……..79

4.8 Direct, Matrix, Numerical calculations and Experimental data ……81

4.9 Conclusion ……..81

Chpater 5 ……..……..……82

5.1 Introduction ……82

5.2 Consistency of HRBS Calibration process ……82

5.3 Conversion of position spectra into energy spectra (FORBIN) ……..86

5.3.1 Energy spectrum form multiple windows of position spectra …….87

5.3.2 Generating the required lists ……89

5.3.3 Re-binning process ……..91

5.3.4 Fragment scaling ……92

5.4 Spectrum conversion using software programs ……92

5.5 Comparison of results from FORBIN and CompoundSP ……..95

5.6 MCP Gain correction ……96

5.6.1 Reverse-binning process (REVBIN) ……..96

5.6.2 Installation of electrostatic plates ……..100

5.6.3 Methods of gain variation characterization ……...102

5.6.4 MCP Gain characterization using thick Au / Ni standard ……103

5.6.5 MCP Gain correction ……105

Chapter 6 …….……110

6.1 Equivalent Oxide Thickness (EOT) ……..110

6.2 Film deposition using Pulsed Laser Deposition ……...111

6.3 Elemental depth profiling of Lu_2O_3/Si film and interface …...…....…..111

6.3.1 Experimental ……111

6.3.2 Depth profiling results ……..112

6.4 Interfacial lattice strain measurement with HRBS channeling ……115

6.4.1 Ion channeling within a crystal ……115

6.4.2 Estimation of lattice strain ……118

6.5 Conclusion ……122

Chapter 7 …….……123

7.1 Conclusion ……123

7.2 Future directions ……...124

Bibliography ……126

Appendices ……..……131

A1 Central force elastic binary scattering in CM frame ……131

A2 Conversion of scattering cross-section from CM to Lab frame ……133

A3 Impulse approximation ……135

Summary

The rapid miniaturization of electronic devices in recent years has caused the thicknesses of thin films in modern semiconductor research to be reduced to the regime of tens of angstroms. Conventional Rutherford Backscattering Spectrometry (RBS) can no longer provide depth profiling for thin films with such thicknesses. The High-resolution RBS (HRBS) endstation in CIBA offers thin film depth profiling and lattice strain analysis with sub-nanometer resolution through a more complicated detection system. Energy detection involves a spectrometer magnet and a Micro-Channel Plate-Focal Plane Detector (MCP-FPD) assembly. Backscattered ions are sorted according to their momentum by the spectrometer before their incidence on the MCP-FPD at the focal plane. The MCP-FPD and the HRBS electronics subsequently assign energy to each incident backscattered ion according to their position of incidence.

The non-linear energy-analyzing process of the spectrometer determines the position of incidence of each backscattered ion along the MCP-FPD, and hence its assigned energy. It is therefore important for the spectrometer ion optics to be carefully studied to ensure that the energy-analyzing process is consistent with theoretical and design expectations. In this thesis, analytical and numerical studies were conducted and their results compared to the actual response of the spectrometer magnet. The MCP utilizes an electron-multiplication process within micro-channels to amplify the signal generated by the incidence of every backscattering ion. However, different parts of the MCP might have different overall gain per ion incidence event, due to variations in the electron-multiplication gain and the gap between the MCP and FPD, generating

false signals in the output spectra. A novel method has been developed as part of this thesis to correct for this gain variation along the length of the MCP.

The rapid down-scaling of Metal-Oxide Field Emission Transistors (MOSFETs) have caused the required thickness of the traditional SiO_2 gate dielectric to reach sub-nanometer regime, where direct quantum tunneling of electrons through the dielectric causes unacceptable levels of gate leakage current. Thicker dielectric materials with higher dielectric constants (high-k dielectrics) must be employed so as to reduce the leakage current yet retain the same capacitative density as a layer of SiO_2 with a much smaller thickness. Among the candidates for alternative high-k dielectrics, quantum tunneling calculations have shown that the Lanthanide oxides have one of the smallest ultimate scaling limits. Lutetium oxide (Lu_2O_3) has the largest lattice energy and band gap among the lanthanide oxides, and is therefore expected to show higher thermal stability and hygroscopic immunity. In last part of this thesis, ultra-thin Lu_2O_3/Si films under different temperatures of anneal were characterized using HRBS depth profiling. Surface Si is found in annealed samples, and a rough interface region exists for all films. Channeling analysis also indicates that the Lu_2O_3 film imposes a tensile lattice strain in the Si lattice at the film-substrate interface. The lattice strain magnitude is largest in the as-deposited sample and decreases with annealing temperature.

List of Acronyms

AC	Alternating Current
BPM	Beam Profile Monitor
CIBA	Centre for Ion Beam Application
CM	Centre of Mass
CMOS	Complementary Metal Oxide Semiconductor
CPU	Capacitative Pickup Unit
EOT	Equivalent Oxide Thickness
FPD	Focal Plane Detector
FWHM	Full Width at Half Maximum
GVM	Generating Voltmeter
High-k	High-Dielectric constant
HRBS	High-Resolution Backscattering Spectrometry
HVE	High Voltage Engineering
HVEE	High Voltage Engineering Europa
Lab	Laboratory
MCA	Multi-Channel Analyzer
MCP	Micro-Channel Plate
MOSFET	Metal Oxide Semiconductor Field Emission Transistor
NUS	National University of Singapore
PIPS	Passivated Implanted Planar Silicon
PLD	Pulsed Laser Deposition
PSDA	Position Sensitive Detector Analyzer
RBS	Rutherford Backscattering Spectrometry

RCA	Radio Corporation of America
RF	Radio Frequency
RTA	Rapid Thermal Annealing
SIMS	Secondary Ion Mass Spectrometry
TMP	Turbo-Molecular Pump

List of Publications

1. *Interfacial Strain Study of thin Lu_2O_3 / Si using HRBS*
   T.K. Chan, P. Darmawan, C.S. Ho, P. Malar, P.S. Lee, T. Osipowicz.
   Nuclear Instruments and Methods in Physics Research B **266** (2008) 1486

2. *Lu_2O_3 / Al_2O_3 gate dielectrics for germanium metal-oxide-semiconductor devices*
   P. Darmawan, M. Y. Chan, T. Zhang, Y. Setiawan, H. L. Seng, **T. K. Chan**, T. Osipowicz, P. S. Lee
   Applied Physics Letters **93** (2008) 062901

3. *HRBS Channeling studies of ultra-thin ITO films on Si*
   P. Malar, **T.K. Chan**, C.S. Ho, T. Osipowicz
   Nuclear Instruments and Methods in Physics Research B **266** (2008) 1464

4. *Realization of silicon-germanium-tin (SiGeSn) source / drain stressors by Sn implant and solid phase epitaxy for strain engineering in SiGe channel P-MOSFETs*
   G. H. Wang, E. H. Toh, **T. K. Chan**, T. Osipowicz, Y. L. Foo, C. H. Tung, G. Q. Lo, G. Samudra, and Y. C. Yeo
   International Symposium on VLSI Technology, Systems and Applications (2008) 128

5. *Quantitative studies of copper diffusion through ultra-thin ALD tantalum nitride barrier films by High resolution-RBS*
   C.S Ho, S. L. Liew, **T. K. Chan**, P. Malar, T. Osipowicz, L. Lu, C.Y.H. Lima
   Advanced Metallization Conference 2007 (AMC 2007) 95

6. *Structural, magnetic and transport investigations of CrTe clustering effect in (Zn,Cr)Te system*
   M. G. Sreenivasan, K. L. Teo, X. Z. Cheng, M. B. A. Jalil, T. Liew, and T. C. Chong, A. Y. Du, **T. K. Chan** and T. Osipowicz
   Journal Of Applied Physics **102** (2007) 053702

7. *Channeling contrast microscopy of epitaxial lateral overgrowth of ZnO/GaN films*
   H. Zhou, H. Pan, **T. K. Chan**, C. S. Ho, Y. Feng, S. J. Chua, T. Osipowicz
   Nuclear Instruments and Methods in Physics Research B **260** (2007) 299

8. *Silicon-Germanium-Tin (SiGeSn) Source and Drain Stressors formed by Sn Implant and Laser Annealing for Strained Silicon-Germanium Channel P-MOSFETs*
   G.H. Wang, E. H. Toh, X. Wang, D.H.L. Seng, S. Tripathy, T. Osipowicz, **T. K. Chan**, K. M. Hoe, S. Balakumar, C. H. Tung; G. Q. Lo; G. Samudra, Y. C. Yeo
   IEEE Electron Devices Meeting 2007 IEDM (2007) 131

9. *Strained SiGeSn formed by Sn implant into SiGe and pulsed laser annealing*
   G. H. Wang, E. H. Toh, X. Wang, S. Tripathy, T. Osipowicz, **T. K. Chan**, K. M. Hoe, S. Balakumar, G. Q. Lo, G. Samudra and Y. C. Yeo
   Applied Physics Letters **91** (2007) 202105

10. *The CIBA high resolution RBS facility*
    T. Osipowicz , H.L. Seng, **T.K. Chan**, B. Ho
    Nuclear Instruments and Methods in Physics Research B **249** (2006) 915

List of Figures

1.1 MOSFET schematic……... 3

1.2 (a) Plot of direct tunneling current J_G through various high-k dielectrics vs EOT for a fixed applied gate voltage. (b) Plot of the scaling limit (EOT) of various dielectrics vs acceptable leakage current through the layer. Source: [7]……. 4

2.1 Elastic collision diagrams as seen in the (a) lab reference frame (b) CM reference frame. Source: [22]…….. 9

2.2 Scattering of an incident ion with impact parameter between b and db into an angular region between θ_c and $\theta_c + \mathrm{d}\theta_c$ in the CM reference frame. Source: [22]……. 12

2.3 Plot of $F(\theta_c, E_c)$ vs θ_c. Correction magnitude increases rapidly at small θ_c and decreases with increasing E_0 at large θ_c. Source: [25]……... 17

2.4 Plot of Chu correction factors H vs Z_2 for various E/M_1 values. Dots are original data from Chu, while lines are extrapolations by Szilágyi [30]. Source:[22]…….. 23

2.5 General layout of typical RBS measurement…….. 24

2.6 (a) Scattering geometry and (b) spectrum of an RBS measurement of a thick, elemental target…….. 25

2.7 (a) Scattering geometry and (b) spectrum of an RBS measurement of a thin compound target……... 27

2.8 Normalized elemental signal in a RBS spectrum where (a) the conditions are perfect, (b) there is influence from straggling only and (c) there are influences from both system resolution and beam straggling. Source: [32]…… 29

2.9 Schematic of the target divided into thin sublayers……..... 30

3.1 Layout of the accelerator and beamlines…… 33

3.2 Schematics of the accelerator system. Source: [33]……..…….. 33

3.3 The RF Ion source. Source: [36]……. 34

3.4 The high voltage power supply. Source: [33]……..... 35

3.5 (a) The steerer table and (b) the 90° Analyzing magnet on the analyzer table Source: [33]……. 37

3.6 Layout of the 45° beamline and the HRBS endstation……... 38

3.7 (a) Main chamber, goniometer and load lock (b) Load lock with a sample holder (inset picture) attached to the insertion rod and (c) View of sample holder on the goniometer attachment within the main chamber through the main viewport……... 40

3.8 Schematic of the vacuum pump and valve network……... 41

3.9 Schematic of the HRBS goniometer. Source: [37]……. 42

3.10 Front view of the control cabinet…… 43

3.11 (a) The actual and (b) schematic layout of the HRBS detection system. Ions backscattered from the target at a fixed scattering angle enters the spectrometer magnet. Ions with higher momentum will be bent with a larger radii (red) while lower momentum ions will have a smaller radii (green)…….. 44

3.12 Structure of the MCP. Ion incidence triggers an electron cascade down the channels. The channels of the two halves of the plate are oriented in different directions……... 45

3.13 Schematics of the HRBS electronics setup……. 47

4.1 Schematic of the HRBS spectrometer magnet…… 49

4.2 Overall layout of the HRBS detection system…… 50

4.3 Focal point calculations for magnet with (a) Flat exit edge (b) Circular exit edge. The scales of the axes are in metres……... 51

4.4 Schematic of the incident and backscattered beam profiles……... 54

4.5 Finite backscattered beam profile and point source approximation……... 54

4.6 Layout of the fringe field correction……... 56

4.7 Schematic of backscattered beam envelopes from point source……. 57

4.8 Schematic of translations of central trajectory due to slanted entrance edge…….. 58

4.9 Schematic of trajectory transformations due to beam divergence…….. 59

4.10 Layout of the Direct calculations in Mathematica…….. 61

4.11 Schematic of Matrix approach by Penner……... 62

4.12 Layout of the calculation for entrance parameter α……... 64

4.13 Schematic of the circular edge corrections to θ…….. 66

4.14 Schematic of exit beam calculations……... 67

4.15 Plot of the distance from the centre of the MCP vs epsilon, defined as the ratio of the ion energy E and the energy E_0 of the ion which hits the midpoint along the MCP…….. 68

4.16 3-dimensional isometric view of the workbench with a magnified view of the spectrometer magnet. One of the pole pieces was cut to show the ion trajectory between the pole pieces……. 70

4.17 Blown up view of the exit edge along the *x*-*y* plane. The black squares are electrode points, while the green circles are non-electrode points. The intersection of the dotted lines is the exit point for ions following the trajectory with radius equal to the magnet bending radius……... 70

4.18 Schematic of magnetic potential calculations for every point in workbench……... 73

4.19 The potential distribution plot along the *x*-*y* plane at a fixed value of *z*. The darkened flat top of the plot represents the region within the uniform magnetic field within between the pole pieces, while the smooth slopes at the sides represent the non-uniform fringe fields……... 73

4.20 Schematic of calculations of ***B*** field components……... 74

4.21 The overview of the workbench in the *x*-*y* plane looking down towards the negative *z*-direction……... 76

4.22 The variation of *B* along r-axis at the (a) exit and (b) entrance edge……. 77

4.23 The overlay of all spectra measured at various magnetic flux density during the calibration run. The horizontal axis is the position channels along MCP and channel 0 was set at the midpoint along the length of the MCP. Positive MCP channels correspond to the left of point *M* in both the analytical and numerical studies in the previous sections…….. 79

4.24 The plot of position of ion incidence vs ε. The experimental data was compared to the SIMION and the analytical calculations……... 81

5.1 (a) Plot of different sets of calibration data measured at approximately 4 months interval. (b) Plot of the residuals of data from all the sets relative to a single linear fit..……..... 83

5.2 (a) Plot of HRBS calibration data (surface edge position) along MCP vs ε with a smooth 6th order polynomial $C_f(\varepsilon)$ fit with the residuals plotted in (b). The normalized gradient $C'_f(\varepsilon)$ vs ε is plotted in (c)…... 84

5.3 Conversion of position to energy spectrum……... 86

5.4 Schematic of the process of combining several position windows into a single energy spectrum……... 87

5.5 Schematic of the position bounds and the corresponding epsilon bounds.. 89

5.6 Schematic of the Re-binning process…….. 91

5.7 CalibrateChB2 program user interface which consists of panels (a) – (d). The program allows for different calibration fit conditions and the graphical fit of the ε-x points is plotted out in (c) while the conditions are varied so as to allow for the identification of the best fit conditions…. 93

5.8 User interface of CompoundSP. The experimental and re-binning conditions are entered in the side panel (a), the position windows and their respective chosen regions are displayed in (b) – (c) and the final combined energy spectrum is displayed in (d)……... 94

5.9 Comparison between energy spectrum obtained using FORBIN and CompoundSP from regions in two separate position windows……... 95

5.10 Schematic of the epsilon bounds and the corresponding position bounds.. 98

5.11 Schematic of the REVBIN process……. 98

5.12 Schematic and layout of the installation of the electrostatic plates…… 100

5.13 Scaled diagram of the layout of the electrostatic plates relative to the MCP, as well as the calculated ion trajectories between the plates at different ion energies at a potential difference of 1 kV. Source : [45]…....101

5.14 The calibration data (also shown in Fig. 4.23) showing the variation in the height of the Ta peaks at different parts of the MCP……...102

5.15 Au / Ni position spectra taken at different spectrometer *B* with no applied field at the electrostatic plates and where there is an applied field of 200 kVm^{-1} between the plates. All spectra were taken to the same accumulated incident charge of 15 μC but the spectra taken with an applied field were shifted down vertically for easy comparison of the difference in the MCP response……...104

5.16 Position spectra of all 4 windows at different spectrometer field strengths B_i, $i = 1,2,3,4$ with energy at centre of each window $E_{0,i}$ …... 106

5.17 (a) Plot of raw and smoothed data with the reverse-binned ideal position spectrum (b) Plot of the correction factors as a function of MCP position.107

5.18 Forward-binned energy spectra of individual windows with and without applied correction with simulated ideal energy spectra for individual position windows…….108

5.19 The combined energy spectra from windows 2 - 4 with and without gain correction compared with the theoretical simulated spectrum……... 109

6.1 (a) HRBS non-aligned spectra of all samples and the schematic of the scattering geometry. (b) Expanded region at the Si surface edge. (c) Expanded region at Lu surface edge……... 112

6.2 The spectrum of the sample annealed at 400 ºC fitted with SIMNRA, with an inset showing the detailed fit of the Si surface edge……...113

6.3 Elemental depth profiles of (a) As-deposited sample, as well as samples annealed at (b) 400 ºC (c) 600 ºC and (d) 800 ºC…….. 114

6.4 Schematic of ion channeling. Source: [46]……..……...……... 115

6.5 (a) Schematic of the formation of the shadow cone at the surface and the trajectories of channeled particles. The horizontal scale on the right is compressed in relation to the vertical scale to show the trajectory oscillations. (b) The comparison between the channeled and the non-aligned RBS spectrum. The channeled spectrum shows a drastically reduced substrate signal. Source: [46]……...……. 116

6.6 (a) Schematic angular shift of the < 111 > channeling direction with decreasing depth in Si lattice under vertical compressive and tensile strain at the film-substrate interface as viewed in the < 110 > direction. Sample tilt is defined as the angle between the < 111 > direction and the sample normal, which is along < 001 >. (b) The stereographic projection of a cubic < 001 > Si lattice showing the angular displacement of < 111 > from < 001 > along (110) or equivalent planes (red)……. 117

6.7 Schematic of lattice strain calculations……... 118

6.8 (a) Layout of the scattering geometry during angular scans. Increasing sample tilts angles is in the direction of $+\theta$. (b) Spectra taken at different sample tilt for the 400 °C annealed sample along the (110) plane. The Si substrate signal decreases near the < 111 > direction (θ_{ch})……... 119

6.9 Angular scans for (a) As-deposited sample and samples annealed at (b) 400 °C, (c) 600 °C and (d) 800 °C. Each dip is fitted with a 2nd order polynomial function to determine its position……..120

6.10 Plot of estimated lattice strain (%) vs depth in Si beneath the film-substrate interface…….121

A.1 Schematic of binary scattering. Source: [22] …….. 131

A.2 Schematics of impulse approximation calculations……. 135

Chapter 1

Introduction

1.1 High-resolution Rutherford Backscattering Spectrometry

Conventional Rutherford Backscattering Spectrometry (RBS) provides a non-destructive means of obtaining quantitative elemental depth profiling of thin films. The solid-state Passivated Implanted Planar Silicon (PIPS) detector used to detect the energy of backscattered ions has a typical energy resolution of 10 ~ 15 keV, capable of providing a depth resolution of up to 5 nm at glancing geometries. However, the thicknesses of thin films in modern semiconductor research have been steadily reduced in recent years due to the rapid miniaturization of electronics, and have now reached regimes of the order of tens of angstroms. Conventional RBS is therefore unable to provide depth profiling for thin films of such thicknesses.

In 1994, Kimura *et al.* successfully demonstrated monolayer depth resolution in RBS by replacing the solid-state PIPS detector with a spectrometer–focal plane detector setup in a glancing angle geometry [1]. This is the High-Resolution RBS (HRBS), possessing an energy resolution of ~ 1 keV and sub-nanometer depth resolution.

HRBS is uniquely suitable for analysis of ultra-thin films, especially in gate dielectrics research. Apart from its capability of providing quantitative elemental depth profiling, it can also be used to measure the lattice strain of a crystalline substrate at the film-substrate interface by using the channeling technique. While spectroscopic methods like the time-of-flight Secondary Ion Mass Spectrometry (SIMS) does provide semi-quantitative ultra-shallow elemental depth profiling in certain situations, only HRBS allows for quantitative depth analysis of ultra-thin films in a non-destructive manner, providing accurate elemental and substrate lattice strain profiles with depth.

1.2 Spectrometer ion optics studies and MCP gain correction

The relatively complicated detection setup which provides HRBS with its superior energy resolution involves backscattered ion energy measurements over multiple stages with two different instruments: the spectrometer and the Microchannel Plate – Focal Plane Detector (MCP-FPD) assembly. The spectrometer spatially sorts the backscattered ions according to their momentum (energy) and the MCP-FPD subsequently detects the position of ion incidences along the focal plane of the spectrometer. This position information is then converted into energy information by the HRBS electronics.

Consequently, non-linearities and errors characteristic to the overall detection system are introduced by these instruments. The spectrometer energy-analyzing process is intrinsically a non-linear process governed by the bending properties of the magnet. Therefore, the magnet ion optics should be properly understood and compared to the

theoretical expectations so as to ensure that the momentum-sorting process of the backscattered ions is consistent with the design expectations of the detection system geometry (so that the energy assigned to it is accurate). The subsequent ion incidence position output of the MCP-FPD and its relevant electronics is also subject to modifications due to non-uniform MCP gain along its length, giving rise to MCP-characteristic variations in the position spectra and the resulting energy spectra. Such variations are artefacts of the detection system and may interfere with true stoichiometric variations in the final output spectra during RBS simulations. These MCP non-uniformities must be properly understood and corrected for. These concerns will be addressed in chapters 4 and 5 of this thesis.

1.3 Gate dielectrics research

Metal-Oxide Field Emission Transistors (MOSFETs) have been rapidly downscaled over the recent years in order to produce devices that are faster and have lower power consumption. This downsizing process has reached the point where the required thickness of the traditional SiO_2 gate dielectric of the MOSFET has reached sub-nanometer regime. At such a small thickness, the leakage current due to direct electron tunneling through the dielectric reaches unacceptable levels. Alternatives with a higher dielectric constant, or "high-k dielectrics", must therefore be used so that a thicker layer can be employed to reduce direct electron tunneling through the layer, and yet retain the same capacitative density as a layer of SiO_2 with a much smaller thickness.

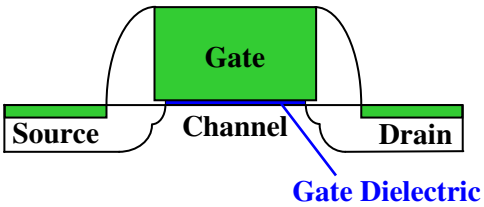

MOSFET Schematic
Fig. 1.1

Intense, ongoing research has yielded a host of possible high-k candidates [2 – 4], including dielectrics based on Si, Al, Hf, Zr, Ti, Y, Ta and Lanthanides. In fact, Intel has fabricated a functional CMOS gate stack with a SiO_xN_y gate dielectric as early as 2005 [5], and it recently announced Hf-based dielectrics of Equivalent Oxide Thickness (EOT) 1.0 nm are to be used in its upcoming 45 nm process technology [6]. However, for the downscaling process to continue in the future, dielectrics beyond SiO_xN_y and Hf-based films will have to be used. Lanthanide (Rare-Earth)-based films are one of the candidates for high-k replacements as they have large band gaps, high dielectric constants and low leakage currents [7]. In fact, quantum mechanical calculations of direct electron tunneling performed by Wu *et al.* [8] through several high-k candidates have shown that La_2O_3 has the smallest leakage current, and hence the lowest ultimate scaling limits among several dielectrics candidates, with an ultimate theoretical limit of EOT ≤ 5 Å as shown in Fig. 1.2.

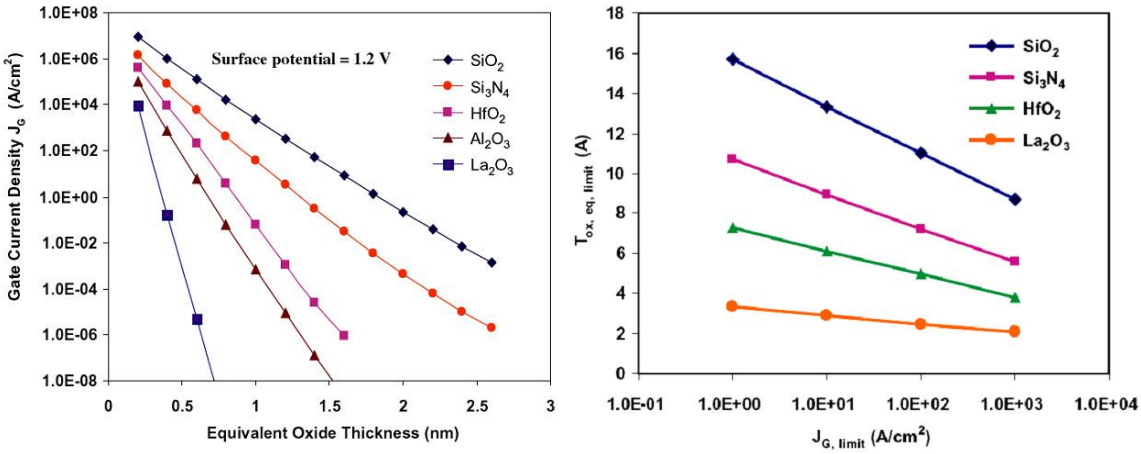

Fig 1.2 **(a)** Plot of direct tunneling current J_G through various high-k dielectrics vs EOT for a fixed applied gate voltage. **(b)** Plot of the scaling limit (EOT) of various dielectrics vs acceptable leakage current through the layer. Source: [7]

Within the Lanthanide series, Lutetium oxide (Lu_2O_3) has the highest lattice energy and band gap [9], it is therefore expected to be more insulating and thermally stable than other oxides of the series, as well as showing better hygroscopic immunity. The

suitability of Lu_2O_3 thin films were investigated by Darmawan *et al.* [10 – 12] and it was found to exhibit favourable electrical and morphological properties.

1.4 Analysis of Lu_2O_3 ultra-thin films with HRBS in CIBA

The superior depth resolution of HRBS, coupled with its non-destructive and quantitative spectrometric capability makes it highly suitable to probe the elemental profiles of ultra-thin films in high-k dielectric research. Of particular interest is the interface region between the film and the substrate, since the film-substrate interface quality will affect the performance of the gate stack. The strain imposed by the thin film on the Si lattice at the interface will also affect the charge mobility in the Si channel of the transistor.

Recently, HRBS has already been used to study ultra-thin films of SiO_2 [13], SiO_xN_y [14 – 15] and HfO_2 [16 – 18]. A review of a variety of HRBS analyses is also given by Kimura in [19]. The HRBS endstation in the Centre for Ion Beam Applications (CIBA) at the National University of Singapore (NUS) [20] was installed in 2004, receiving ion beams of high brightness and stability from a 3.5 MV Singletron Accelerator. Elemental depth profiles of ultra-thin Lu_2O_3/Si films, as well as the Si lattice strain distribution with depth at the interface were studied using HRBS in CIBA. The results from this study are presented in Chapter 6 of this thesis and they were published in [21].

1.5 Structure of this thesis

In chapter 2, the concepts and theoretical framework of RBS, as well as the method of simulation of RBS spectra are briefly described, while the Singletron accelerator and the physical experimental setup of the HRBS endstation in CIBA are described in detail in chapter 3. The spectrometer ion optics was simulated using numerical and analytical calculations and the results are compared to experimental data in chapter 4. The necessary spectrum processing during conversion of a position spectrum to an energy spectrum is explained in detail in chapter 5. Furthermore, the non-uniformities of the MCP-FPD were characterized, and a process to correct for them was developed. Finally, the results of HRBS depth profiling and interfacial Si lattice strain analysis of Lu_2O_3/Si ultra-thin films are presented in chapter 6.

Chapter 2

Physical Concepts

2.1 Introduction

The distinct advantage of Rutherford Backscattering Spectrometry (RBS) is its ability to provide quantitative and non-destructive depth profiling of the elements within the sample. In this chapter we present the basic physical concepts behind RBS, as well as an overview of the numerical simulation of RBS spectra using SIMNRA.

2.2 Overview of RBS physical concepts

There are four basic physical concepts in RBS, based on the following quantities:

i. Kinematic Factor K which is defined as the ratio of backscattered energy E_1 to incident energy E_0 for a backscattering event happening on the surface of the target at a certain scattering angle θ. This is determined by the dynamics of binary elastic collisions.

ii. Rutherford differential scattering cross section $\frac{d\sigma(\theta)}{d\Omega}$, which allows for quantitative determination of target composition.

iii. Ion stopping cross-section S which characterizes the ion stopping within the target. It depends on the form of the (screened) interatomic potential and leads to the capability of depth profiling of elements in the target.

iv. Energy straggling $\Omega_E^{\ 2}$, which arises from the statistical fluctuations of the energy transfer during the collision between the ion and the target atoms.

These quantities will first be separately presented and discussed. Subsequently, they will be put together to present the theory and concepts of RBS. The discussions in this chapter will be limited to concepts, quantities and corrections that are of direct relation to this project, and which are applied during RBS simulations to extract the results as presented in chapter 6.

2.2.1 Kinematic factor

In RBS, ions incident onto a target backscatter from target atoms which are effectively stationary. The mean free path between collisions is much greater than the atomic spacing, therefore the probability of correlated and simultaneous recoil of neighbouring atoms due to a single scattering event is very small, and we can assume all scattering events to be binary elastic collisions. The collision dynamics are expressed in the center-of-mass (CM) reference frame [22], in order to reduce the problem of the classical two-particle scattering in the laboratory (lab) reference frame into that of a single particle moving in a central force field potential centered at the origin of the CM frame. This will greatly simplify the derivation of the various quantities in the following sections.

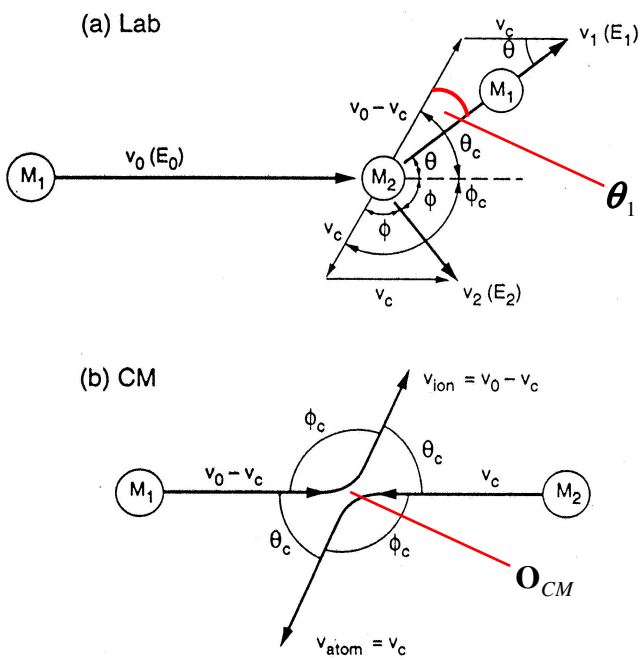

Fig. 2.1 Elastic collision diagrams as seen in the (a) lab reference frame (b) CM reference frame. Source: [22].

In the lab reference frame (Fig. 2.1 (a)), an ion of mass M_1, speed v_0 and energy E_0 scatters off a stationary target nucleus of mass M_2. After scattering, the ion moves off with speed v_1, energy E_1 and scattering angle of θ, while the target nucleus recoils with speed v_2, energy E_2 and angle ϕ. The equivalent situation in the CM reference frame moving with a constant speed v_c is shown in Fig. 2.1 (b). The ion and the target nucleus undergoes a symmetric scattering about the center of the CM frame ($\mathbf{O}_{CM}$), with the frame speed v_c chosen such that the total linear momentum *within* the frame is zero before and after the scattering event.

$$M_1\left(v_0 - v_c\right) = M_2\left(v_c\right) \qquad \Rightarrow \qquad v_c = \frac{\mu}{1+\mu} v_0$$

where $\mu = \dfrac{M_1}{M_2} < 1$ in RBS. The ion and target nucleus approach $\mathbf{O}_{CM}$ with speeds $\left(v_0 - v_c\right)$ and v_c respectively, and scatters off each other at the same CM scattering angle θ_c with their speeds unchanged. The CM velocity vectors before and after scattering are superimposed onto their counterparts in the lab reference frame in Fig. 2.1(a). From the geometry of the vector triangles,

$$\phi_c = \pi - \theta_c = 2\phi \qquad \Rightarrow \qquad \theta_c = \pi - 2\phi$$

$$\frac{v_c}{\sin\left(\theta_1\right)} = \frac{\left(v_0 - v_c\right)}{\sin\theta} \qquad \Rightarrow \qquad \theta_c = \theta + \theta_1 = \theta + \sin^{-1}\left(\mu \sin\theta\right)$$

The **Kinematic factor *K*** is defined as the ratio of the ion energy after backscattering to that before the scattering event in the lab reference frame, i.e. $K \equiv \dfrac{E_1}{E_0} = \dfrac{v_1^{\,2}}{v_0^{\,2}}$.

From Fig. 2.1(a),

$$v_1^{\,2} = v_c^{\,2} + (v_0 - v_c)^2 - 2v_c(v_0 - v_c)\cos(\pi - \theta - \theta_1)$$

$$= \left(\frac{\mu}{1+\mu}v_0\right)^2 + \left(\frac{1}{1+\mu}v_0\right)^2 - \frac{2\mu v_0^{\,2}}{(1+\mu)^2}\cos\left(\pi - \theta - \sin^{-1}(\mu\sin\theta)\right)$$

Let $\varphi = \sin^{-1}(\mu\sin\theta)$:

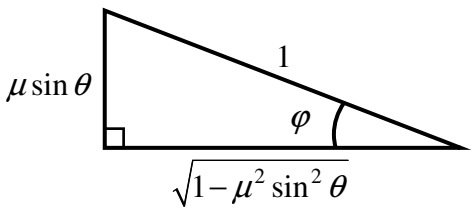

$$\therefore \quad \cos(\pi - \theta - \varphi) = \cos(\pi - \theta)\cos\varphi + \sin(\pi - \theta)\sin\varphi$$
$$= -\cos\theta\sqrt{1-\mu^2\sin^2\theta} + \mu\sin^2\theta$$

Hence we have:

$$v_1^{\,2} = \frac{v_0^{\,2}}{(1+\mu)^2}\left[1 + \mu^2 + 2\mu\cos\theta\sqrt{1-\mu^2\sin^2\theta} - 2\mu^2\sin^2\theta\right]$$
$$= \frac{v_0^{\,2}}{(1+\mu)^2}\left[(\mu\cos\theta)^2 + 2(\mu\cos\theta)\sqrt{1-\mu^2\sin^2\theta} + \left(1-\mu^2\sin^2\theta\right)\right]$$

So that finally,

$$K(\mu,\theta) = \frac{v_1^{\,2}}{v_0^{\,2}} = \frac{\left[\mu\cos\theta + \sqrt{1-\mu^2\sin^2\theta}\right]^2}{(1+\mu)^2} \quad , \quad \mu = \frac{M_1}{M_2} < 1$$

2.2.2 Rutherford scattering cross-section

Quantitative simulation of spectra in RBS requires the knowledge of the probability of backscattering a given ion into the detector at a given geometry. In the previous section, we reviewed the binary elastic collision in the CM reference frame using only the asymptotic values of momentum and energy far away from the collision site. However, developing the probability of backscattering at a given scattering angle would require a detailed description of the scattering trajectory near the scattering site, as the ion travels under the influence of a central (Coulomb) force in the CM reference frame.

The **Impact Parameter** b is defined as the perpendicular distance between the target atom and the straight ion trajectory in the hypothetical scenario where there is no (Coulomb) interaction between them (Fig. 2.2). During actual collisions, ions with impact parameter b will be deflected by an angle θ_c.

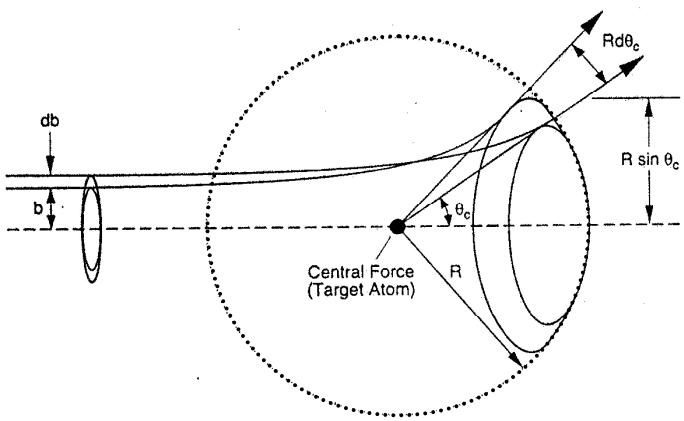

Fig. 2.2 Scattering of an incident ion with impact parameter between b and db into an angular region between θ_c and $\theta_c + d\theta_c$ in the CM reference frame. Source: [22].

The **Total cross-section** $\sigma(\theta_c)$ is the cross-sectional area πb^2 about the target nucleus, normal to the incident ion beam, within which ions will be deflected by

angles greater than θ_c. A more useful quantity is the **Angular Differential Cross-section** $\frac{d\sigma(\theta_c)}{d\Omega}$, which is defined as the probability of incident ions scattering into an angular region between θ_c and $\theta_c + d\theta_c$ per unit solid angle Ω of the detector, per areal density of target. Incident ions with impact parameters between *b* and *db* will be deflected through the annular area $2\pi(R\sin\theta_c)(Rd\theta_c)$ about the target, so that $d\Omega = 2\pi\sin\theta_c\, d\theta_c$. Therefore,

$$\frac{d\sigma(\theta_c)}{d\Omega} = \frac{2\pi b\, db}{2\pi\sin\theta_c\, d\theta_c} = \frac{b}{\sin\theta_c}\left|\frac{db}{d\theta_c}\right| \qquad \textbf{(1)}$$

Since θ_c increases as *b* decreases, and cross-section is positive by definition, we keep only the magnitude of $db/d\theta_c$.

To evaluate the expression for the angular differential cross-section, the relationship between *b* and θ_c is required. This is derived from the **Classical Scattering Integral** in the CM reference frame (Appendix A1):

$$\theta_c = \pi - 2b\int_{r_{\min}}^{\infty} \frac{dr}{r^2\sqrt{1-\frac{V(r)}{E_c}-\left(\frac{b}{r}\right)^2}}$$

where *r* is the distance of separation between the ion and target, $r_{\min}$ is the distance of closest approach, $V(r)$ is the interaction potential, and

$$E_c = \frac{1}{2}\left(\frac{M_1M_2}{M_1+M_2}\right)v_0^{\,2} = \frac{1}{1+\mu}E_0 .$$

is the CM energy.

We assume here that Coulomb repulsion is the only interaction between the ion and the target throughout the scattering process. The ion therefore moves within a conservative central force field with a potential $V(r) = Z_1 Z_2 e^2 / r$. We make the substitutions $u = \frac{1}{r}$ and $\alpha = Z_1 Z_2 e^2$, so that $V(r) = \alpha u$ and:

$$\theta_c = \pi - 2\int_0^{\frac{1}{r_{\min}}} \frac{du}{\sqrt{\left(\frac{1}{b}\right)^2 - \frac{\alpha u^2}{b^2 E_c} - u^2}} = \pi - 2\left[\sin^{-1}\left(\frac{-\left(bu + \frac{\alpha}{2bE_c}\right)}{\sqrt{1 + \frac{\alpha^2}{4b^2 E_c^{\,2}}}}\right)\right]_0^{\frac{1}{r_{\min}}} \qquad \textbf{(2)}$$

To evaluate $\frac{1}{r_{\min}}$, consider the CM energy at the point of closest approach:

$$E_c(r) = \frac{M_c}{2}\left[v_r^{\,2} + v_\theta^{\,2}\right] + V(r) = \frac{M_c}{2} v_r^{\,2} + \frac{l^2}{2M_c r^2} + V(r)$$

$$\Rightarrow \quad E_c(r_{\min}) = \frac{l^2}{2M_c r_{\min}^{\,2}} + V(r_{\min}) \qquad \text{since } v_r = 0 \text{ at } r = r_{\min}.$$

The angular momentum l has an asymptotic value of $M_c v_0 b$ at large r, and since both l and E_c are conserved throughout the motion, we have

$$E_c(r_{\min}) = E_c = V(r_{\min}) + \frac{(M_c v_0 b)^2}{2M_c r_{\min}^{\,2}} = \frac{\alpha}{r_{\min}} + \frac{E_c b^2}{r_{\min}^{\,2}}$$

$$\therefore \; b^2\left(\frac{1}{r_{\min}}\right)^2 + \frac{\alpha}{E_c}\left(\frac{1}{r_{\min}}\right) - 1 = 0$$

$$\Rightarrow \quad \frac{1}{r_{\min}} = \frac{1}{b}\left[-\left(\frac{\alpha}{2bE_c}\right) \pm \sqrt{\left(\frac{\alpha}{2bE_c}\right)^2 + 1}\right] \qquad \textbf{(3)}$$

Substituting **(3)** into **(2)**,

$$\theta_c = \pi - 2\left[\pm\frac{\pi}{2} - \sin^{-1}\left(\frac{-\left(\frac{\alpha}{2E_c b}\right)}{\sqrt{1+\left(\frac{\alpha}{2E_c b}\right)^2}}\right)\right] \quad \Rightarrow \quad \pm\sin\left(\frac{\theta_c}{2}\right) = \frac{-\left(\frac{\alpha}{2E_c b}\right)}{\sqrt{1+\left(\frac{\alpha}{2E_c b}\right)^2}}$$

We have, therefore,

$$\tan\left(\frac{\theta_c}{2}\right) = \frac{\alpha}{2E_c b} \quad \Rightarrow \quad b = \frac{\alpha}{2E_c}\cot\left(\frac{\theta_c}{2}\right) \qquad \textbf{(4)}$$

From **(4)** and **(1)**, we obtain the **Rutherford Scattering Cross-section** in CM frame:

$$\left.\frac{d\sigma(\theta_c)}{d\Omega}\right|_{\text{Rutherford, CM}} = \frac{\frac{\alpha}{2E_c}\cot\left(\frac{\theta_c}{2}\right)}{\sin\theta_c}\left[\frac{\alpha}{4E_c\sin^2\left(\frac{\theta_c}{2}\right)}\right] = \left(\frac{\alpha}{4E_c}\right)^2\frac{1}{\sin^4\left(\frac{\theta_c}{2}\right)}$$

Conversion to its Lab frame equivalent (Appendix A2) yields:

$$\left.\frac{d\sigma(\theta_c)}{d\Omega}\right|_{\text{Rutherford, Lab}} = \left(\frac{\alpha}{2E_0}\right)^2\frac{\left[\cos\theta + \sqrt{1-\mu^2\sin^2\theta}\right]^2}{\sin^4\theta\sqrt{1-\mu^2\sin^2\theta}}$$

Deviations from Rutherford cross-section

The Rutherford cross-section assumes that the incident ion experiences the unscreened Coulomb potential at all distances r from the target atom. However, the target nuclear charge is effectively screened out at large r due to the electron shells surrounding the target nucleus. For small E_0 where the point of closest approach is outside the bounds of the inner electron shells of the target atom, the target nuclear charge is partially screened during the whole process. At very large E_0 where the distance of closest approach is of the order of nuclear radius, nuclear reactions occur,

during which the Coulomb potential cease to apply. RBS measurements are usually conducted using E_0 values between these extreme cases, with the majority of the distances of closest approach being smaller than the *K*-shell radius of the target atom, but not to the extent where nuclear reactions occur.

Several authors have developed correction factors for the Rutherford cross-section [23 – 24]. The screening effect can be simulated by assuming that the approaching ion gains an additional kinetic energy due to the attraction between the ion nuclear charge and the electron shells of the target atom, during the time when the ion is still beyond the innermost shells. A widely used correction is by Andersen *et al.* [23] where he used a potential $V(r)$ that is corrected for the kinetic energy increase of approaching ion and with a cutoff at a suitably large value of *r*. He obtained a angular and energy dependent correction factor $F(\theta_c, E_c)$:

$$\frac{d\sigma}{d\Omega}_{\text{Andersen}} = F(\theta_c, E_c)\frac{d\sigma}{d\Omega}_{\text{Rutherford}} = \left[\frac{1+\dfrac{V_1}{2E_c}}{1+\dfrac{V_1}{E_c}+\left(\dfrac{V_1}{2E_c}\right)^2 \operatorname{cosec}^2\left(\dfrac{\theta_c}{2}\right)}\right]^2 \frac{d\sigma}{d\Omega}_{\text{Rutherford}}$$

$F(\theta_c, E_c)$ is plotted vs θ_c for various E_0 values in Fig. 2.3. The correction is insensitive to the scattering angle at large θ_c but drops off rapidly at small θ_c. For $\theta_c \geq 60^\circ$, $F(\theta_c, E_c)$ approaches unity as E_0 increases, with correction within ~ 7.5% for $E_0 = 500$ keV and ~ 2% at $E_0 = 2$ MeV.

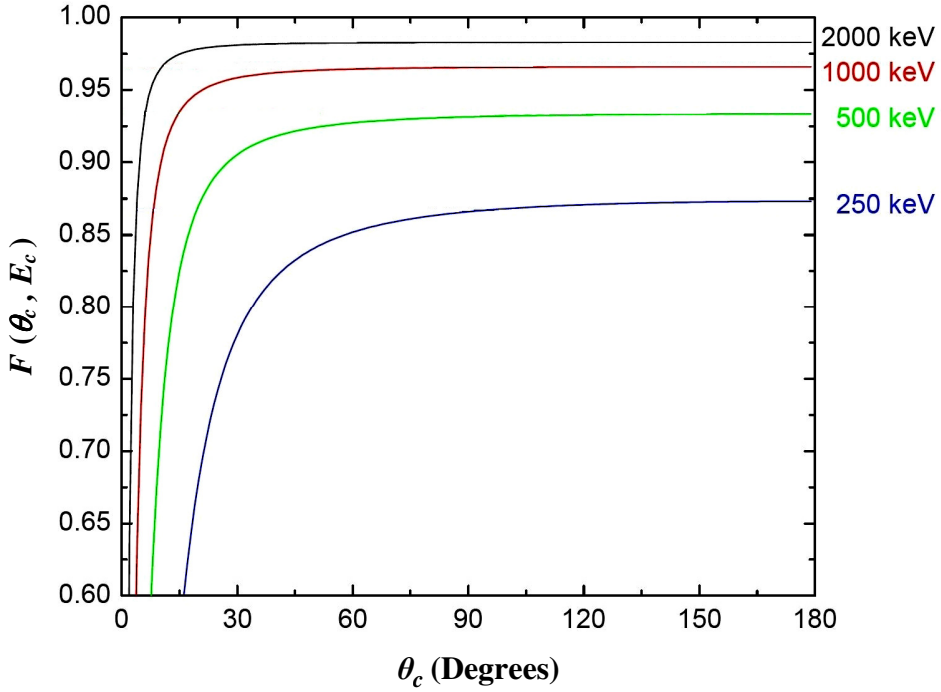

Fig. 2.3 Plot of $F\left(\theta_c, E_c\right)$ vs θ_c. Correction magnitude increases rapidly at small θ_c and decreases with increasing E_0 at large θ_c. Source: [25]

2.2.3 Stopping cross-section

Due to the relatively small probability of backscattering, the majority of ions incident onto the target will penetrate beneath its surface, either to be backscattered at a certain depth and travel back out of the target, or to be stopped at the eventual end of its trajectory within the target. As the ion moves within the target material, it will undergo collisions with the target nuclei and electrons, losing energy during the process. Ions backscattered from beneath the surface of the target will lose energy along the way in as well as along the way out of the target, before and after the backscattering event. Therefore the larger the energy loss of the backscattered ion, the greater is the depth of the backscattering event beneath the surface. This energy loss process provides for the depth scale capability of RBS.

The main quantity used during energy-loss discussions is the **Stopping cross-section**:

$$S \equiv \frac{1}{N}\frac{dE}{dx}$$

where N is the atomic density, and dE/dx (stopping power) is the energy loss per unit ion path length x within the target. The stopping cross-section can be split into two components $S = S_n + S_e$, where S_n and S_e are cross-sections due to collisions with the target nuclei and electrons respectively. Nuclear stopping are due to elastic collisions that can give rise to large scattering angles and discrete energy losses of the ion per collision event, while electronic stopping are mainly due to inelastic collisions involving much smaller energy losses per collision as well as negligible angular deflection of the ion trajectory. The relative importance of S_n and S_e depends on the ion energy E at each point of its trajectory, with S_n being significant only at low energies ($\leq 10\,\text{keV/amu}$). Since RBS (and HRBS) measurements are usually conducted with He^+ ions of $E_0 \geq 500\,\text{keV}$ and only backscattered ions with energies $E_1 \geq 250\,\text{keV}$ are measured, nuclear stopping is negligible ($S_N / S_e \sim 2\%$ in Si and $S_N / S_e \sim 0.4\%$ in Lu for 500 keV He ions) and will not be discussed here.

Theoretical frameworks exist for S_e at both high and low ion energies. For low energies ($E \leq 30\,\text{keV/amu}$), a well-known model is by Firsov (1959), where the duration of collision is assumed to be long enough to produce a quasi-molecule, during which work involved in the transfer and acceleration of electrons from target atom to ion contributes to the stopping process. The Firsov model, however, is limited to ion-target pairs with $Z_1 / Z_2 \leq 4$. Lindhard and Scharff (1963) used the Firsov

model, but with a different (screened) inter-atomic potential, so that the model extends to all arbitrary ion-target pairs. The low-energy Lindhard-Scharff electronic cross-section is given by:

$$S_{\text{Low}} = Z_1^{\frac{1}{6}}\left(8\pi e^2 a_0\right)\frac{Z_1 Z_2}{\left[Z_1^{\frac{2}{3}} + Z_2^{\frac{2}{3}}\right]^{\frac{3}{2}}}\left(\frac{v}{v_0}\right) \quad , \quad v < v_0 Z_1^{\frac{2}{3}}$$

where v is the ion speed, a_0 and v_0 are the Bohr radius and velocity respectively. At high ion energies ($E > 1\,\text{MeV}/\text{amu}$), the Bethe-Bloch model describes the energy loss process as that of a relativistic particle interacting with an isolated system (atom) of harmonic oscillators. The model yields the high energy stopping cross-section (Bethe-Bloch formula):

$$S_{\text{High}} = \frac{4\pi e^4 Z_1 Z_2}{m v^2}\left[\ln\left(\frac{2 m v^2}{I}\right) + \ln\left(\frac{1}{1-\beta^2}\right) - \beta^2 - \frac{C}{Z_2}\right] \quad , \quad v \geq v_0 Z_1^{\frac{2}{3}}$$

where m is the electron mass, $\beta = v/c$, with c being the speed of light, C/Z_2 is the shell corrections, and I is the mean excitation potential that involves all possible energy transitions and oscillator strengths for the target atom.

Most RBS measurements (as well as other ion beam analysis and material modification work) are performed within an intermediate energy region of $10\,\text{keV}/\text{amu} \leq E \leq 20\,\text{MeV}/\text{amu}$. Electronic stopping within this region $S_{\text{Intermediate}}$ is not well described by theory, and stopping cross-sections are obtained by interpolation between S_{High} and S_{Low}. The widely used interpolation function is:

$$\frac{1}{S_{\text{Intermediate}}} = \frac{1}{S_{\text{High}}} + \frac{1}{S_{\text{Low}}}$$

In practice, it is too inconvenient and complicated to calculate S_{High} and S_{Low} analytically for every different ion-projectile pairs and experimental conditions using the Lindhard-Scharff and Bethe-Bloch formulae. Parameterized functions were fitted over existing stopping data in both high and low energy regions for ease of extraction of cross-section values. Two commonly used fits of stopping data for He ions are the Andersen-Ziegler stopping data and the Ziegler-Biersack stopping data, where different fit function were used for S_{High} and S_{Low}. The **Andersen-Ziegler stopping** for He [26] uses:

$$S_{\text{Low}} = A_1 E^{A_2} \quad \text{and} \quad S_{\text{High}} = \frac{A_3}{E} \ln\left[1 + \frac{A_4}{E} + A_5 E\right]$$

where parameters $A_1 - A_5$ are given in tabulated form. The **Ziegler-Biersack stopping** for He uses the the Hydrogen stopping data fits by Ziegler, Biersack and Littmark [27] with parameters $C_1 - C_8$:

$$S_{\text{Low,H}} = C_1 E^{C_2} + C_3 E^{C_4} \quad \text{and} \quad S_{\text{High,H}} = \frac{C_5}{E^{C_6}} \ln\left(\frac{C_7}{E} + C_8 E\right)$$

These are then scaled [28] to obtain the He stopping data using the effective charge $\gamma_{\text{He}}{}^2$:

$$S_{\text{He}} = S_{\text{H}} \left(\gamma_{\text{He}} Z_{\text{He}}\right)^2 \quad \text{where} \quad \gamma_{\text{He}}{}^2 = 1 - e^{-\sum_{i=0}^{5} C_i E^i}$$

The accuracy of the sets of stopping data are typically ~ 5% with the difference between the two data sets being $< 5\%$.

2.2.4 Energy straggling

The energy loss processes of the ions within the target are statistical in nature. Mono-energetic ions incident onto the target surface therefore experience a spread in beam energy as they move within the target, due to the statistical fluctuations in the electronic and nuclear energy processes. This broadening of the ion energy distribution is known as energy straggling. As with the stopping cross-sections, the straggling due to nuclear energy loss is negligible. A simple model of electronic energy loss straggling is by Bohr (1915), where he made the following assumptions:

i. The velocity of the ion is much greater than that of the target electrons.

ii. The energy loss of the ion per collision event with a target electron is very small as compared to the total energy of the projectile.

iii. The target atoms and electrons are randomly distributed in the target.

iv. No channeling is involved in the travelling of ion within the target.

Assumptions (i) and (ii) allow for the Impulse approximation to be applied, where the energy transferred to an electron in a direction perpendicular to the incident ion trajectory is $E_{\perp} = \left(\frac{2}{m_e}\right)\left(\frac{Z_1 e^2}{b v_1}\right)^2$ (Appendix A3). From assumption (iii), the expected number of encounters with electrons for ions having impact parameters between b and db (Fig. 2.3) over a path length Δx is $NZ_2\,\Delta x \cdot 2\pi b\,db$, where N is the target atomic density. The actual number fluctuates statistically around this value. Assuming Poisson statistics, the standard deviation of the energy loss between b and db over Δx is $E_{\perp}\sqrt{NZ_2\,\Delta x \cdot 2\pi b\,db}$.

If the fluctuations are independent over different b, the total variance of the electronic energy is given by:

$$\Omega_{\mathrm{B}}{}^{2} = \int_{b_{\min}}^{b_{\max}} E_{\perp}{}^{2}\left(NZ_2\,\Delta x\,2\pi b\right)db = 2\pi NZ_2\,\Delta x\frac{\left(Z_1e^2\right)^2}{m_e v_1{}^2}\int_{b_{\max}}^{b_{\min}} E_{\perp}\left(-\frac{2}{b}\right)db$$

where $\Omega_{\mathrm{B}}{}^{2}$ is the customary notation for Bohr straggling. Since $dE_{\perp} = E_{\perp}\left(-2/b\right)db$,

$$\Omega_{\mathrm{B}}{}^{2} = 2\pi NZ_2\,\Delta x\frac{\left(Z_1e^2\right)^2}{m_e v_1{}^2}\left[E_{b_{\min}} - E_{b_{\max}}\right]$$

where $E_{b_{\min}}$ and $E_{b_{\max}}$ are the energy losses at $b_{\min}$ and $b_{\max}$ respectively. Since the largest energy transfer between ion of mass M_1 with speed v_1 and a stationary electron of $m_e \ll M_1$ is $2m_e v_1{}^2$, and that $E_{b_{\min}} \gg E_{b_{\max}}$, we have finally:

$$\Omega_{\mathrm{B}}{}^{2} = 4\pi\,NZ_2\left(Z_1e^2\right)^2\Delta x$$

Bohr's straggling theory is valid in the limit of high ion velocities, where the straggling value is almost independent of the ion energy. For lower ion energy E, Chu [29] developed a correction factor H to account for the electron binding in the target atoms, so that

$$\Omega_{\mathrm{Chu}}{}^{2} = H\left(\frac{E}{M_1}, Z_2\right)\Omega_{\mathrm{B}}{}^{2}$$

The Chu correction factors are tabulated for $100 \le E/M_1 \le 1000$ (keV/amu) by Szilágyi in [30] and are plotted for several values of E/M_1 as a function of Z_2 in Fig 2.4. For 500 keV He ions the deviation from Bohr straggling is typically 60% ~ 80%, with the largest deviation occurring for high Z_2 and low E. As energy increases, H approaches unity and becomes insensitive to both Z_2 and E.

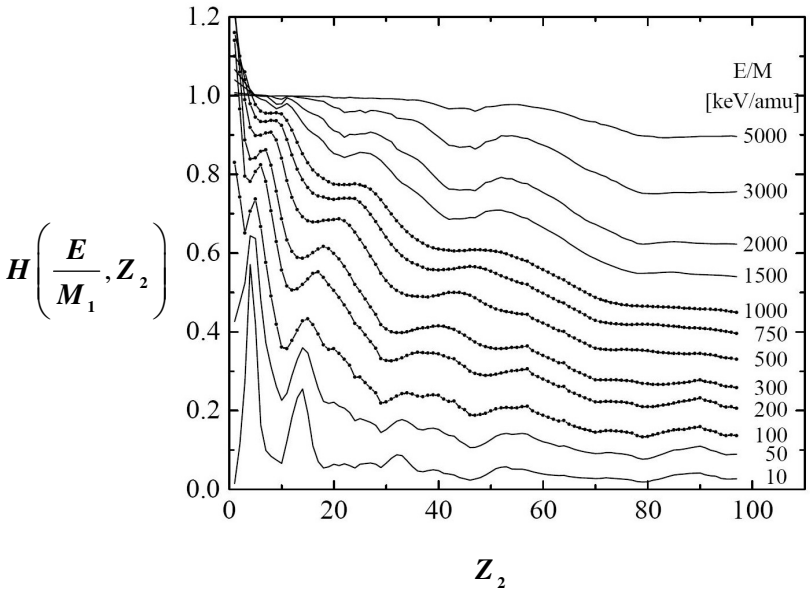

Fig 2.4 Plot of Chu correction factors H vs Z_2 for various E/M_1 values. Dots are original data from Chu, while lines are extrapolations by Szilágyi [30]. Source:[22]

Another source of energy straggling is from the fluctuation in the charge state of the ion, which was investigated by Yang *et al.* [31]. Ions with different charge states will transfer different amount of energy to the electron during each collision event. For He ions, their charge state as they travel through matter is constantly changing due to the excitation and capture processes of the electrons in the target along its trajectory. Such fluctuations in the charge state of the ion incur an additional energy straggling component given by the semi-empirical formula with fitted constants C_1 to C_4:

$$\frac{\Omega_{\text{Yang}}{}^2}{\Omega_{\text{B}}{}^2} = \frac{Z_1^{\frac{4}{3}}}{Z_2^{\frac{1}{3}}}\left[\frac{C_1\Gamma}{\left(\varepsilon - C_2\right)^2 + \Gamma^2}\right]$$

where

$$\Gamma = C_3\left[1 - e^{-C_4\varepsilon}\right] \qquad \text{and} \qquad \varepsilon = \frac{E}{\sqrt{Z_1^3 Z_2}}$$

For 500 keV Helium ions, the additional straggling component $\Omega_{\text{Yang}}{}^2 / \Omega_{\text{B}}{}^2$ is estimated to be ~ 0.25 in solid targets.

The total energy straggling Ω_E^2 is then the sum of the Chu and Yang straggling components:

$$\frac{\Omega_E^2}{\Omega_B^2} = \gamma_{He}^2 \frac{\Omega_{Chu}^2}{\Omega_B^2} + \frac{\Omega_{Yang}^2}{\Omega_B^2}$$

where γ_{He}^2 is the fitted effective charge factor used in the Ziegler-Biersack scaling of proton stopping cross-sections in the previous section.

2.3 Rutherford Backscattering Spectrometry

The quantities presented in the previous sections are now put together to form a basic theoretical framework of RBS. Our discussions here are limited to RBS analysis of thin films deposited on thick substrates, which is the focus of this thesis, the full description of the concepts of RBS can be found in [32]. We start with discussions of RBS measurements of thick elemental substrate samples, and then proceeding on to compound thin films on thick elemental substrates, and finally on to numerical simulation of RBS spectra.

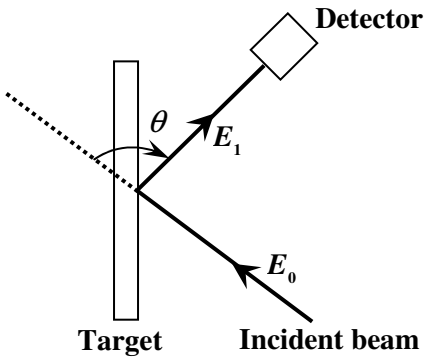

Fig 2.5 General layout of typical RBS measurement

During a typical RBS measurement (Fig. 2.5), incident ions of energy E_0 are backscattered into a detector placed at a certain scattering angle θ, which measures the backscattered ion energy E_1. The spectra obtained, after a series of electronic

signal processing, is a number distribution of backscattered ion energies E_1, which is then used to estimate the composition of the target, by numerical simulations of the energy spectra with the software package SIMNRA [25].

2.3.1 Thick elemental substrates

Fig. 2.6 shows the scattering geometry and spectrum of an RBS measurement of a thick, elemental target.

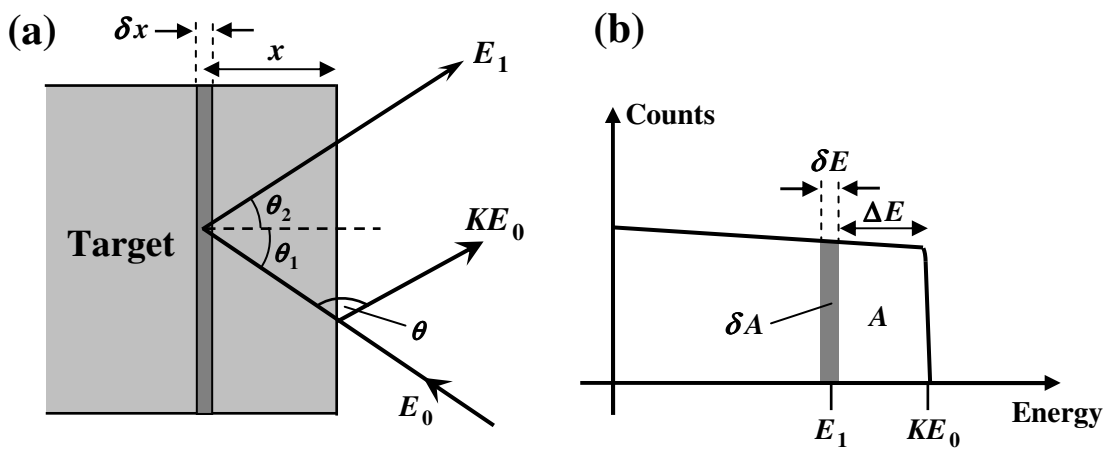

Fig. 2.6 **(a)** Scattering geometry and **(b)** spectrum of an RBS measurement of a thick, elemental sample

Incident ions that backscatter off the surface of the target will have energy KE_0, where $K = K(\mu, \theta)$ is the kinematic factor for this geometry, and E_0 is the incident ion energy. If the backscattering event happens beneath the surface, energy is lost as the ions move within the target before and after backscattering. Consider a thin region of thickness δx at a depth x beneath the surface. Ions backscattered within the region eventually emerge with a mean energy E_1 given by:

$$E_1 = K\left(E_0 - \frac{x}{\cos\theta_1}\frac{dE}{dx}\bigg|_{\mathrm{IN}}\right) - \frac{x}{\cos\theta_2}\frac{dE}{dx}\bigg|_{\mathrm{OUT}}$$

where the first term is the product of K and the energy of the ion just before the back-scattering event, and the second term is the energy loss of the beam along the way out. The energy difference between E_1 and KE_0 is

$$\Delta E \;=\; kE_0 - E_1 \;=\; \left[\frac{K}{\cos\theta_1} S_{\mathrm{IN}} + \frac{1}{\cos\theta_2} S_{\mathrm{OUT}}\right] Nx \;=\; [S]\, Nx$$

where $S = (1/N)(dE/dx)$ is the stopping cross-section, and $[S]$ is defined as the Stopping Cross-section Factor. ΔE is proportional to the areal density Nx of the target traversed by the beam before backscattering, and therefore provides a measure of backscattering depth beneath the surface.

The corresponding spectrum in Fig 2.6 (b) shows the RBS signal starting from energy KE_0 and extending towards lower energies. The spectrum height increases with decreasing energy and increasing backscattering depth, due to the E^{-2} dependence of the differential cross-section. The signal with an area (total number of counts) A within the energy width ΔE of the spectrum corresponds to backscattering events in the entire region within depth x of the target, while the signal of area δA and energy width δE in the shaded region of the spectrum at E_1 corresponds to backscattering events within the thin shaded region of thickness δx at depth x in the target. The number of backscattered particles δA and A are:

$$\delta A = \frac{\sigma(E(x))\Omega\, N\delta x}{\cos\theta_1} \quad \Rightarrow \quad A = \frac{N\Omega}{\cos\theta_1}\int_0^x \sigma(E(x))\,dx = \frac{\Omega}{\cos\theta_1}\int_{E_0}^{E_x} \frac{\sigma(E)}{S(E)}\,dE$$

where $\sigma(E(x))$ is the average differential cross-section at energy E and depth x, Ω is the solid angle of the detector, and N is the atomic density of the target. Evaluation of the integral on the right is not straightforward, since both scattering and stopping

cross-sections are functions of ion energy *E*. A brief overview of numerical evaluation during simulation of RBS spectra will be given in the last section.

2.3.2 Thin film systems

For thin films deposited on thick substrates, we are mainly interested in the stoichiometry and depth profile of heavy elements within the thin oxide films at the interface region with the substrate.

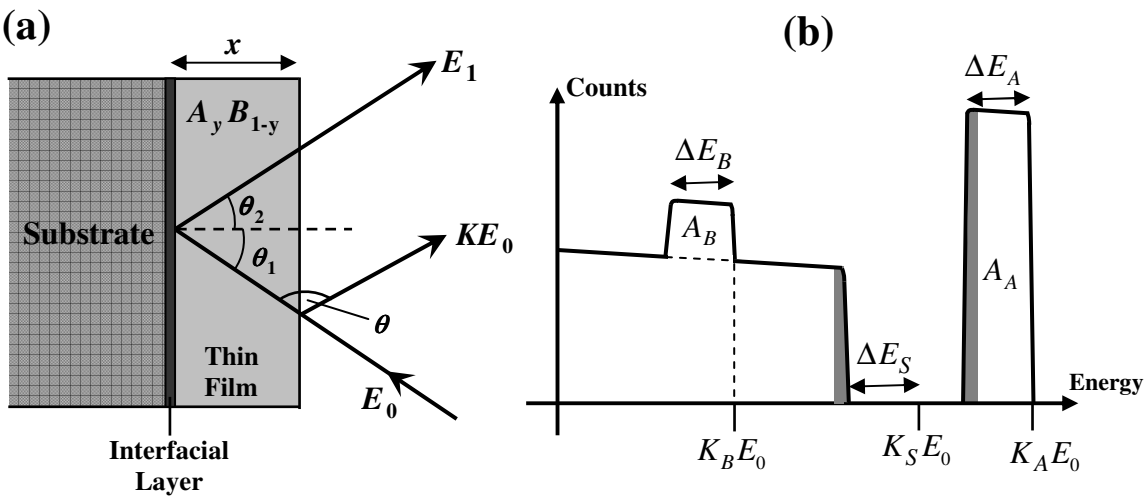

Fig. 2.7 **(a)** Scattering geometry and **(b)** spectrum of an RBS measurement of a thin compound target

Fig. 2.7 shows the scattering layout and the RBS spectrum of a thin compound film $A_y B_{1-y}$ on a thick substrate *S*, where in many cases during semiconductor research, *A* is usually a heavy element, *B* is either O or N, and *S* is usually Si. The signals from elements *A* and *B* in the spectrum have high energy edges at $K_A E_0$ and $K_B E_0$ respectively, with the substrate signal S pushed back to lower energy by ΔE_S, due to the ions losing energy within the thin film. The signal from *B* rests on top of the substrate signal *S*, due to $K_B E_0 < K_S E_0 - \Delta E_S$. Elemental depth profiling of the thin film is shown more clearly in the signal from *A*, which is isolated at higher energies.

Collisions with atoms of both A and B will now contribute to the energy loss process. Ions will lose the same amount of energy per unit length along the way in, but may lose a different amount along the way out depending on which atom they backscatter from, due to the difference in K values. The energy widths of the respective signals in the spectrum are:

$$\Delta E_A = [S]_A^{AB} N^{AB} x \qquad \text{and} \qquad \Delta E_B = [S]_B^{AB} N^{AB} x$$

with

$$[S]_A^{AB} = \frac{K_A}{\cos\theta_1} S_{\text{IN}}^{AB} + \frac{1}{\cos\theta_2} S_{\text{OUT},A}^{AB}$$

$$[S]_B^{AB} = \frac{K_B}{\cos\theta_1} S_{\text{IN}}^{AB} + \frac{1}{\cos\theta_2} S_{\text{OUT},B}^{AB}.$$

and where $N^{AB}x$ is the areal density of the thin film, S_{IN}^{AB} is the stopping cross-section of the ions along the way in, while $S_{\text{OUT},A}^{AB}$ and $S_{\text{OUT},B}^{AB}$ are the cross-sections along the way out after backscattering from atoms of A and B respectively. We assume that Bragg's rule of additivity applies to the stopping cross-sections for both inward (and outward paths at the same energy E, so that:

$$S^{AB}(E) = [y]S_A(E) + [1-y]S_B(E).$$

The area of the signals in the spectrum from elements A and B are:

$$A_A = \frac{\Omega}{\cos\theta_1}\int_{E_0}^{E_x} \frac{\sigma_A(E)}{S_A(E)}\, dE \qquad \text{and} \qquad A_B = \frac{\Omega}{\cos\theta_1}\int_{E_0}^{E_x} \frac{\sigma_B(E)}{S_B(E)}\, dE$$

These can then be used to determine the stoichiometric ratio between the elements in the film. Depth profiles of elements A and S at the interfacial layer are shown in shaded regions in the spectrum.

2.3.3 Effects of straggling in RBS spectra

The effects of straggling will degrade the attainable depth resolution at the interface, due to the broadening of energy distribution as the beam travels through the thin film.

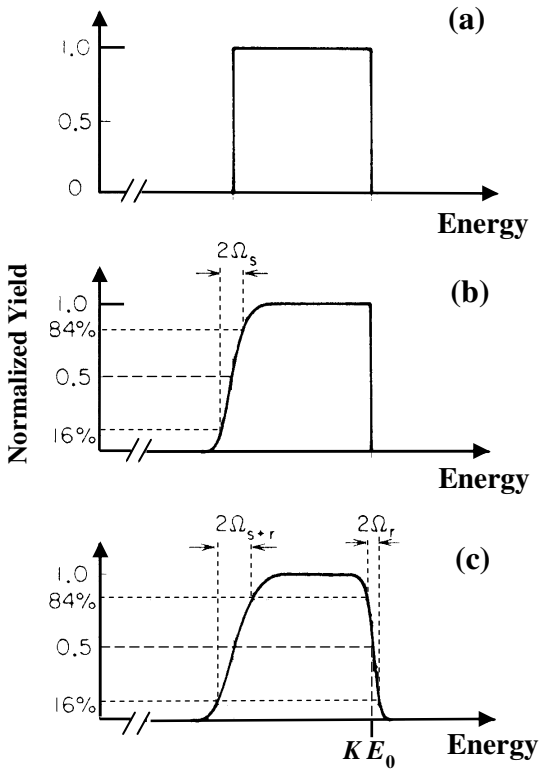

Fig. 2.8 Normalized elemental signal in a RBS spectrum where **(a)** the conditions are perfect, **(b)** there is influence from straggling only, and **(c)** there are influences from both system resolution and straggling. Source: [32]

Fig. 2.8 shows a normalized elemental signal in a RBS spectrum where

a) the condition are perfect,

b) there is only influence from beam straggling with standard deviation Ω_s,

c) there are influences from both system resolution Ω_r and beam straggling Ω_s.

Here the straggling is expressed as the standard deviation of the ion energy distribution. The distributions for both beam straggling and system resolution are assumed to be Gaussian.

2.3.4 Numerical simulation of RBS spectra using SIMNRA

During numerical simulations of RBS spectra by SIMNRA, the target is divided into many thin sub-layers, as shown in Fig. 2.9.

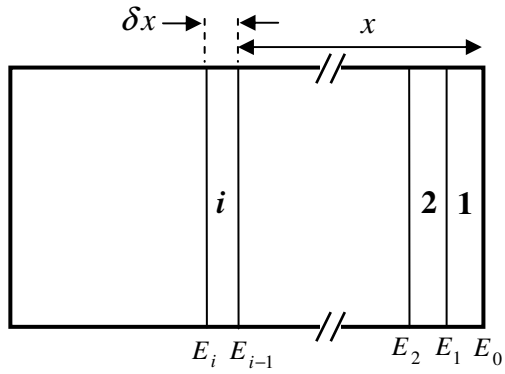

Fig. 2.9 Schematic of the target divided into thin sublayers.

Each sub-layer is assumed to be thin enough so that the variation of stopping power (cross-section) is negligible within the layer. For the ith sub-layer of thickness δx, the energy of the ions as they cross the front and back of the layer along the way in are E_{i-1} and E_i respectively, so that the energy loss within the layer ΔE_i and the energy of the beam $\bar{E}$ at the middle of each layer (mean energy) are given by

$$\Delta E_i = E_{i-1} - E_i = N\int_x^{x+\delta x} S\left(E(x)\right)\, dx \qquad \Rightarrow \qquad \bar{E}_i = E_0 - \sum_{j=1}^{i-1} \Delta E_j - \frac{\Delta E_i}{2}$$

where the integral in ΔE_i is numerically computed using the Runge-Kutta method. The ion energy along the outward path is computed similarly in reverse, starting with KE_i for backscattering at the back of sub-layer *i*, where *K* is the kinematic factor of the appropriate element. For compounds, the Bragg's rule of additivity is used to obtain $S(E)$ at each *E*.

Beam straggling σ_i within the (i^{th}) layer for the inward path is calculated by:

$$\sigma_{i,\text{IN}}{}^2 = \left(\frac{S\left(E_i\right)}{S\left(E_{i+1}\right)} \right)^2 \sigma_{i-1}{}^2 + \sigma_E{}^2 \quad \text{and} \quad \sigma_{i,\text{OUT}}{}^2 = K^2 \sigma_{i,\text{IN}}{}^2$$

where the first term of $\sigma_{i,\text{IN}}{}^2$ is the non-statistical beam straggling due to the varying stopping cross-sections, and $\sigma_E{}^2$ is the total (Chu and Yang) energy straggling within the layer with energy $\bar{E}_i$.

Scattering from within each sub-layer results in a corresponding signal component in the spectrum called a “brick”. Each brick has an area

$$dA = \frac{N\Omega}{\cos\theta_1} \frac{1}{S\left(\bar{E}\right)} \int_{E_i}^{E_{i-1}} \sigma\left(E\right) dE$$

where the stopping cross-section $S\left(\bar{E}\right)$ is assumed to be constant, and evaluated at the mean energy in the layer. The final spectrum is then formed by summing up all bricks from all depth and over all elements.

Chapter 3

Experimental Setup

3.1 CIBA Facilities

CIBA consists of two laboratories, each housing an accelerator. A single-ended 2.5 MV AN-2500 Van de Graaff accelerator from High Voltage Engineering (HVE) is housed in the auxiliary laboratory, providing ion beams to a single beamline leading to a NEC RC43 analytical endstation which allows for broad-beam conventional RBS and PIXE research. In the main laboratory (Fig. 3.1), three beamlines are attached to a single-ended 3.5 MV Singletron™ accelerator from High Voltage Engineering Europa (HVEE) [33] that provides ion beams which are brighter and more stable than those from the belt-driven Van De Graaff accelerators. At the 10° beamline, a state-of-the-art proton beam writer [34] is present, which allows for direct-write micro-machining while a nuclear microscope [35] is attached to the 30° beamline which is used for advanced materials analysis and elemental mapping of biological samples. The 45° beamline leads to the HRBS endstation, which is the focus of this thesis.

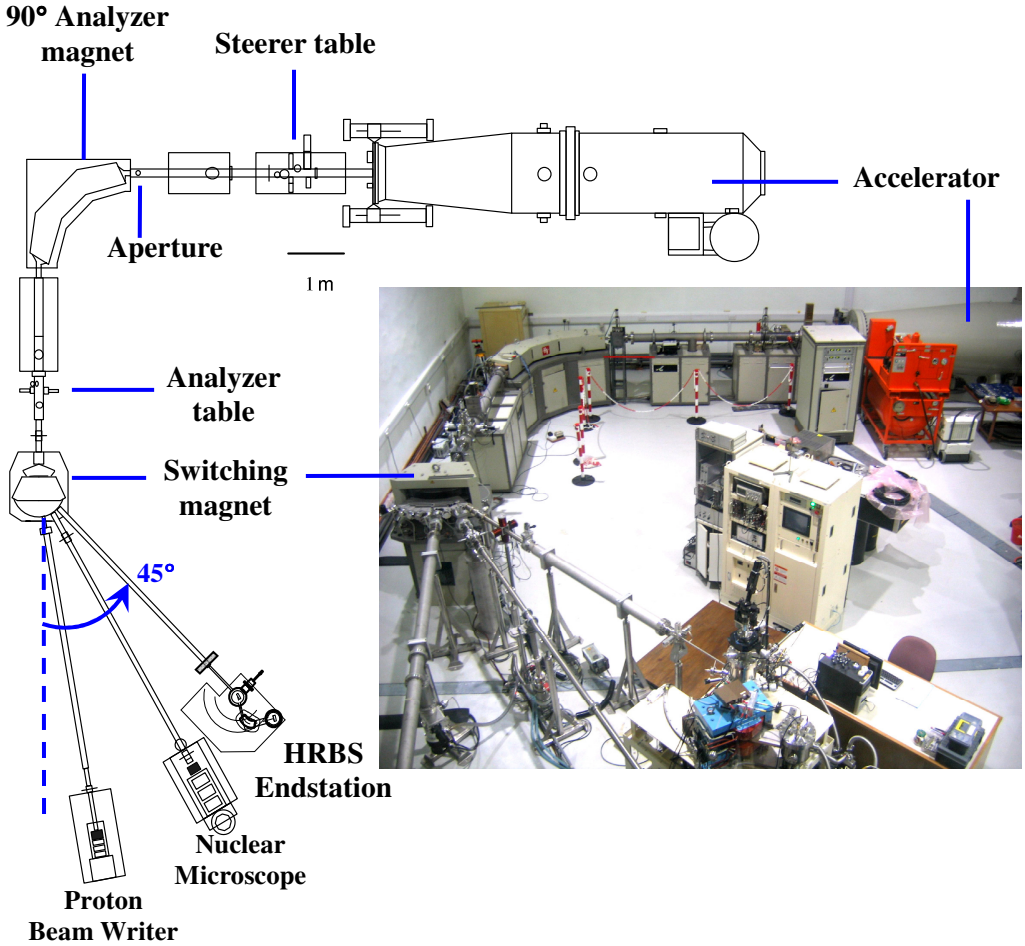

Fig. 3.1 Layout of the accelerator and beamlines

3.2 Singletron™ accelerator

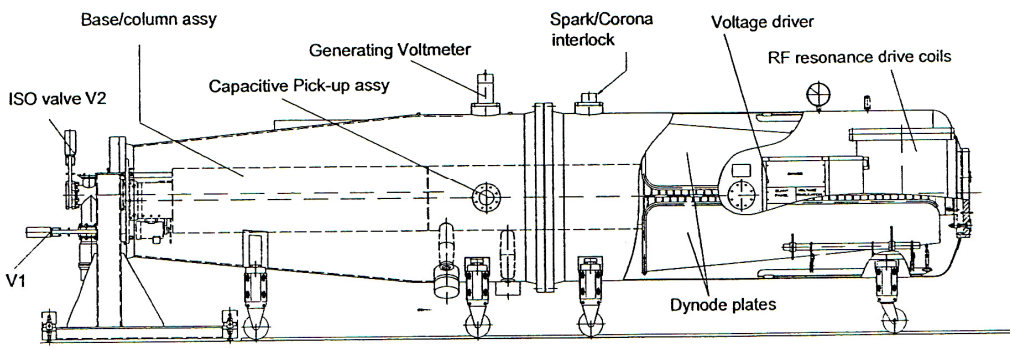

Fig. 3.2 Schematics of the accelerator system. Source: [33]

3.2.1 RF Ion source

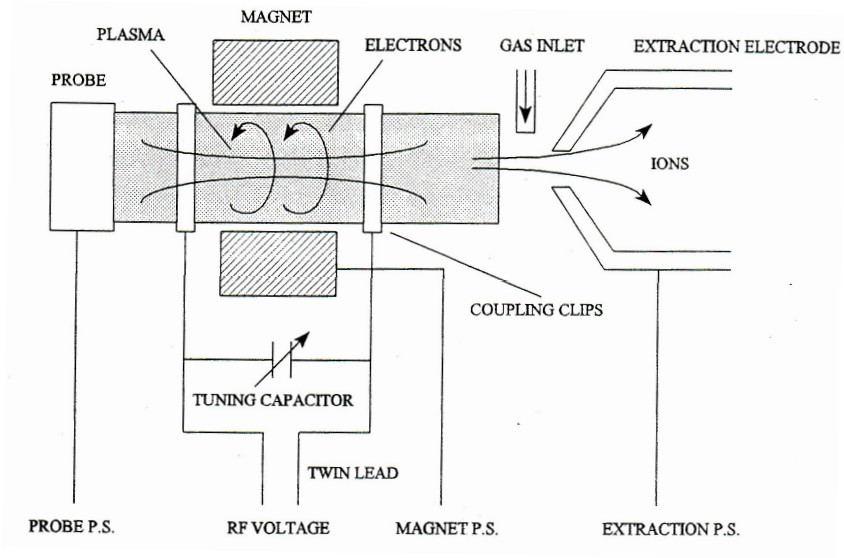

Fig. 3.3 The RF Ion source. Source: [36]

The RF ion source model 173 (Fig. 3.3) is used within the Singletron as a heavy duty profile source for proton, alpha and oxygen beams. The neutral gas is released into the ion source, where an RF voltage is applied. Electrons within the gas atoms are excited into oscillation by the RF field, quickly gaining enough kinetic energy to cause ionization and forming a plasma. Positive ions from the plasma are pushed out of the source by an applied electric field from the probe, and the resultant ion beam is focused by applied voltage at the extraction electrode. A set of permanent magnets apply an axial magnet field to create a toroidal motion of electrons that concentrates the plasma near the extraction electrode, increasing the ion beam current.

3.2.2 High voltage power supply

The high voltage power supply (Fig 3.4) provides the terminal voltage which accelerates the ions extracted from the ion source along the accelerator tube. The

driver electrodes are connected to RF oscillator coils which generate an AC voltage which is transferred to the rectifier stack by means of capacitative coupling.

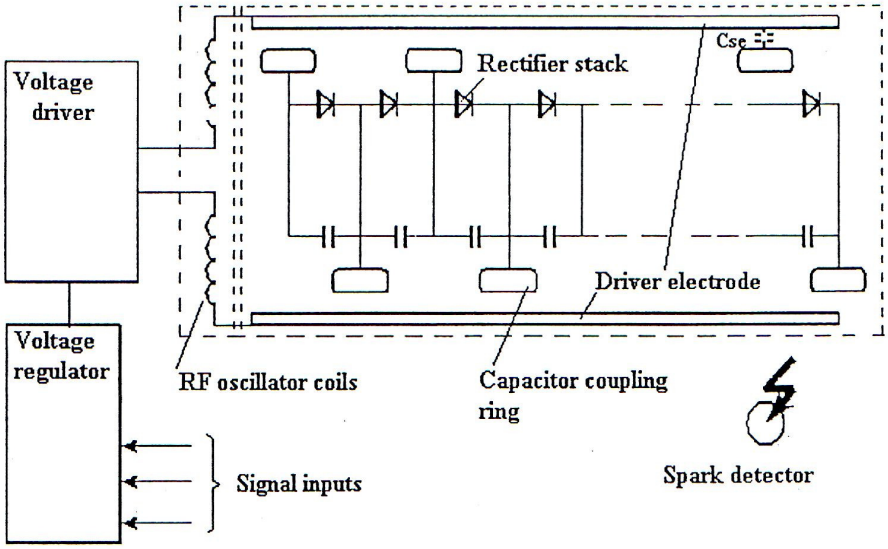

Fig. 3.4 The high voltage power supply. Source: [33]

The RC time constant of the stack is much larger than the period of the RF generated by the voltage driver, so that an equilibrium high positive voltage is generated at the top of the stack. Alternate capacitors along the stack are charged in the same electrical orientation during each half-cycle of the AC, with the rectifiers ensuring a net flow of current towards the positive accelerator terminal over the AC cycles. Potential differences across each charged capacitor along the stack eventually add up to the terminal voltage. A generating voltmeter (GVM) measures the potential of the terminal relative to the laboratory ground, while a capacitative pickup unit (CPU) measures the ripple of the terminal voltage and feeds the signal back to the voltage regulator controlling the voltage driver. The voltage driver then adjusts the terminal voltage accordingly to reduce the ripple, improving the energy stability of the beam. In the event of a tank spark, the corona/spark interlock will trigger a warning on the control computer and the voltage regulator will switch off the terminal voltage.

3.2.3 High voltage insulation and Electron suppression

The accelerator tank is filled with a heavy non-toxic insulating gas SF_6 at a pressure of 8 bar. SF_6 has a dielectric strength approximately 2.5 to 3 times that of air, and serves to prevent corona buildup and tank sparks. Other forms of electrical insulation are the vacuum and glass insulation within the accelerator tube, the plastic support members in the power supply and a variety of insulating cable covers. Also, electron suppression is employed via small permanent magnets within the accelerator to reduce the level of emitted radiation.

3.3 Beam steering and stablization

The beam output from the accelerator is adjusted at the steerer table (Fig. 3.5(a)) by electrostatic steerers along *x* and *y* axes along the *x*-*y* plane normal to the beam (*z*) direction and subsequently passes through a beam defining slit. A circular aperture checks the exact beam position and defines the maximum beam diameter just before the 90° analyzing magnet. The desired ion species is then selected by the magnet to pass into the stabilizer slit at the analyzer table (Fig. 3.5(b)). The currents created by the beam hitting on the left and the right of the stabilizer slit are monitored, and the slit assembly is connected via a feedback loop to the voltage regulator in the accelerator high voltage power supply. Any instability of the ion beam will cause changes in the slit currents, which in turn triggers a compensation response from the terminal voltage regulator in the accelerator, creating a stabilizing effect on the beam.

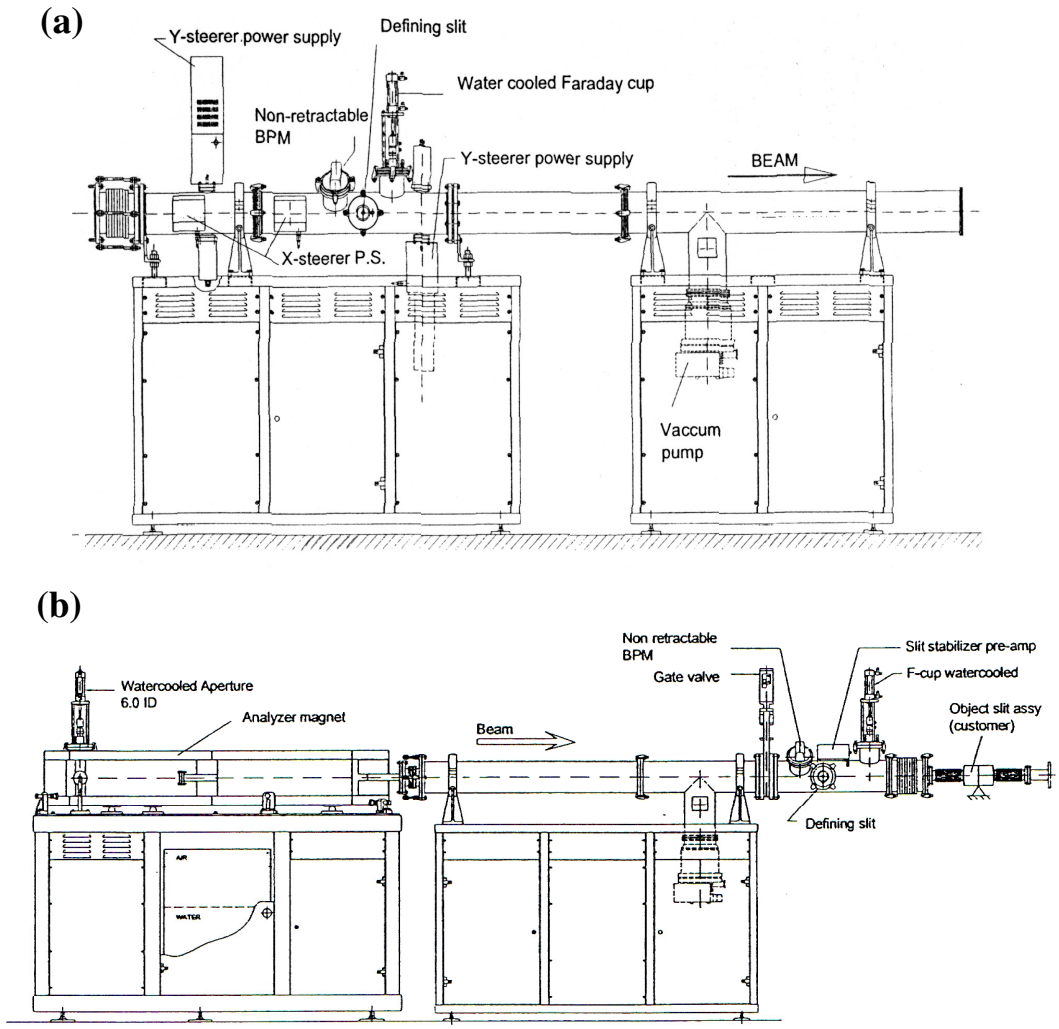

Fig. 3.5 **(a)** The steerer table and **(b)** the 90° analyzing magnet on the analyzer table. Source: [33]

On both steerer and analyzer tables, a beam profile monitor (BPM) and a faraday cup measure the beam profile along the *x*-*y* plane and the total beam current respectively. This facilitates the proper steering and focusing of the beam before it enters the switching magnet to be steered into one of the beamlines.

3.4 HRBS Endstation

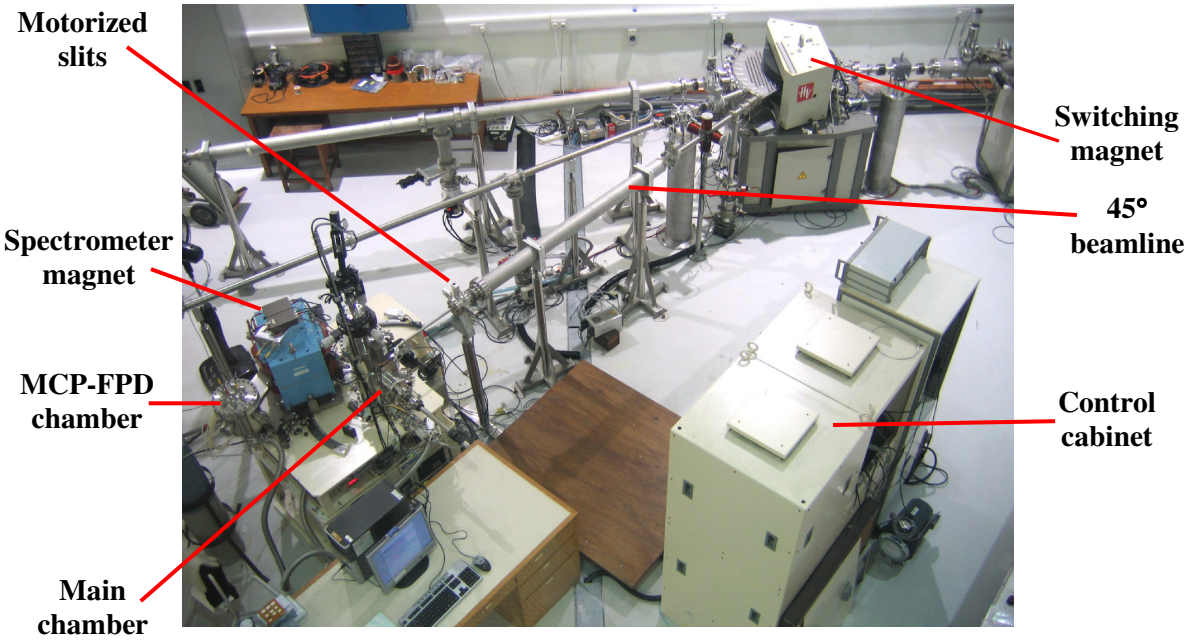

Fig. 3.6 Layout of the 45° beamline and the HRBS endstation.

Overview

The HRBS endstation was fabricated by the Machinery Company of Kobe Steel Ltd and installed at CIBA in 2003. The general setup (Fig 3.6) consists of:

i. Main chamber with a load lock chamber

ii. UHV Vacuum sytem (pumps, valves and interlocks)

iii. 5-axis goniometer

iv. Control cabinet

v. Spectrometer magnet and MCP-FPD chamber (HRBS detection system)

Both the main and the MCP-FPD chambers are constantly maintained under UHV with two turbo-molecular pumps, which are located beneath the main chamber and

the MCP-FPD chamber. Sample exchange is performed by a transfer rod which transfers a target holder onto the goniometer attachment in the main chamber from a load-lock chamber through a gate valve. A controller program at the control cabinet oversees the vacuum interlocks system and allows for programmed or manual control of all valves as well as the goniometer rotation axes.

During measurements, the divergence of the ion beam is defined using the motorized slits located ~ 1 m before the main chamber. The scattering target is suspended by a precision 5-axis goniometer and is applied with an electrical potential for secondary electron suppression. Backscattered ions subsequently enter the detection system, which consists of a 90° spectrometer magnet and a Micro-Channel Plate – Focal Plane Detector (MCP-FPD) stack. The system is mounted on a circular track which allows the scattering angle to be varied via 7 detection ports. The signal output from the FPD is processed by a network of electronics on the control cabinet to extract the position of incidence of the ion along its length. The spectrum is sorted by an MCA before being output by a software on a computer.

3.4.1 Main chamber, load lock and vacuum system

During RBS measurements, the sample is placed in a specially designed sample holder which is held on the goniometer attachment in the main chamber. Insertion and removal of the sample holder is done with a transfer rod normally contained within the load lock chamber.

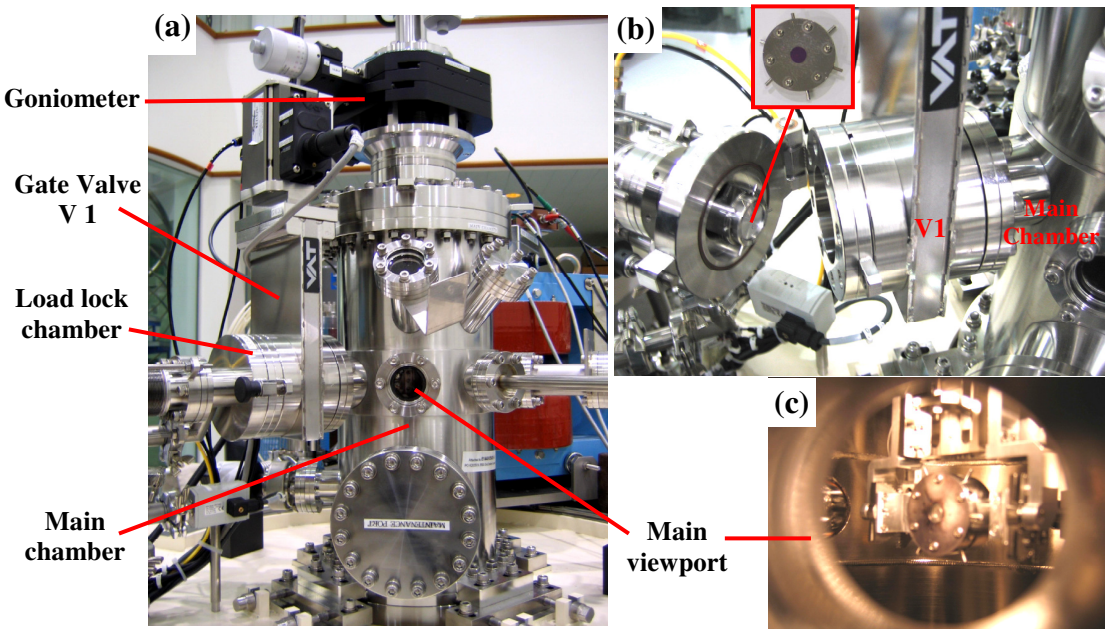

Fig. 3.7 **(a)** Main chamber, goniometer and load lock. **(b)** Load lock with a sample holder (inset picture) attached to the insertion rod **(c)** View of sample holder on the goniometer attachment within the main chamber through the main viewport.

A UHV vacuum of $< 5\times10^{-9}$ mbar is maintained by a Mitsubishi FT-800WH turbo-molecular pump (TMP) in main chamber (TMP 1) and a Mitsubishi PT-50 TMP in the MCP-FPD chamber (TMP 2), as shown in Fig. 3.8. Both TMPs are being backed by a Mitsubishi DS-251L scroll pump with valve V2 perpetually open. Valve V3 allows the load-lock to be pumped (also by the scroll pump), V4 controls the venting with N_2 during sample change and V1 isolates the load lock from the main chamber. The network is regulated by an interlocks system at the control cabinet, preventing

any sudden change in vacuum pressure by accidental activation of inappropriate valves.

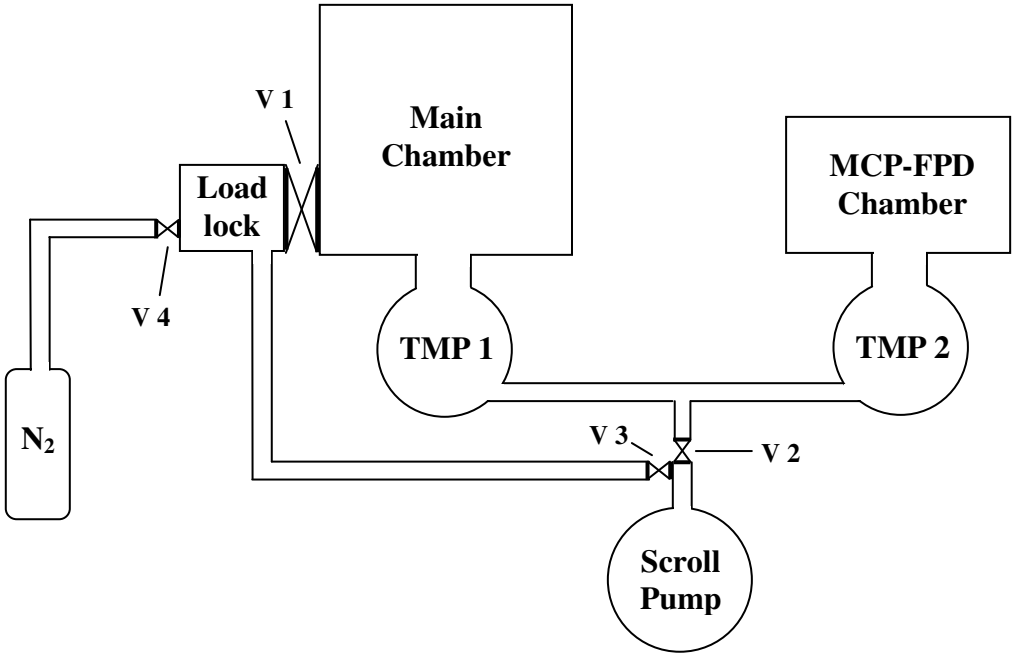

Fig 3.8 Schematic of the vacuum pump and valve network.

During sample change, programmed sequences can be initiated from the graphical user interface on the control cabinet which automatically activates the appropriate valves in the correct sequence. During the insertion of the sample into the main chamber, the sample holder containing the target is placed onto the transfer rod within the load lock with all valves except V2 closed. The insertion sequence is activated, where V3 is first opened to allow the load lock to be pumped to a pressure of ~10^{-2} mbar before opening V1 to allow the user to transfer the sample into the main chamber. Once that is done and the inserting rod is retracted back into the load lock, both V1 and V3 are closed, ending the sequence. The sample removal sequence is slightly different: again V3 is first opened to pump down the load lock before opening V1. Once the user removed the sample and the transfer rod is retracted into the load

lock, both V1 and V3 are closed. V4 is then opened to allow N_2 to flood the load lock back to atmospheric pressure, after which the load lock chamber can be opened to remove the sample.

3.4.2 Goniometer

A Kitano Seiki 5-axis goniometer controls the sample orientation within the main chamber. It allows for translation in the *x*, *y* and *z* axes, as well as rotation about the θ and ϕ axes (Fig. 3.9). The translation resolution is 0.01 mm with a repeatability of $\leq$0.05 mm along all directions, while rotations have resolution of 0.05° and are repeatable to within ± 0.05°. An electric potential of ~ +480 V is applied to the attachment which holds the sample holder during measurements, suppressing secondary electron emissions to allow for accurate beam current readings.

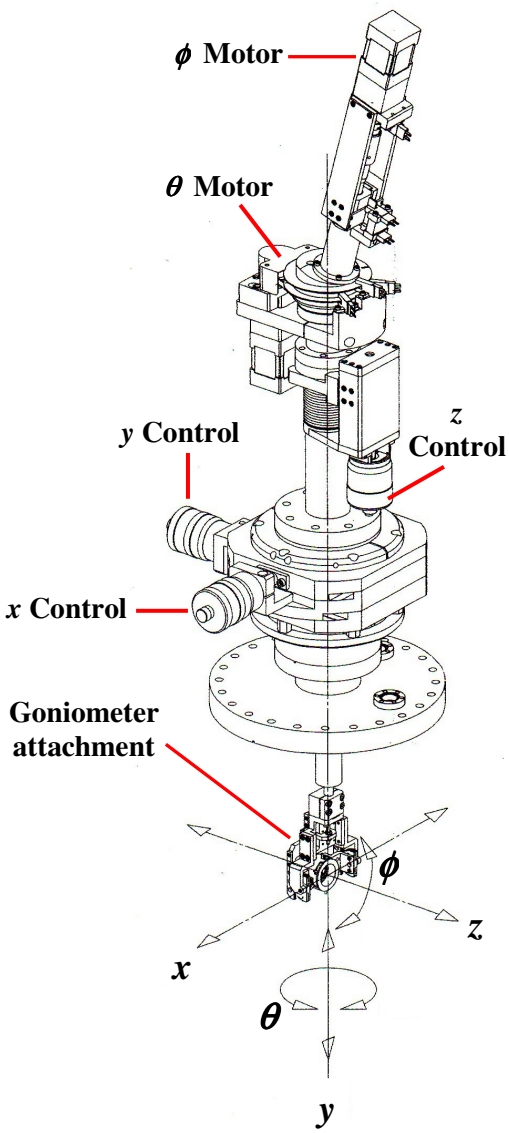

Fig. 3.9 (Right) Schematic of the HRBS goniometer. Source: [37]

3.4.3 Control cabinet

The goniometer and vacuum system controls are accessed from a touch-screen control panel that is found on the control cabinet, which also houses the vacuum gauge readouts, MCP electronics, as well as the MCA.

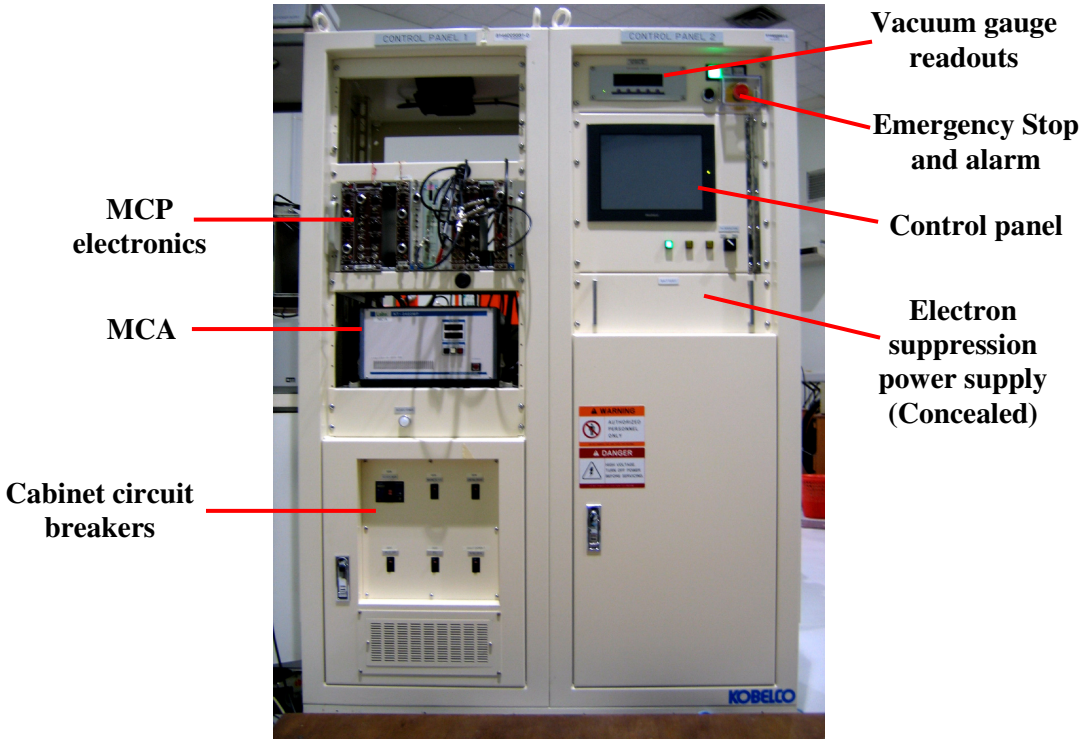

Fig. 3.10 Front view of the control cabinet.

The power supply for the electron suppression voltage applied on the sample is also installed within the cabinet, comprising two 240V dry cells in series. The cabinet circuitry is electrically protected by a network of circuit breakers, while the vacuum and the spectrometer magnet cooling systems are monitored by an interlocks program, which is accessible from the control panel. An alarm will sound whenever the interlocks is triggered, and an emergency stop button allows for automatic emergency shutdown of the HRBS endstation.

3.5 HRBS Detection system

Superior energy resolution of HRBS is achieved by replacing the solid-state PIPs detector in normal RBS with a detection system that consists of a spectrometer magnet and a 100 mm long by 15 mm width Micro-Channel Plate (MCP) – Focal Plane Detector (FPD) stack. Backscattered ions of energy E enter the spectrometer magnet at a specific scattering angle where they follow circular trajectories with radii r that are proportional to $E^{0.5}$ (Fig 3.11). These ions then incident onto the MCP-FPD stack at the focal plane of the spectrometer.

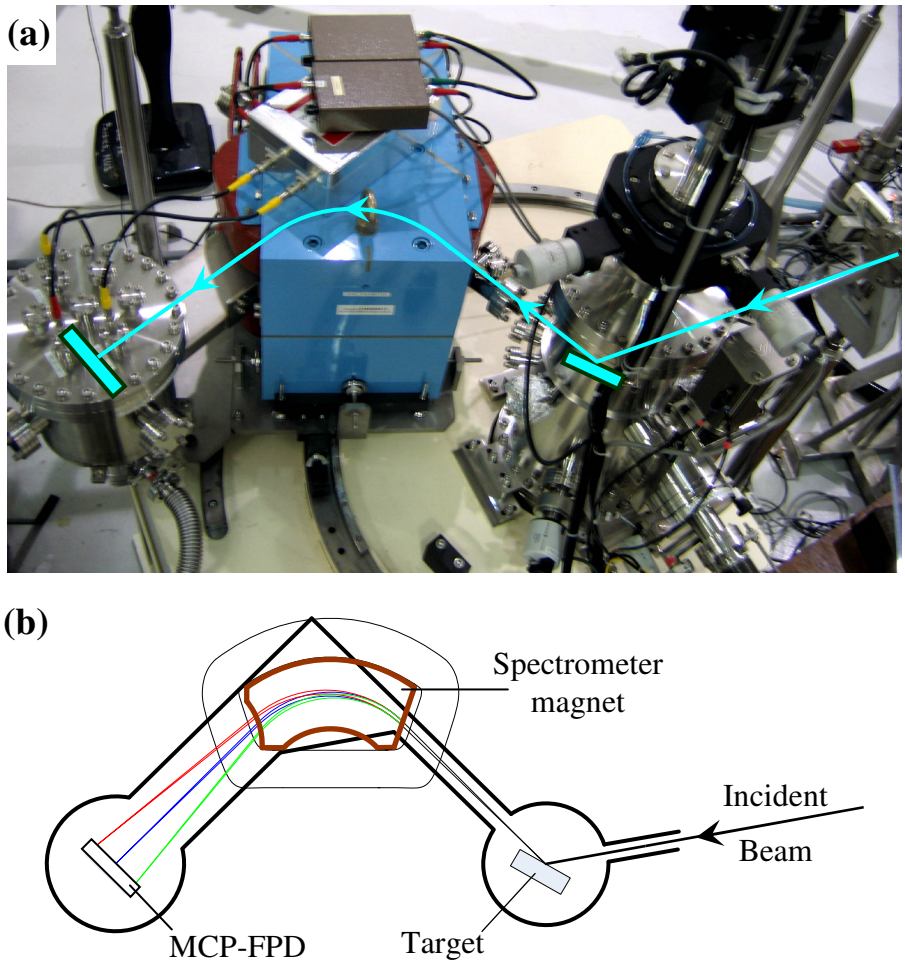

Fig. 3.11 **(a)** The actual and **(b)** schematic layout of the HRBS detection system. Ions backscattered from the target at a fixed scattering angle enters the spectrometer magnet. Ions with higher momentum will be bent with a larger radii (red) while lower momentum ions will have a smaller radii (green).

The incidence of a backscattered ion onto the MCP triggers an electron cascade, which deposits a charge/voltage pulse onto the FPD. The FPD, being of a resistive strip type, determines the position of the pulse and hence the ion incidence along its length using a simple charge division method. The spectrum obtained directly from the system is therefore a "position spectrum", which is a position distribution of backscattered ions at fixed intervals of length along the MCP-FPD. The energy spectrum is subsequently obtained by processing the position spectrum, using a forward-binning process, which will be described in Chapter 4.

3.5.1 Micro-Channel Plate

The MCP consists of a stack of 2 channel plates with rows of micro-channels as shown in Fig. 3.12.

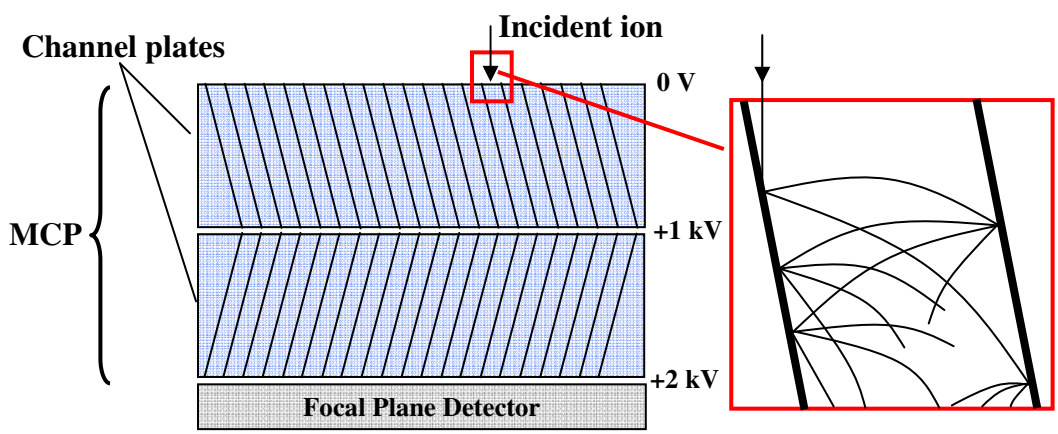

Fig. 3.12 Structure of the MCP. Ion incidence triggers an electron cascade down the channels. The channels of the two halves of the plate are oriented in different directions.

The function of the 1-dimensional FPD is to detect the position of incidence of energy-analyzed backscattered ions along its length. However, the charge carried by each ion is insufficient to generate an electrical signal large enough for the subsequent electronic equipment to pick up. Therefore, an MCP acts as an amplifier of the

electrical signal using an electron multiplication process initiated by the incidence of a single back-scattered ion. The walls of the micro-channels have low electron-emission work function, and a bias of about 1 kV is applied across each channel plate using an ORTEC 660 High Voltage Bias so that an incident backscattered ion will initiate an electron cascade down the channel. The electron multiplication process will saturate, depositing a charge pulse onto the FPD.

Residual gas molecules within the channels may be ionized during the cascade process, which will accelerate back up the channels. To prevent such gas ions from gaining enough kinetic energy to initiate another cascade, the orientation of the channels within each plate stack are angled relative to each other. This is to ensure that the acceleration of gas ions produced within the bottom plate will be either stopped or interrupted at the angled junction between two plates, preventing them from gaining kinetic energy continuously through the entire 2 kV bias.

3.5.2 Focal Plane Detector and HRBS electronics

The FPD is a 100 mm long resistive strip of uniform resistance per unit length. Once the electron cascade deposits a charge pulse onto the FPD, the system performs a simple charge division calculation electronically to determine the position of the pulse, and hence the ion incidence, along the MCP-FPD stack as shown in Fig. 3.13. A voltage pulse V_0 is deposited on the FPD at point X, which in turn causes currents I_L and I_R to flow towards the left and right ends of the FPD respectively. The charges collected Q_L and Q_R are measured at the left and right ends of the FPD respectively over the same time interval Δt and are compared to the total charge collected to calculate the distance of X from the ends of the FPD.

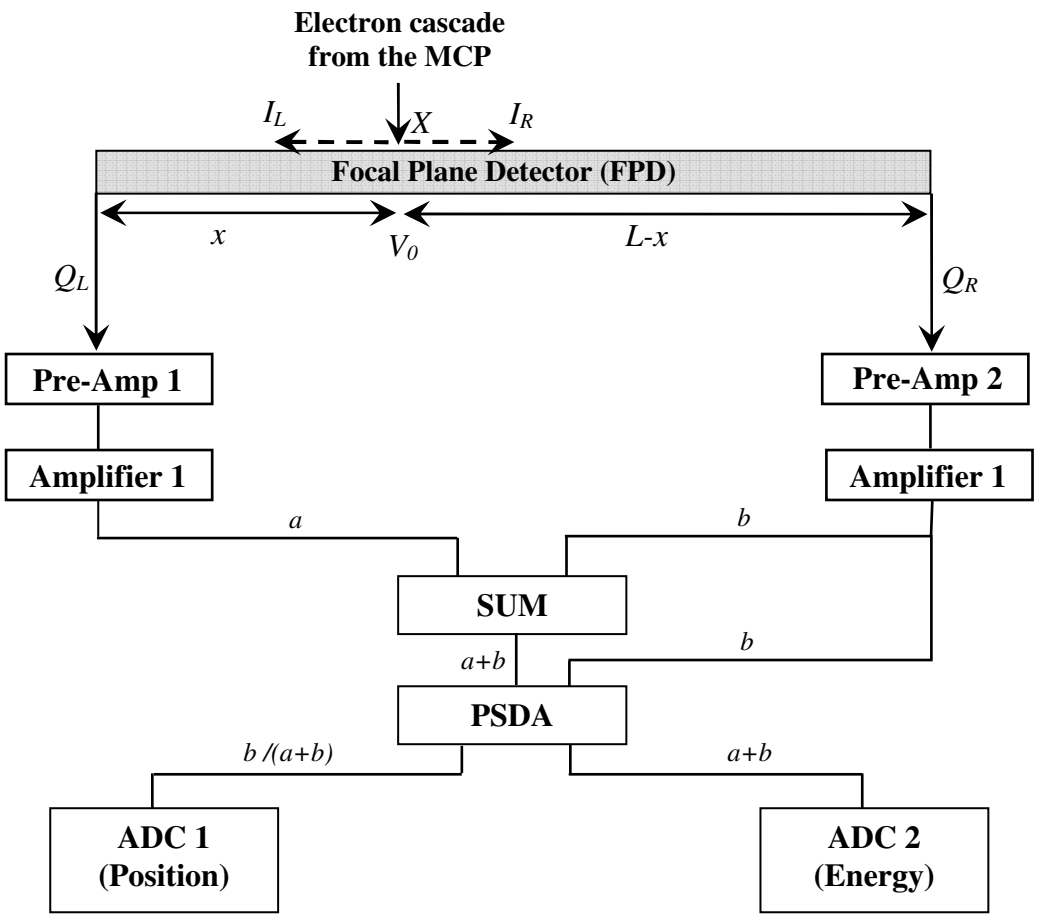

Fig. 3.13 Schematic of the HRBS electronics setup

Let the length of the FPD be L. Since it has uniform resistance per unit length,

$$\frac{I_L}{I_R} = \frac{L-x}{x} = \frac{Q_L\,\Delta t}{Q_R\,\Delta t} \quad \Rightarrow \quad x = \frac{Q_R}{Q_L+Q_R}L$$

The charge division is performed electronically by a network of analog processors. The charge pulses Q_L and Q_R are each processed first by ORTEC 113 Pre-amplifier and then by ORTEC 571 Amplifier. The resultant pulses were then added using ORTEC 533 Dual Sum and Invert card. A Seiko EG&G PSDA card is used to divide an amplified signal with the summed signal to obtain the position output, while a summed signal output (Energy) is also available. Thereafter, the output is fed into a Canberra 8706 ADC and subsequently sorted using a Labo NT2400 Multichannel Analyzer, before the spectrum is obtained, on the PC.

Chapter 4

Analytical and Numerical studies of Spectrometer Ion Optics

4.1 Introduction

In this chapter, the bending property of the spectrometer magnet is modeled with:

i. Simple analytical calculations developed using the Mathematica scientific programming software [38] with ion trajectories within the magnet determined using:

   a. Direct construction of circular trajectories

   b. Matrix-transport approach by Penner [39].

ii. Full numerical calculation of the magnetic field using SIMION software [40].

The above models adopted the actual HRBS scattering geometry and shapes of the entrance and exit edges of the spectrometer in CIBA. The results from these models are compared to the actual experimental data so as to ensure that the spectrometer works as designed. All dimensions and distances in this chapter are measured in metres.

4.2 HRBS Spectrometer magnet

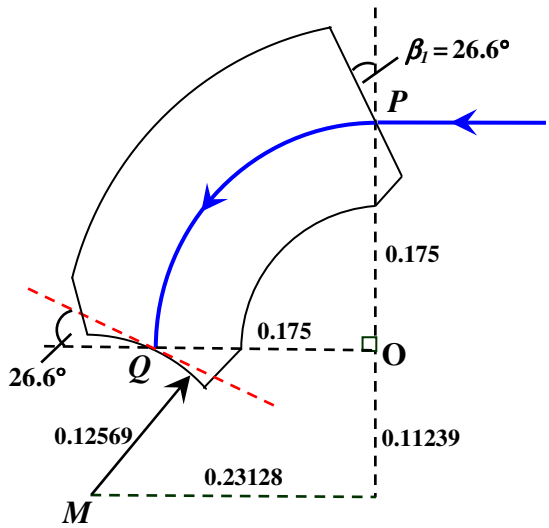

Fig. 4.1 Schematic of the HRBS spectrometer magnet.

The HRBS spectrometer magnet in CIBA is a 0.175 m double-focusing 90° sector magnet with a straight entrance edge rotated by 26.6° and a circular exit edge of radius 0.12569 m. The schematic is shown in Fig. 4.1. Let the origin O be the centre of the trajectory with radius ρ_0 = OP = OQ = 0.175 m (blue). The circular exit edge has centre at point M with coordinates (–0.23128, –0.11239) relative to the origin. The trajectory cuts the exit edge at Q where its tangent (dotted red) meets horizontal OQ at an angle of 26.6º. Assuming a static magnetic field, every ion energy E has a unique "central trajectory" with radius ρ given by:

$$\rho = \frac{\sqrt{2mE}}{Bq}$$

where m = Mass of the ion, B = Magnetic flux density and q = Ion charge. The central trajectory will be used to determine the exit point Q in the analytical calculations in the later sections in this chapter.

4.3 Overall layout of the HRBS detection system

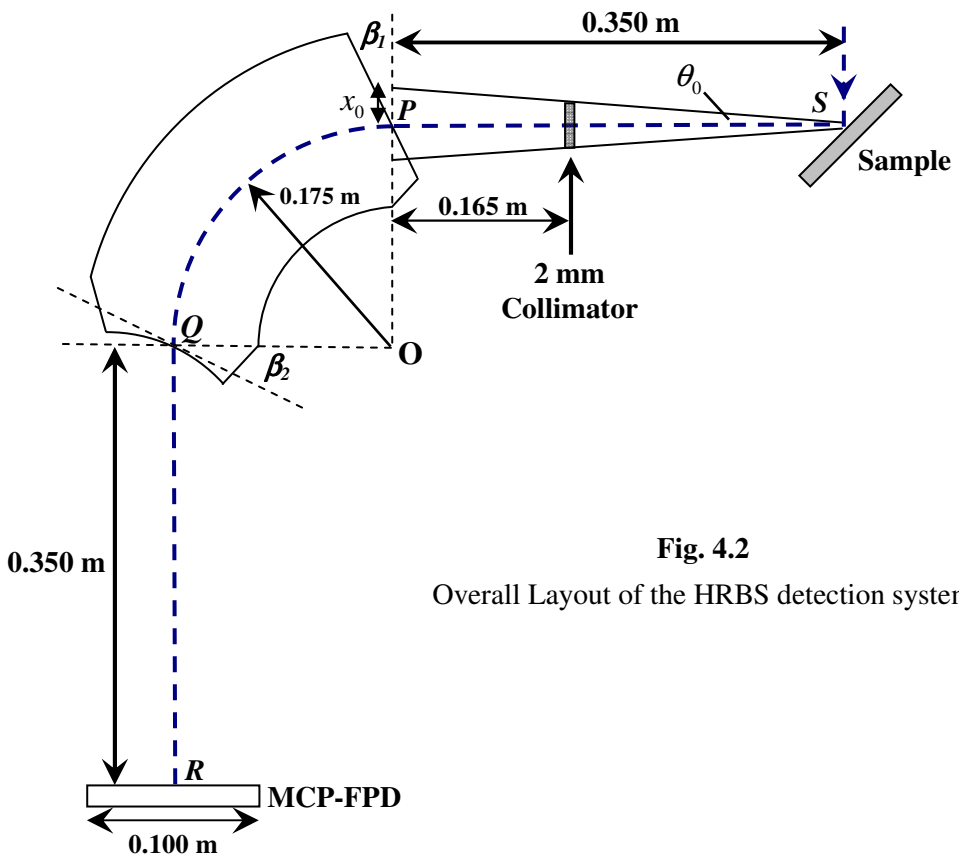

Fig. 4.2
Overall Layout of the HRBS detection system

A 90º sector magnet of radius ρ_0 with flat entrance and exit edges that are both rotated at 26.6º is expected to produce a stigmatic image of a point source at both object and image distances of $2\rho_0$. The HRBS spectrometer and detection setup is designed to produce a stigmatic image according to this principle. The incident beam backscatters from the sample at *S* enters the magnet at *P*, after passing through a 2 mm collimator which defines the backscattered beam divergence. Ions following a trajectory with a radius of ρ_0 = 0.175 m will exit the magnet at *Q* and impact at the midpoint along the MCP-FPD assembly at *R*, assuming that no fringe fields were present. The target (object) distance $\overline{SP}$ and the MCP-FPD (image) distance $\overline{QR}$ are both set at $2\rho_0 = 0.350$ m to obtain a stigmatic image on the MCP.

4.4 Effect of curvature of spectrometer exit edge

The focal plane of the spectrometer is determined by the shape of the exit edge. Here the effect of the curvature of the exit edge of the spectrometer on its focal plane is investigated using a simple program written using the Mathematica software. Two magnets, one with a flat exit edge and another with a circular exit edge, were simulated using the actual scattering layout (Fig. 4.3).

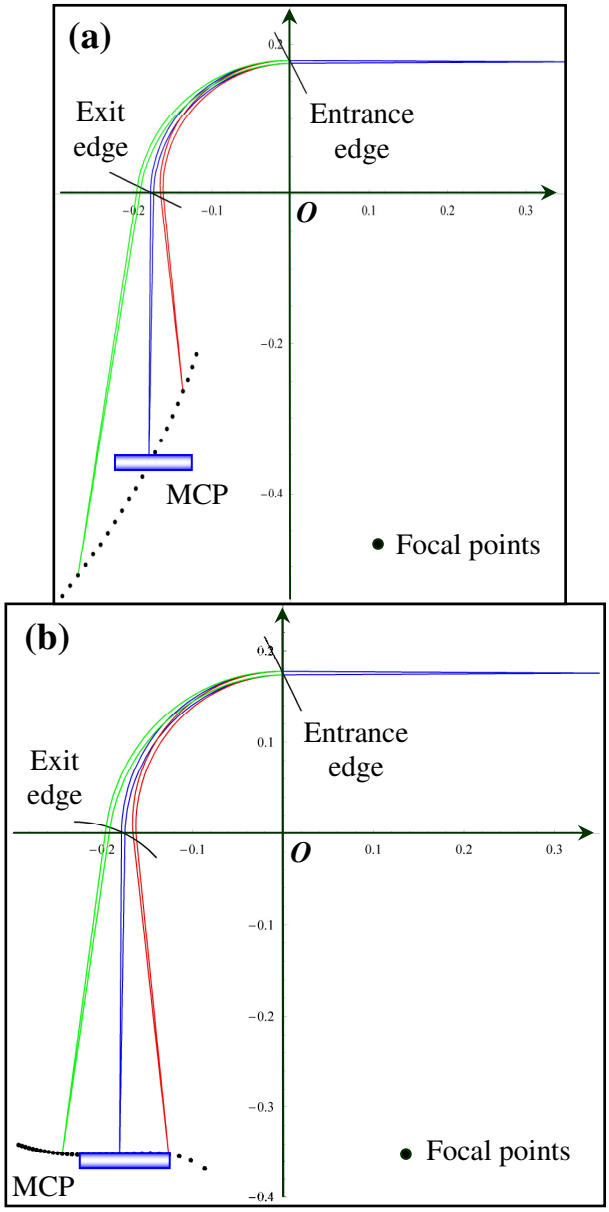

Fig. 4.3 Focal point calculations for magnet with **(a)** Flat exit edge **(b)** Circular exit edge. The focal points are calculated by varying the beam energy in steps of 1.4% about a central beam energy (blue trajectory) of 475 keV through a spectrometer field of 1.0 T. The scales of the axes are in metres.

The origin *O* of the *x*-*y* axes is set at the centre of the trajectory with radius of ρ_0, and a point source of ions is assumed to be at an object distance of $2\rho_0$. Lines are drawn to simulate the envelope of a beam with the maximum angular divergence allowed by the 2 mm collimator between the target and the magnet entrance. The circular trajectories within the magnet with radii ρ corresponding to ion energy *E* as given by the relationship in section 4.2 are then drawn so that the incident beam envelopes are tangential to the trajectories at the magnet entrance edge. Similarly, exit beam envelopes outside the magnet are drawn as straight lines that are tangential to their respective circular trajectories at the exit edge. The details of the trajectory constructions are given in the description of Direct analytical calculations in section 4.5.3. The intersections between the exit beam envelopes are then assumed to be the focal point for that particular energy. Focal points for varying ion energy *E* are then plotted out at a fixed field strength *B*.

Fig. 4.3(a) and (b) show the focal point plots for magnets with flat and circular exit edges respectively. The focal points for the flat exit edge lies along a line with a significant slope relative to the *x*-axis, while the focal points for the circular exit edge follow a line that is essentially parallel to the *x*-axis at a distance of $2\rho_0$, where the plane of the MCP is located. In effect, the curvature of the exit edge tilts the focal plane of the flat edge so that it becomes parallel to the *x*-axis and the design of the detection setup places the MCP along that plane. To conclude, this simple study has shown that both the curvature of the HRBS spectrometer exit edge and the placement of the MCP are correct: the circular exit edge of the spectrometer creates a focal plane parallel to the *x*-axis where MCP is placed.

4.5 Analytical studies of spectrometer ion optics

Introduction

In the last section, focal points are calculated at the intersection of the beam envelopes in order to plot out the focal plane. Here, we study the intersections of the exit beam with the MCP at varying beam energy *E*. Since the FPD determines the energy of an ion according to the ion's position of incidence along its length after exiting the magnet, all calculations are based on the projection of the ion beam onto the median (*x*-*y*) plane. The calculations are performed for various *E* so as to sweep the ion incidence position across the length of the MCP to study the behaviour of the position of the beam incidence along the MCP as the beam energy is varied.

Analytical calculations using two different approaches were adopted for the trajectories within the magnet: the Direct and the Matrix approach. Both of these approaches calculate the ion trajectories before and after the magnet, as well as the beam incidence position along the MCP, in the same manner. The only difference between the approaches is the calculation of ion trajectories within the magnet. The Direct approach constructs circles as the ion trajectories in the similar manner as section 4.4, correcting for the rotated entrance edge and beam divergence. The Matrix approach uses a matrix-transport theory developed by Penner [39] to calculate the exit beam parameters, given the entrance parameters. The matrix was developed also by considering circular trajectory construction, but with first-order approximations for small-divergence beams in order to simplify the calculations. These two approaches will be separately described in detail, and their results compared with the SIMION numerical modeling and the experimental results.

4.5.1 Beam entry parameters

The backscattered ion beam entering the magnet is calculated in the same manner in both Direct and Matrix calculations. The ion beam was assumed to have incident on a target tilted at 45° with IBM geometry (Fig. 4.4), which conforms to the experimental conditions of a HRBS calibration process. The incident beam spot size on the target is 1×1 mm as seen along the target normal. Particles backscattered at a scattering angle of 65° will form a beam of half-width $w = 0.5\times10^{-3}\sin 20^{\circ}$ (metres) that will subsequently be collimated by a 2 mm collimator placed between the target in the scattering chamber and the magnet entrance.

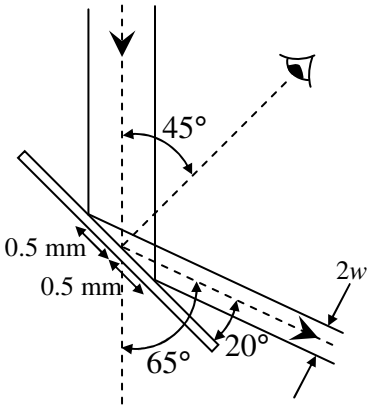

Fig 4.4 Schematic of the incident and backscattered beam profiles

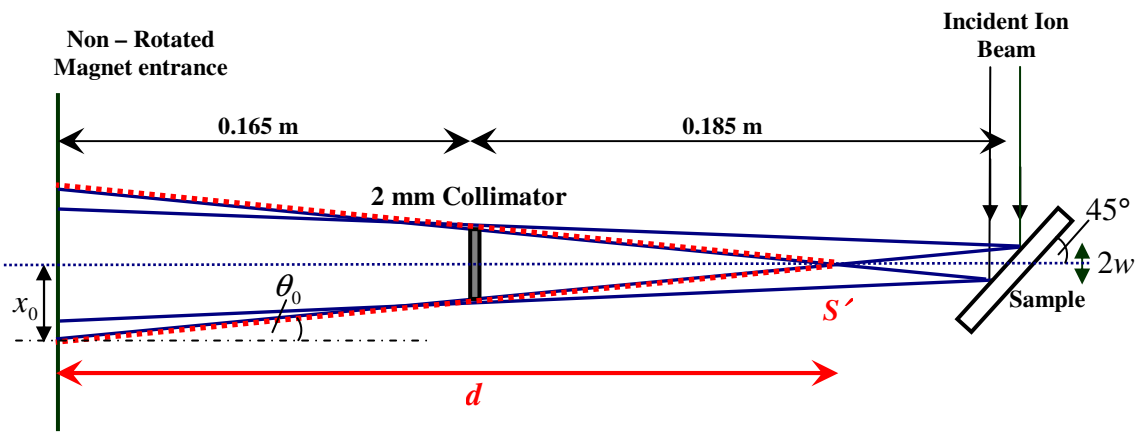

Fig. 4.5 Finite backscattered beam profile and point source approximation

The total distance between the beam spot on the target and the magnet entrance is 0.350 m, and the collimator is 0.165 m from the magnet entrance, as shown in Fig. 4.5. Due to the finite size of the incident beam, the outermost ions of the incident beam form cone-shaped envelopes that represent the maximum possible divergence of the backscattered beam (blue) through the collimator. The union of all such envelopes therefore determines the overall entry beam envelopes of the backscattered ions into the magnet, as shown in Fig. 4.5. It can be shown that a point source at point S' at a distance d from the magnet entrance will form maximum-divergence envelopes (red) that exactly contain all envelopes formed by the finite incident beam. The point beam at S' was therefore used as an equivalent of the finite beam in both Direct and Matrix calculations. By similar triangles, we have

$$\frac{0.001}{d-0.165}=\frac{w}{0.350-d} \quad \Rightarrow \quad d=\frac{0.350(0.001)+(0.165)w}{0.001+w}$$

4.5.2 Fringe field correction

The fringe fields cause additional bending of the ion trajectories before the entrance edge and after exit edge. We can account for the bending properties of the fringe fields along the median plane for our analytical calculations by assuming that the fringe field extends outward equally at the entrance and exit edges. This can be approximated to the first order by assuming that the magnet is physically larger by a distance of f at both edges as shown in Fig. 4.6, while retaining the sharp drop-off model for the static magnetic field between the magnet poles.

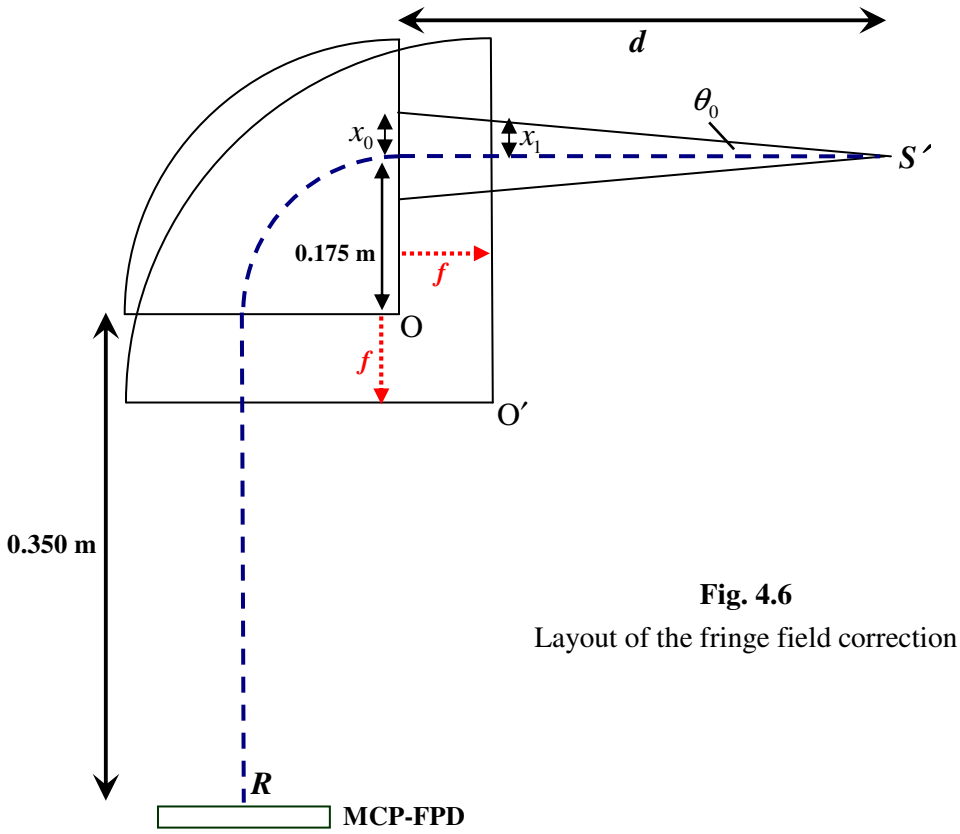

Fig. 4.6
Layout of the fringe field correction

The distance f was adjusted so that the analytical calculations agree with SIMION results obtained for an ion of energy E_0 passing through the magnet of field strength B_0 and hitting the MCP at point R at the exact midpoint of its length. This step normalized both approaches to the single data point at R, and is justified since our only interest is to know how all other ion trajectories behave relative to the beam that hits the MCP at R. The size of the magnet increases and the origin is shifted from O to O′. The equation of the exit edge is therefore:

$$(x+0.23128+f)^2+(y+0.11239)^2=(0.12569)^2$$

The MCP-FPD plate is along the plane:

$$y=-0.350+f$$

The equivalent point source S' is now closer to the entrance with coordinates:

$$S'(Sx',Sy') = S'(d-f,\ 0.175+f)$$

4.5.3 Direct calculations

Entry parameters

A point source at $S'(Sx', Sy')$ produces two lines which are the "top" and "bottom" beam envelopes that define a beam divergence of 2θ, as shown in Fig. 4.7.

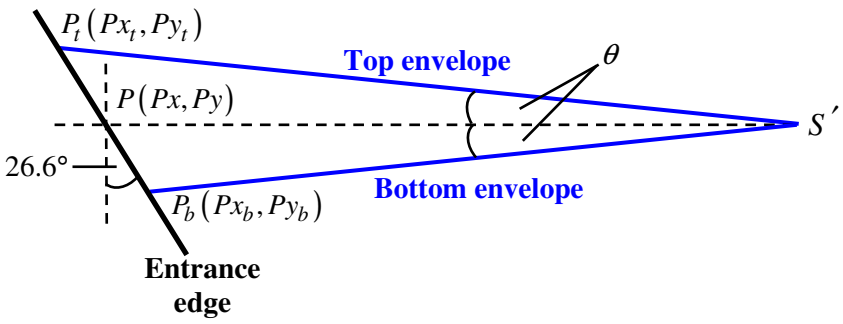

Fig. 4.7 Schematic of backscattered beam envelopes from point source

The top and bottom envelopes have equations

$$y = -x\tan\theta + [Sy' + Sx'\tan\theta] \quad \text{and} \quad y = x\tan\theta + [Sy' - Sx'\tan\theta]$$

respectively, while the equation of the entrance edge is given by

$$y = -x\cot(26.6^\circ) + (0.175 + f)$$

Solving these equations yields respectively the points of intersection $P_t(Px_t, Py_t)$ and $P_b(Px_b, Py_b)$ of the top and bottom envelopes with the entrance edge.

Trajectories within magnet

Circles are drawn within the magnet as trajectories for the top and bottom envelopes so that each envelope is a tangent to its respective circle. Since the envelopes are fixed, the circles have to be shifted to account for the tilt in entrance edge, as well as the gradient of the envelopes. We start with a central trajectory (red) in Fig 4.8 with

radius ρ and centre at $(0, 0.175 + f - \rho)$ where a horizontal beam with zero divergence forms a tangent at point $P_0(Px, Py)$ at the topmost point of the circle. The central trajectory is then separately shifted to form the top (violet) and bottom (green) trajectories such that their uppermost points are $P_t(Px_t, Py_t)$ and $P_b(Px_b, Py_b)$ respectively.

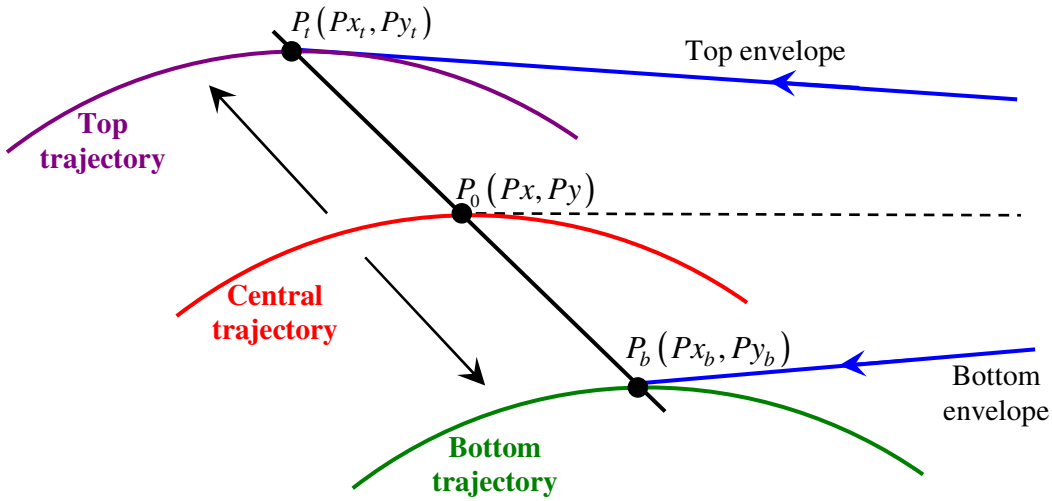

Fig. 4.8 Schematic of translations of central trajectory due to slanted entrance edge.

The translations for the top and bottom trajectories are therefore given by:

$$\{x \to x + (Px - Px_t),\ y \to y - (Py_t - Py)\}$$

and

$$\{x \to x - (Px_b - Px),\ y \to y + (Py - Py_b)\}$$

respectively. However, these translated circular trajectories have horizontal tangents at P_t and P_b, and do not take into account the beam divergence angle. An additional transformation is required on the trajectories so that the incident envelopes become their respective tangents. This is accomplished by translating the circles yet again so that the points P_t and P_b coincide with the specific parts of the circle with the same gradients as the top and bottom envelopes respectively, as illustrated in Fig. 4.9.

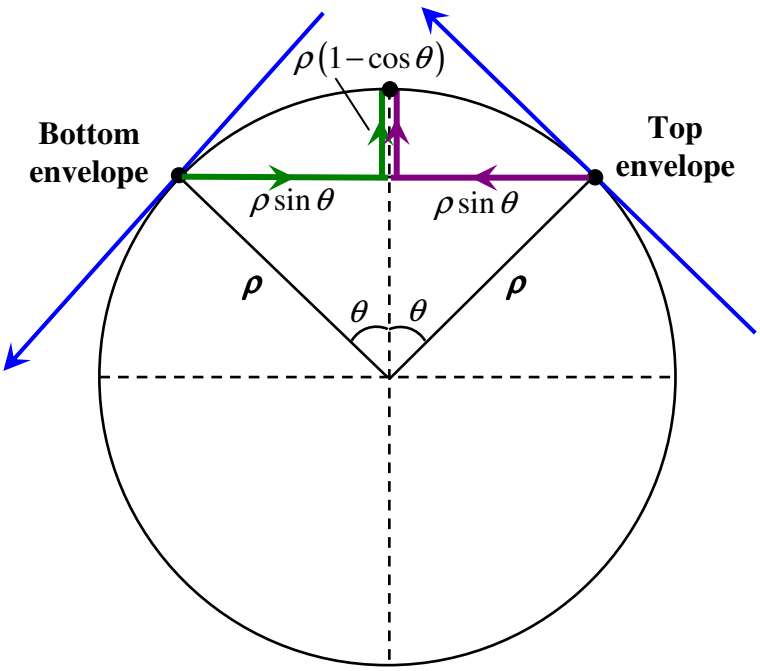

Fig. 4.9 Schematic of trajectory transformations due to beam divergence

The additional transformations required are:

$$\text{Top:} \quad \left\{ x \to x + \rho\sin\theta,\ y \to y - \rho(1-\cos\theta) \right\}$$

$$\text{Bottom:} \quad \left\{ x \to x - \rho\sin\theta,\ y \to y - \rho(1-\cos\theta) \right\}$$

Hence the final equations of the top and bottom circular trajectories constructed within the magnet are:

$$\left[x + (Px - Px_t) + \rho\sin\theta\right]^2 + \left[y - (0.175 + f - \rho) - (Py_t - Py) - \rho(1-\cos\theta)\right]^2 = \rho^2$$

and

$$\left[x - (Px_b - Px) - \rho\sin\theta\right]^2 + \left[y - (0.175 + f - \rho) + (Py - Py_b) - \rho(1-\cos\theta)\right]^2 = \rho^2$$

respectively.

Exit parameters and MCP incidence

The equation of the magnet exit edge is:

$$\left(x+0.23128+f\right)^2+\left(y+0.11238\right)^2=0.12569^2$$

Solving the top and bottom trajectories with the above exit edge equation yields the respective exit points $Q_t\left(Qx_t,Qy_t\right)$ and $Q_b\left(Qx_b,Qy_b\right)$. The gradients G_t and G_b of the top and bottom exit beams are determined from the gradient of the radius vector joining the exit point and the centre of the trajectory:

$$G_t=-\left[\frac{\left[\left(0.175+f-\rho\right)+\left(Py_t-Py\right)+\rho\left(1-\cos\theta\right)\right]-Qy_t}{\left[-\left(Px-Px_t\right)-\rho\sin\theta\right]-Qx_t}\right]^{-1}$$

$$G_b=-\left[\frac{\left[\left(0.175+f-\rho\right)-\left(Py-Py_b\right)+\rho\left(1-\cos\theta\right)\right]-Qy_b}{\left[\left(Px_b-Px\right)+\rho\sin\theta\right]-Qx_b}\right]^{-1}$$

The equations of the exit beams are therefore:

$$y=Qy_t+G_t\left(x-Qx_t\right) \qquad \text{and} \qquad y=Qy_b+G_b\left(x-Qx_b\right)$$

for the top and bottom exit beams respectively. These are then solved with the MCP equation given by

$$y=-0.350+f \quad , \quad \left\{-0.225\le x\le -0.125\right\}$$

The domain is limited to ± 50 mm from the centre of the MCP at $\left(-0.175,-0.350\right)$, due to its finite physical length along that plane. The beam-incidence centroid is assumed to be the midpoint between the intersection points along the MCP and are plotted out and compared to results from the Matrix and Numerical calculations as well as the experimental data at the end of this chapter. The layout of the Direct calculations is shown in Fig 4.10.

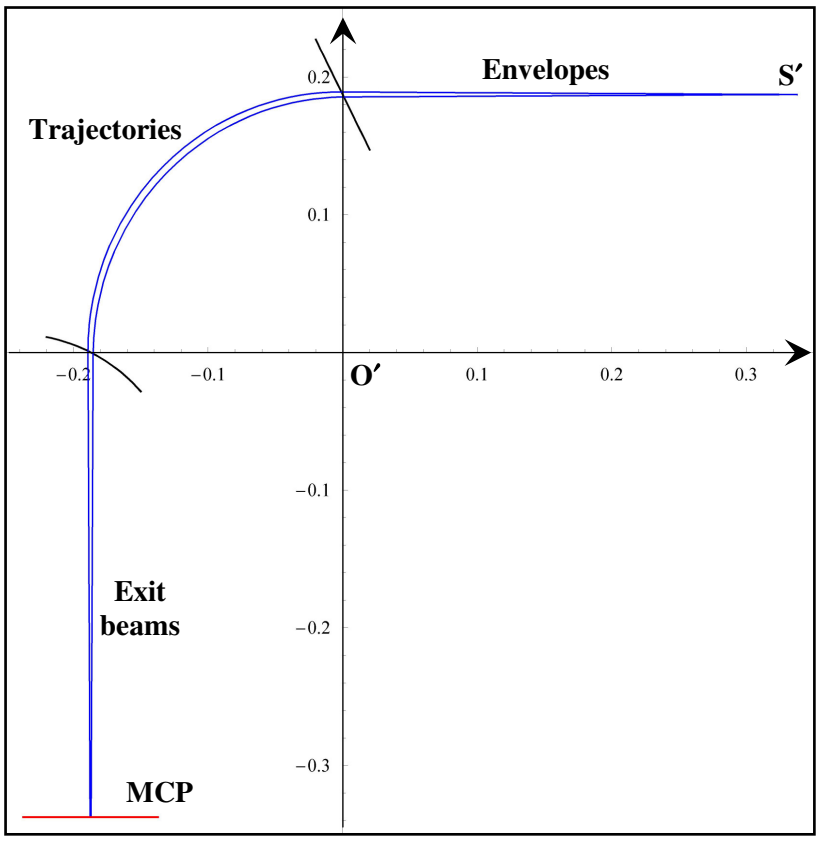

Fig. 4.10 Layout of the Direct calculations in Mathematica.

4.5.4 Matrix calculations

Introduction

First-order bending and focusing properties of magnetic deflection systems had been extensively investigated in the 1950s and 1960s. Simplifications to calculations of ion trajectories were beneficial in those days as personal computers were not readily available for such analyses, and analytical equations with closed form were developed so that analyses could be performed “by hand”. In particular, discussions had been made on the conditions for double-focusing in sector-shaped magnetic spectrometers with uniform fields [41 – 43]. Ion trajectories are constructed using the sharp drop-off model of the field at the magnet edges, and the conditions for a stigmatic image in

both the vertical and the median planes are determined from the geometry of the trajectories. Properties of such magnetic systems are simplified using a matrix approach as described by Penner [39], and this was adopted for our Matrix calculations of ion trajectories in the HRBS spectrometer.

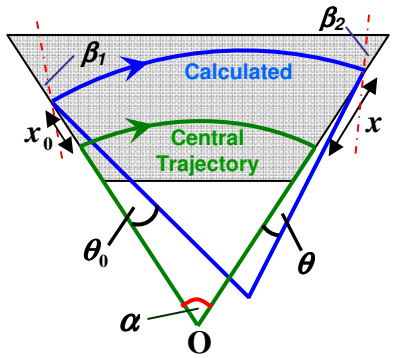

Fig. 4.11 Schematic of Matrix approach by Penner

In Penner's approach, circular trajectories of ions were constructed within the median plane of a bending magnet with a static, uniform field. The geometry of the setup is shown in Fig. 4.11. The central trajectory is one that is perpendicular to both (non-rotated) entrance and exit edges for a particular ion energy. An ion having momentum p travels along a circular trajectory of radius ρ with its entrance and exit points subtending an angle α about the centre O. Another ion entering the magnet with momentum $p' = p + \Delta p$ at a small angle θ_0 and displacement x_0 relative to the central trajectory will exit the magnet at an angle θ and displacement x with its momentum unchanged in magnitude. A matrix approach was then developed to obtain the exit parameters x and θ for every set of entrance parameters x_0 and θ_0. The effects of rotated (flat) entrance and exit edges by angles β_1 and β_2 respectively were incorporated into the matrix. Stable, well-collimated ion beams have small angular and momentum spreads, as well as small cross-sectional dimensions as compared to the bending radius of the spectrometer magnet. First order effects will dominate for

such ion beams and higher-order effects may be ignored. By considering the geometry of the setup with first-order small angle approximations, the exit parameters of the calculated ion trajectory can be obtained by the relation:

$$\begin{pmatrix} x \\ \theta \\ \frac{\Delta p}{p} \end{pmatrix} = M\ (\alpha, \beta_1, \beta_2) \begin{pmatrix} x_0 \\ \theta_0 \\ \frac{\Delta \rho}{\rho} \end{pmatrix}$$

where

$$M = \begin{pmatrix} \frac{\cos(\alpha - \beta_1)}{\cos \beta_1} & \rho \sin \alpha & \rho(1 - \cos \alpha) \\ \frac{-(1 - \tan \beta_1 \tan \beta_2)\sin(\alpha - \beta_1 - \beta_2)}{\rho \cos(\beta_1 + \beta_2)} & \frac{\cos(\alpha - \beta_2)}{\cos \beta_2} & \sin \alpha + (1 - \cos \alpha)\tan \beta_2 \\ 0 & 0 & 1 \end{pmatrix}$$

The fractional change in momentum of the ion $\Delta p / p$ is equal to the fractional change in the ion trajectory radius in the magnet $\Delta\rho / \rho$, and in our case, $\Delta p = \Delta\rho = 0$. The same layout as the Direct calculations (Fig. 4.10) is used here.

Entry parameters

The framework developed in 4.5.1 is adopted here in order to obtain the entry parameters. From Fig. 4.5 we obtain:

$$x_0 = \frac{d - f}{d - 165} \quad \text{and} \quad \theta_0 = \tan^{-1} \frac{1}{d - 165}$$

Determination of α, β_1 and β_2

The matrix M requires the determination of three variables for every ion energy E: α, β_1 and β_2. The angle α of an ion with energy E was calculated by finding the

coordinates of the entrance and exit points of the central trajectory of radius ρ from a horizontal beam of zero divergence. Consider the case of $\rho < \rho_0$ in Fig. 4.12.

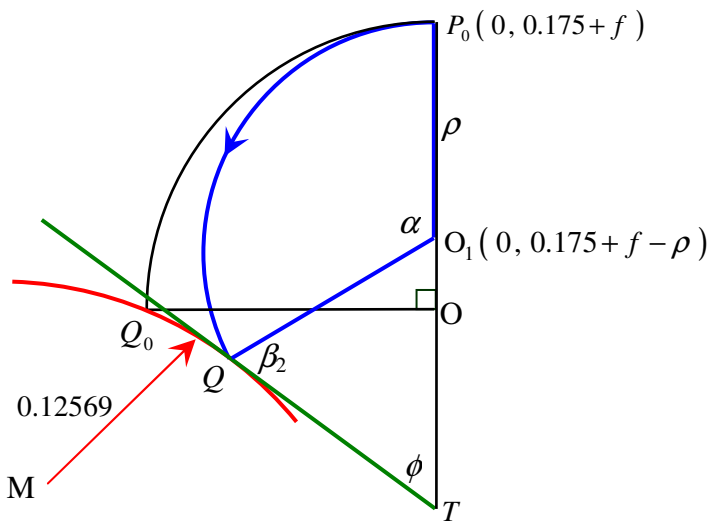

Fig. 4.12 Layout of the calculation for entrance parameter α

Let O be the origin and P_0Q_0 be the trajectory for an ion with radius $\rho_0 = 0.175$. All horizontal backscattered beams enter the magnet at the same point $P_0(0, 0.175+f)$ regardless of the energy of the ion. An ion of energy E has a trajectory P_0Q of radius ρ and centre at $O_1(0, 0.175+f-\rho)$. The tangent of the exit edge of the magnet (red) at Q meets the y-axis at T. The equation of the trajectory P_0Q is:

$$x^2 + \left[y - (0.175 + f - \rho)\right]^2 = \rho^2$$

while the equation of the circular exit edge of the magnet is as before:

$$(x + 231.28 + f)^2 + (y + 112.39)^2 = (125.69)^2$$

with the centre at $M(Mx, My) = M(-231.28 - f, -112.38)$. The appropriate solution of the above two equations gives us the exit point $Q(Qx, Qy)$. The angle α was then calculated from the coordinates of Q and P_0 with

$$\mathrm{O}_1 P_0 = \mathrm{O}_1 Q = \rho \quad \Rightarrow \quad 2\rho \sin\left(\frac{\alpha}{2}\right) = \overline{P_0 Q},$$

where $\overline{P_0 Q}$ is the length of the chord joining P_0 and Q. We therefore have

$$\alpha = 2\sin^{-1}\left(\frac{\overline{P_0 Q}}{2\rho}\right)$$

The magnet entrance edge is straight, and since all ions enter horizontally at P_0,

$$\beta_1 = 26.6°$$

The exit edge rotation angle β_2 is defined as the angle between the actual exit edge and the trajectory radius vector $\overrightarrow{\mathrm{O}_1 Q}$ at the exit point Q. In this case β_2 is given by $\angle\, O_1 QT$, where QT is the tangent of the circular exit edge at the ion exit point $Q(Qx, Qy)$. Using the gradient of the exit edge radius vector $\overrightarrow{M\,Q}$, we have

$$\tan\phi = \frac{Qy - My}{Qx - Mx} = \frac{Qy + 0.11238}{Qx + 0.23128 + f}$$

$$\Rightarrow \beta_2 = \alpha - \phi = \alpha - \tan^{-1}\left(\frac{Qy + 0.11238}{Qx + 0.23128 + f}\right)$$

Correction to exit parameters due to circular exit edge

Once the parameters α, β_1 and β_2 were established, the matrix M provides us with the exit parameters x and θ given the entry parameters x_0 and θ_0. We note that all entry and exit parameters are expressed relative to the unique central trajectory $P_0 Q$ for every ion energy E. However, the original matrix approach assumed that the rotated exit edge is flat, not circular. Due to the small magnitudes of θ_0 and θ, the effect of the curvature of the real exit edge may be significant. Hence a correction is developed here for the exit parameter θ due to the exit edge curvature.

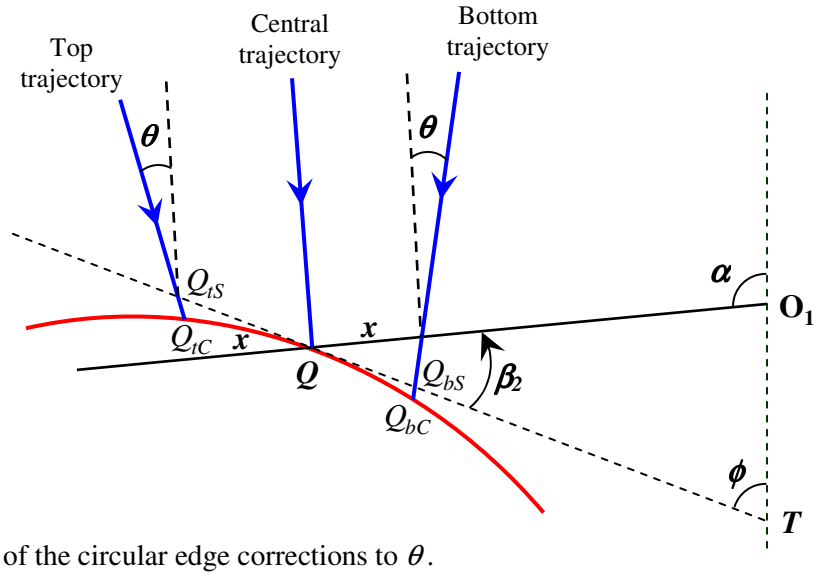

Fig 4.13 Schematic of the circular edge corrections to θ.

Schematically shown in Fig. 4.13, the original derivations assumed a straight rotated exit edge at the point of exit Q for an ion of energy E and subtending an angle of α. This edge is the tangent $Q_{tS}\,Q_{bS}$ of the exit edge at Q that makes an angle of ϕ with the vertical at T. However, the true magnet edge $Q_{tC}\,Q_{bC}$ is circular, causing the beam envelope to be bent more on either side of Q. The top and bottom beam envelopes on each side of the central trajectory travel additional distances of $Q_{tS}\,Q_{tC}$ and $Q_{bS}\,Q_{bC}$ respectively, which are equal to the first order. The arc lengths $Q_{tC}\,Q$ and $Q_{bC}\,Q$ were also assumed to be approximately equal in lengths as $Q_{tS}\,Q$ and $Q_{bS}\,Q$ respectively. Since θ is small and the radius of the exit edge is 0.12569 m,

$$\overline{Q_{bC}\,Q} \approx \overline{Q_{bS}\,Q} = x\sec\beta_2 \qquad \text{and} \qquad \angle Q_{bC}\,Q\,Q_{bS} = \frac{\overline{Q_{bC}\,Q}}{0.12569} \approx \frac{x\sec\beta_2}{0.12569}$$

for the top envelope, which will then give us the angular correction factor to θ:

$$\varphi = \frac{\overline{Q_{bC}\,Q_{bS}}}{\rho} = \frac{2\,\overline{Q_{bS}\,Q}}{\rho}\sin\left(\frac{\angle Q_{bC}\,Q\,Q_{bS}}{2}\right) = \frac{2x\,\sec\beta_2}{\rho}\sin\left(\frac{x\,\sec\beta_2}{0.25138}\right)$$

The adjusted θ for the top and bottom envelopes are therefore

$$\theta_t = \theta + \varphi \qquad \text{and} \qquad \theta_b = \theta - \varphi$$

Position of ion incidence along MCP

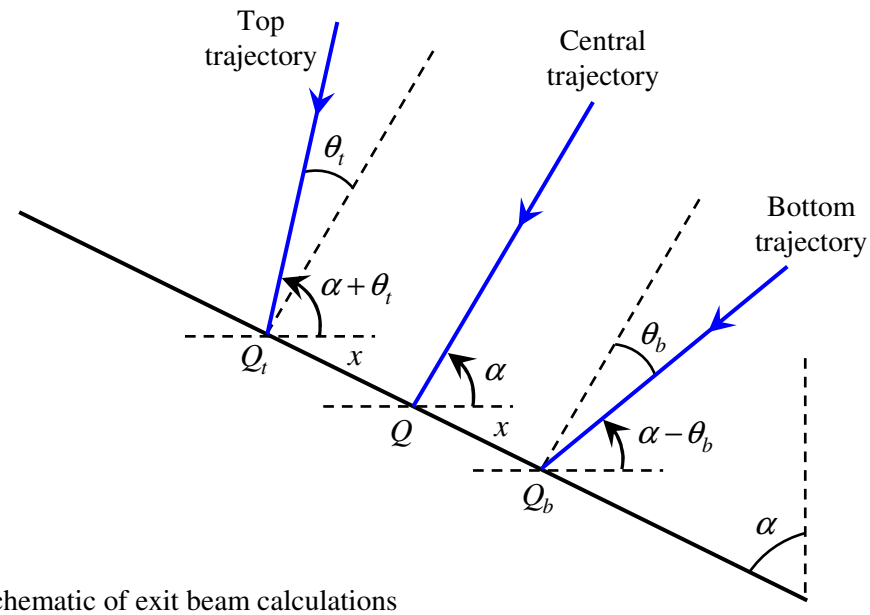

Fig. 4.14 Schematic of exit beam calculations

The exit parameters x, θ_t and θ_b allow us to find the equations of the straight exit beams of the trajectories outside the magnet. Consider the case where $\rho < \rho_0$ in Fig. 4.14. Since the exit point $Q(Qx, Qy)$ of the central trajectory has already been determined, the exit points $Q_t(Q_t x, Q_t y)$ and $Q_b(Q_b x, Q_b y)$ of the top and bottom trajectories are calculated in relation to Q:

$$(Q_t x) = (Qx) - x\sin\alpha \quad , \quad (Q_t y) = (Qy) + x\cos\alpha$$

$$(Q_b x) = (Qx) + x\sin\alpha \quad , \quad (Q_b y) = (Qy) - x\cos\alpha$$

Since the distances $Q_{tS}\,Q_{tC}$ and $Q_{bS}\,Q_{bC}$ are insignificant as compared to $x\sin\alpha$ and $x\cos\alpha$, we can ignore the distinction between points on the circular or flat edge in this case and assume for simplicity that all exit points are along the straight line tangential to Q, dropping the subscripts S and C. The equations of the exit beams are:

$$\text{Top:} \quad y = x\tan(\alpha+\theta_t) + \left[(Q_t y) - (Q_t x)\tan(\alpha+\theta_t)\right]$$

$$\text{Bottom:} \quad y = x\tan(\alpha-\theta_b) + \left[(Q_b y) - (Q_b x)\tan(\alpha-\theta_b)\right]$$

In a similar manner to the Direct equations, the exit beam equations are then solved with the MCP equation $y = -0.350 + f$ with $-0.225 \le x \le -0.125$ and the beam-incidence centroid is the midpoint between the intersection points along the MCP.

4.5.5 Comparison of results from Direct and Matrix calculations

The results of the Direct and Matrix calculation are shown in Fig 4.15.

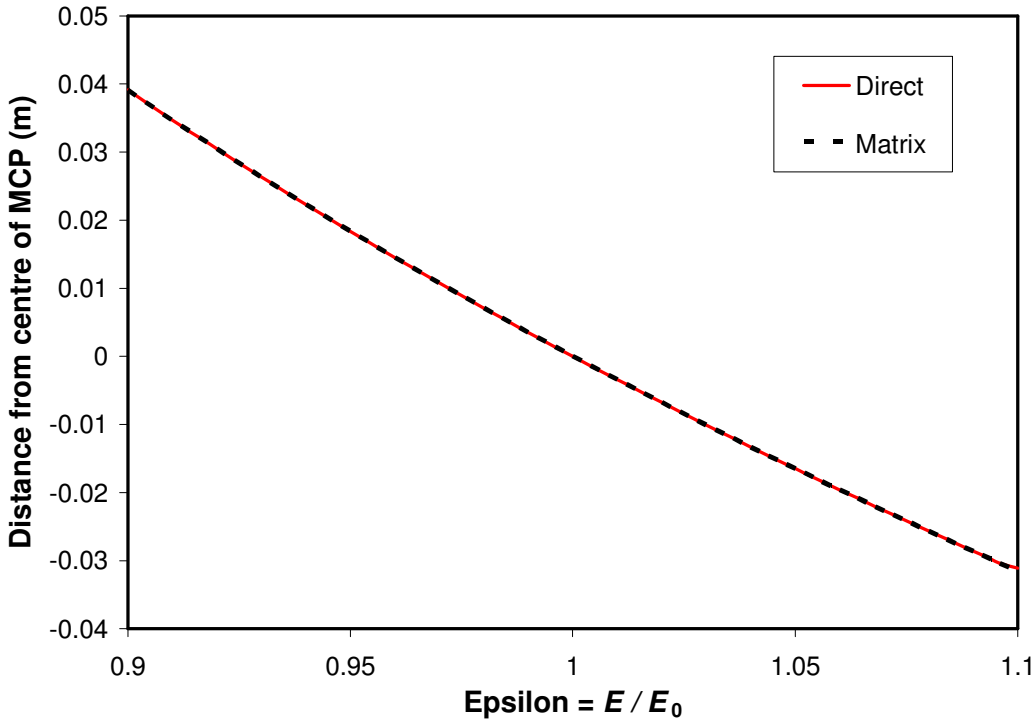

Fig. 4.15 Plot of the distance from the centre of the MCP vs epsilon, defined as the ratio of the ion energy E and the energy E_0 of the ion which hits the midpoint along the MCP.

The results from the Direct and Matrix calculations show almost perfect agreement, which is as expected as they have almost the same structure. Both calculations solve for the entrance and exit points (P and Q) by using a circular trajectory of radius ρ for every ion energy E. The main difference between them is the first-order small angle approximations made in matrix M by assuming that the beam divergence is small, which is indeed the case in the HRBS detection setup.

4.6 Numerical simulation of ion trajectories using SIMION

Overview

SIMION 3D version 7.0 ion optics simulation program [40] had been used to perform numerical simulation of the ion trajectories through the spectrometer magnet. The program allows for exact shape of the magnetic pole pieces to be drawn within a virtual 3-dimension grid-like universe. Due to the fact that both the divergence and curl of static magnetic fields in vacuum are zero, the program was allowed to assign magnetic scalar potentials to every non-pole grid point. Numerical solutions to Maxwell's equations were then obtained by computing potential gradients at every point within the grid. Alpha particles were "created" at a particular starting point and assigned a starting energy E. Their subsequent trajectory were determined by calculating the potential gradients and hence the magnetic forces along the x,y and z directions at the ion's position at every time step. A fourth-order Runge-Kutta algorithm was then used to perform numerical integration needed to obtain the ion's trajectories for various values of E, and the corresponding positions of ion incidence onto the MCP are recorded and compared to the experimental data.

4.6.1 Drawing the magnet

The program simulates a 3-dimensional universe called workbench that is divided into grids. The centre of each grid cube is known as a grid point, while the separation between 2 adjacent grid points is known as a grid unit. Grid points are divided into 2 types: electrode points and non-electrode points. The size of the workbench was first defined, followed by the drawing out of the exact shape of the magnetic pole pieces (known as electrodes within SIMION). Drawing a pole piece is done by deciding the

set of grid points to be defined as electrode points, while the rest of the grid points are designated to be non-electrode points.

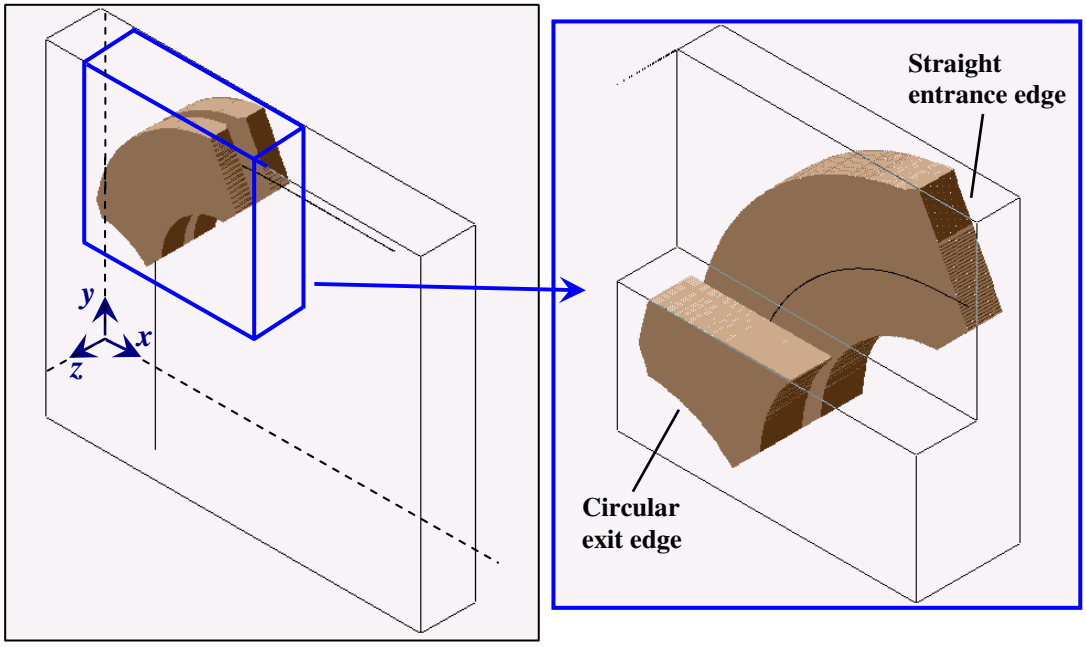

Fig. 4.16 3-dimensional isometric view of the workbench with a magnified view of the spectrometer magnet. One of the pole pieces was cut to show the ion trajectory between the pole pieces.

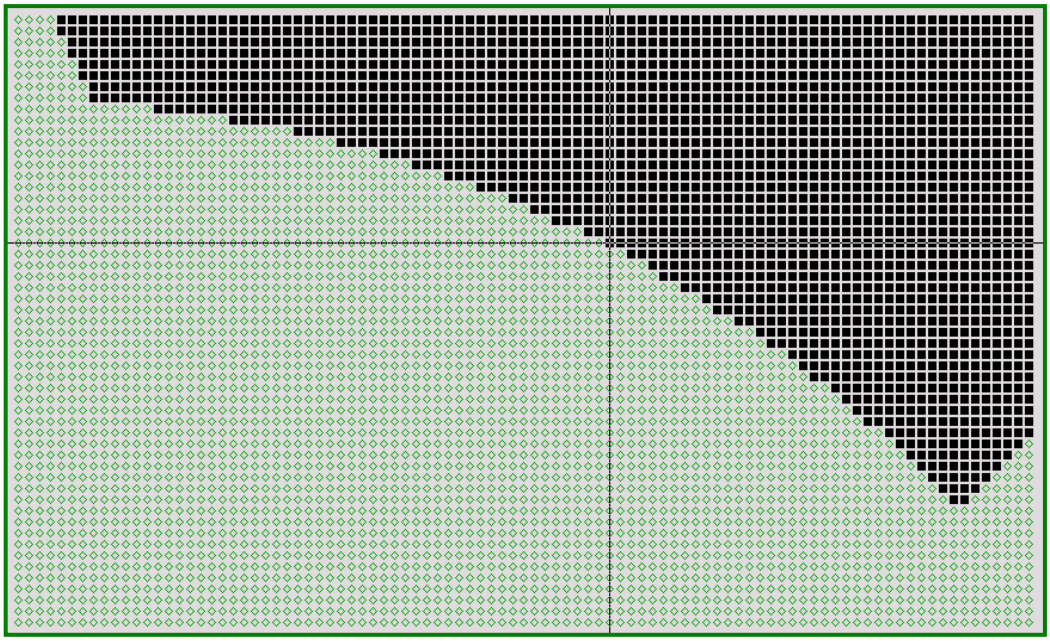

Fig. 4.17 Blown up view of the exit edge along the *x*-*y* plane. The black squares are electrode points, while the green circles are non-electrode points. The intersection of the solid lines is the exit point for ions following the trajectory with radius equal to the magnet bending radius.

The exact shape of the HRBS spectrometer magnet was drawn using a geometry file where exact geometrical shapes were drawn using its in-built definition language. The pole pieces were separated by 18 mm, while their thicknesses were drawn out to be 40 mm. The exact thickness along the *z*-direction was not simulated because only the shape and the magnetic potential at their boundaries define the magnetic field between them. The inner boundary edges are filed at an angle of 45° at both the magnet entrance and exit.

4.6.2 Maxwell's and Laplace's equations

The general Maxwell's equations for electric and magnetic fields in vacuum are

$$\nabla \cdot \mathbf{E} = \frac{\rho}{e} \qquad \nabla \cdot \mathbf{B} = 0$$

$$\nabla \times \mathbf{E} = -\frac{\partial \mathbf{B}}{\partial t} \qquad \nabla \times \mathbf{B} = \mu_0 \varepsilon_0 \frac{\partial \mathbf{E}}{\partial t}$$

For static fields in regions not containing any electrical charges, these equations reduce to

$$\nabla \cdot \mathbf{E} = 0 \qquad \nabla \cdot \mathbf{B} = 0$$

$$\nabla \times \mathbf{E} = 0 \qquad \nabla \times \mathbf{B} = 0$$

Since both curls are zero, we can express both **E** and **B** in terms of scalar potentials:

$$\mathbf{E} = -\nabla \mathrm{V_E} \qquad \mathbf{B} = -\nabla \mathrm{V_B}$$

Because both divergences are also zero, we arrive at the Laplace's equations

$$\nabla^2 \mathrm{V_E} = 0 \qquad \nabla^2 \mathrm{V_B} = 0$$

whose solutions are Harmonic functions. Since only magnetic fields were involved in our case, the subscripts are dropped and V refers to the scalar magnetic potentials. Gauss's Mean Value Theorem for harmonic functions requires that the value V of a

harmonic function at any point to be equal to the arithmetic mean of its values on the surface of a closed region containing that point. There are no local maxima or minima for the solutions, the magnetic potential gradients vary smoothly along all directions at all points.

4.6.3 Refining the magnet array

All electrode points within a single magnetic pole piece share the same magnetic potential. A non-zero potential was chosen for the north pole at the top while the potential of the south pole at the bottom was set at zero. These electrode potentials form the Dirchlet boundary condition which ensures the uniqueness of the harmonic solutions to Laplace's equation. All non-electrode points outside the poles begin with their potentials set at zero.

The next step was to solve the Laplace's equation numerically to determine the magnetic potentials for all non-electrode points within the workbench that will reflect the correct magnetic field (called "refining the array" in SIMION). Due to the mean value property of harmonic functions, refining the array is essentially a process of assigning a potential to each non-electrode point that is equal to the average value among those of the neighbouring points. SIMION does this sequentially and over a number of iterations. During each iteration, the program sequentially calculates for every non-electrode point within the array the average potential of the 6 neighbouring points in the 3-dimensional workbench (Fig 4.18). The program then assigns this average value to that point.

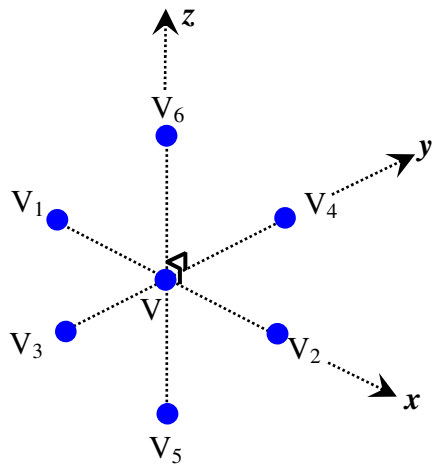

$$V = \frac{V_1 + V_2 + V_3 + V_4 + V_5 + V_6}{6}$$

Fig. 4.18 Schematic of magnetic potential calculations for every point in the workbench.

As the iterations were repeated, the potentials were propagated from the electrode points outwards to all non-electrode points away from the poles. The change in the potential of each non-electrode point across successive iterations decreases as the number of iterations increases, and the iterations were set to cease only when the potential of any non-electrode point within the workbench changes by less than 0.0001 V between two successive iterations, at which time the potential distribution within the workbench was considered to be set up.

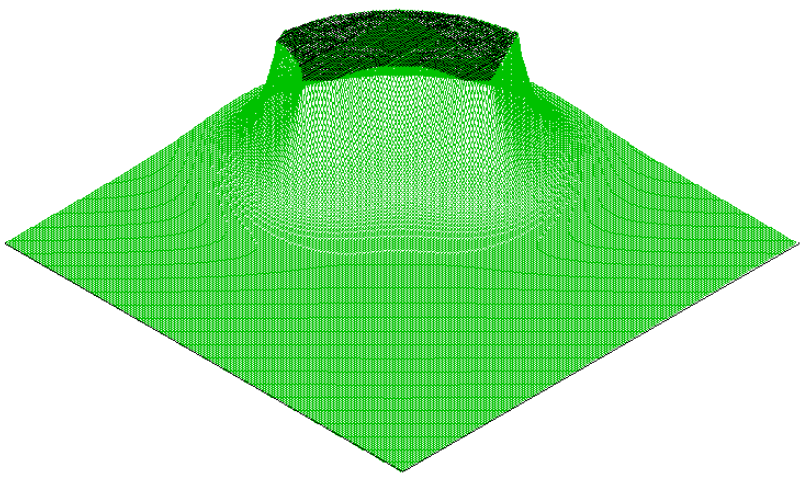

Fig. 4.19 The potential distribution plot along the *x*-*y* plane at a fixed value of *z*. The darkened flat top of the plot represents the region within the uniform magnetic field within between the pole pieces, while the smooth slopes at the sides represent the non-uniform fringe fields.

4.6.4 Calculation of ion trajectories

Ions of mass M_α were created at point S and given an initial energy E. During the flight of the ions through the magnet, the program divides the flight duration into time steps. The size of the time steps depends on the rate of change of magnetic potential gradient at that point in space. The time steps are large at regions with relatively constant gradients and become smaller in regions with large variations in gradients.

At each time step, the program performs linear interpolation between the potential V at the ion's current position with potentials V_1 to V_6 at the 6 adjacent grid points to determine the potentials V'_1 to V'_6 at surrounding *intermediate points* that are *half* a grid unit (g_u) away from the ion's current position. These potentials were then used to determine the component of the magnetic field as well as the acceleration in the x, y and z direction, according to $\boldsymbol{B} = -\nabla \mathrm{V}$:

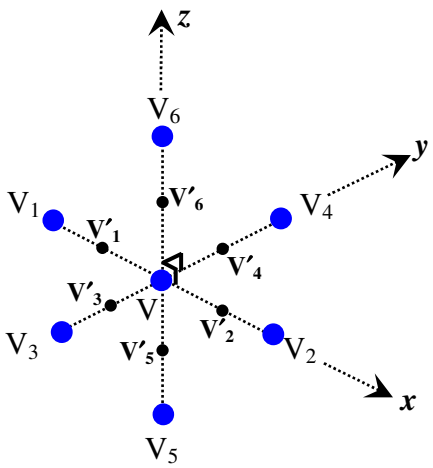

$$V'_i = \frac{V + V_i}{2} \quad , \quad i = 1,2,3,4,5,6$$

$$B_x = \frac{V'_1 - V'_2}{g_u}$$

$$B_y = \frac{V'_3 - V'_4}{g_u}$$

$$B_z = \frac{V'_5 - V'_6}{g_u}$$

Fig. 4.20 Schematic of calculations of ***B*** field components.

The acceleration components were then derived from $\boldsymbol{a} = \dfrac{Q\,\boldsymbol{v}\times\boldsymbol{B}}{M_\alpha}$, which then leads to the components in the velocity change during every time step:

$$a_x = \frac{dv_x}{dt} = \frac{Q\left(v_y B_z - v_z B_y\right)}{M_\alpha}$$

$$a_y = \frac{dv_y}{dt} = \frac{Q\left(v_z B_x - v_x B_z\right)}{M_\alpha}$$

$$a_z = \frac{dv_z}{dt} = \frac{Q\left(v_x B_y - v_y B_x\right)}{M_\alpha}$$

4.6.5 Numerical integration of acceleration components

The integration of the components of $\boldsymbol{a}$ were then performed numerically at every time step using the 4th order Runge-Kutta (RK4) method in order to obtain the velocity v_i at the start of every time step:

$$v_{i,n+1} = v_{i,n} + \frac{h_n}{6}\left(k_1 + 2k_2 + 2k_3 + k_4\right) + O\left(h^5\right)$$

where $v_{i,n}$ = The velocity along the i-direction at the start of the nth time step

where $i \in \{x, y, z\}$

$$k_1 = f\left(t_n,\ i_n\right)$$

$$k_2 = f\left(t_n + \frac{h_n}{2},\ i_n + \frac{h_n}{2}k_1\right)$$

$$k_3 = f\left(t_n + \frac{h_n}{2},\ i_n + \frac{h_n}{2}k_2\right)$$

$$k_4 = f\left(t_n + h_n,\ i_n + h_n k_3\right)$$

i_n = The value of the ordinate i at the start of the nth time step

t_n = The value of time t at the start of the nth time step

h_n is the duration of the nth time step $\Rightarrow t_{n+1} = t_n + h_n$

The RK4 method sequentially estimates the gradient once at the start of the interval, twice at the middle, and once at the end. Every subsequent estimation of the gradient uses a value of v_i calculated from the previous estimated gradient. The final average gradient is a weighted average of these 4 estimated gradients, and this final value was then used to calculate the new value of v_i at the end of the interval. Finally, the trajectory was plotted out once the ion velocity was determined at every time step.

4.6.6 Simulation details

All distance (grid) units used in SIMION are in millimetres. The simulation layout is shown below in Fig. 4.21

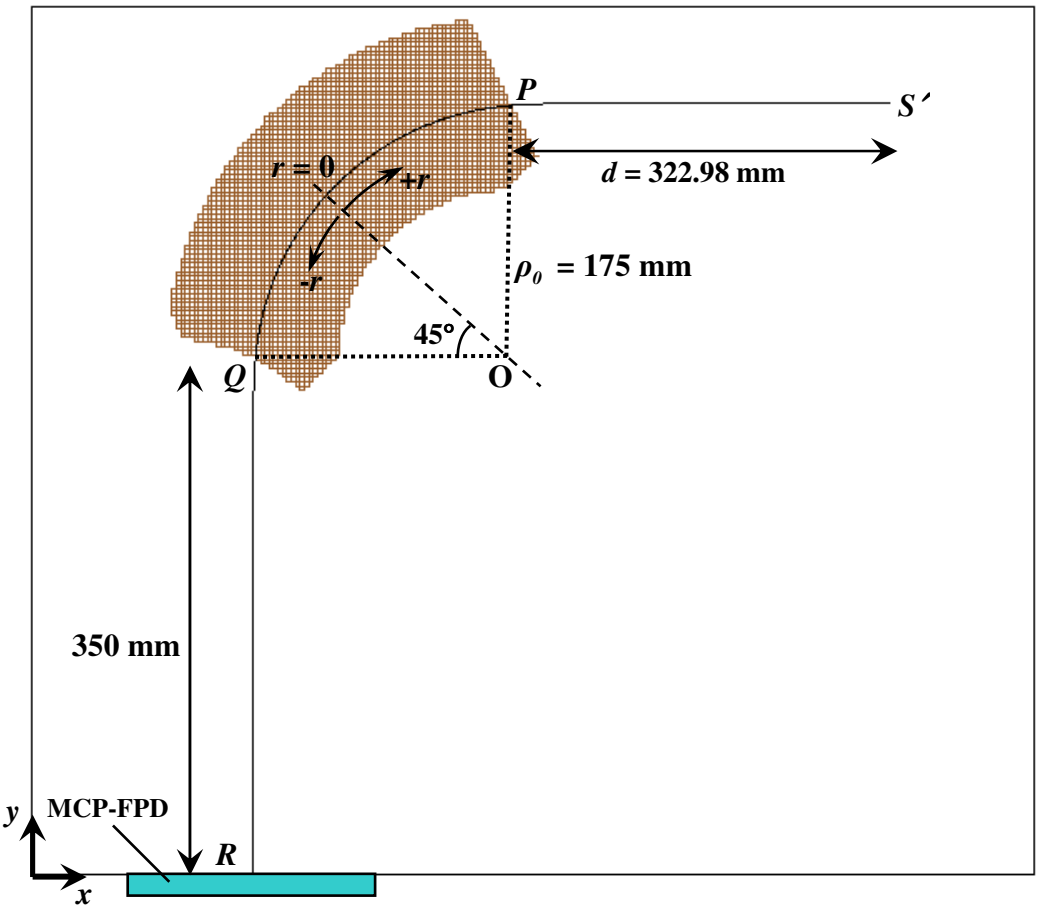

Fig. 4.21 The overview of the workbench in the *x*-*y* plane looking down towards the negative *z*-direction.

Ions were created at a single point source $S'(647.98, 525)$, a distance of d = 322.98 mm from the entry point. This corresponds to a finite backscattered beam size of 1×1 mm on target at 45° tilt. An ion flying along the magnet central trajectory (i.e. with radius $\rho_0 = 175$ mm) will exit at point $Q(150, 350)$, while the MCP-FPD assembly is located along the x-axis with its midpoint at $R(150, 0)$. The variation of the z-component of magnetic flux density B along the central trajectory (r-axis) was calculated and compared to the experimentally measured value.

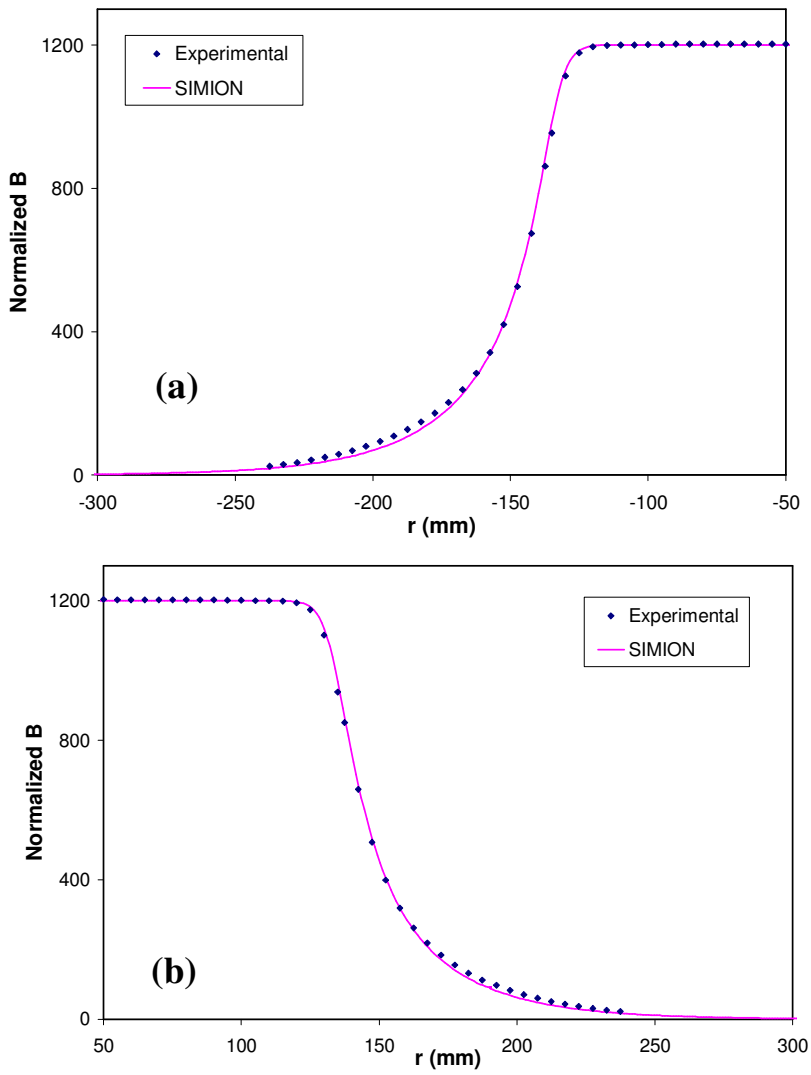

Fig. 4.22 The variation of B along r-axis at the **(a)** exit and **(b)** entrance edge.

Fig. 4.22 (a) and (b) show that SIMION calculated fringe fields exhibit good agreement with experimentally measured values at both exit and entrance edges. This is important as it is the fringe fields that are responsible for the focusing properties of the magnet. The SIMION numerical modeling of the magnetic field is therefore accurate. Ions with different E were then flown through a static $\boldsymbol{B}$ and their corresponding positions of incidence are recorded with respect to the centre of the MCP at R, again using the convention where x is positive to the left of R. The collected data is then compared to the analytical calculations and the experimental data.

4.7 Experimental data using a HRBS calibration run

Investigation of the bending property of the spectrometer magnet requires ion trajectories of different radii of curvature. This was accomplished experimentally by varying the strength of the magnetic field between the poles with ions flying at fixed energy. This is far easier in practice than to vary the energy of the ions, which would involve adjustment of the settings of the accelerator as well as the 90° and switching magnets. A HRBS calibration process was performed [20], where mono-energetic ions of energy E were flown through a magnetic field B whose strength is varied. We define a variable ε to be the square of the ratio of the central magnetic field strength B_0 to B, where B_0 is the field strength that steers the ions to impact onto the midpoint of the MCP. ε was plotted against the position of incidence of the ion along the MCP for different B. This was then compared to the numerical and analytical results.

4.7.1 Calibration experimental details

A beam of 500 keV α^+ particles was incident onto a thin-film target of ~50 Å TaN on thick SiO_2. The beam was collimated so that the incident beam spot on target measures 1×1 mm with the sample tilted at 45° in the IBM geometry (where the target normal, incident and backscattered beams all lie along the same plane). Ions backscattered at 65° scattering angle then pass through the spectrometer magnet and incident onto the MCP-FPD. The magnetic flux density *B* between the poles was varied and a spectrum was measured at every value of *B*, which is measured by a Hall probe placed between the pole pieces.

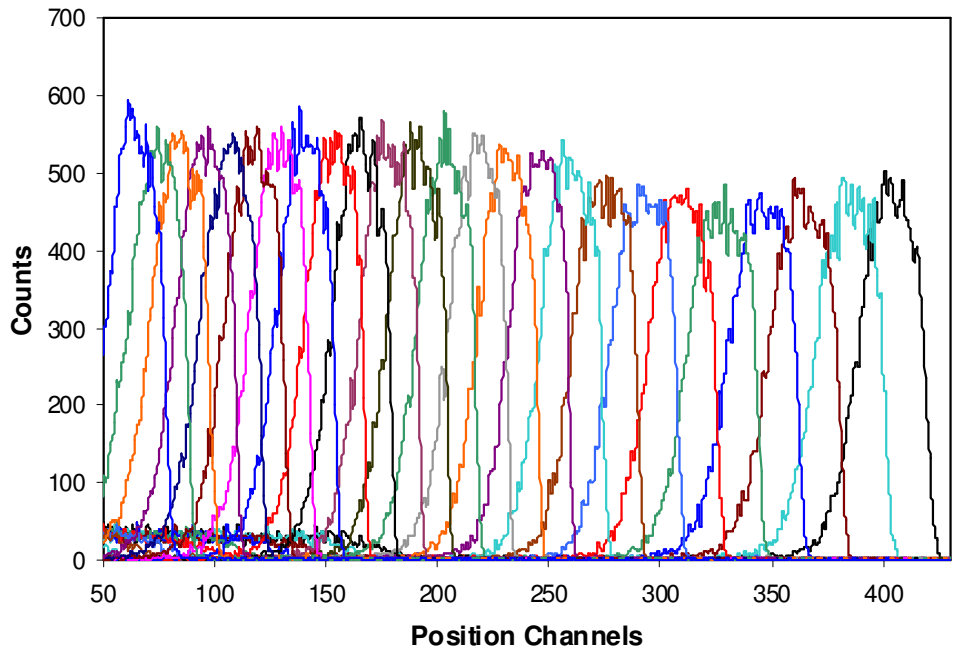

Fig. 4.23 The overlay of all spectra measured at various magnetic flux density during the calibration run. The horizontal axis is the position channels along MCP and channel 0 was set at the midpoint along the length of the MCP. Positive MCP channels correspond to the left of point *M* in both the analytical and numerical studies in the previous sections.

Each spectrum in Fig. 4.23 was measured to an accumulated charge of ~ 4.0 μC on target and *B* was stepwise decreased so that the Ta peak moves across the MCP, which is equivalent to an ion beam of increasing *E* at constant *B*. A typical calibration run consists of 50 spectra, translating to a total incident charge of 200 μC received by

the TaN target during a standard calibration run. Target damage is minimal at the surface as sputtering effects are not significant during the calibration process. The sputtering yields calculated using TRIM-Dynamic (T-Dyn) [44] are ~ 5×10^{-3} for both Ta and N at 45° target tilt fors 500 keV He^{+} ions. A 200 μC incident charge on a beam spot area 1 mm × 1 mm, equivalent to a fluence of ~ 1.25×10^{17} ions/cm^2, is expected to sputter off a negligible linear thickness of ~ 1 Å of TaN (density 16.3 g/cm^3).

The surface edge of the Ta peak corresponds to a specific backscattered ion energy E, since the kinematic factor k is a function of only the scattering angle, which is fixed throughout the calibration process. The position of the peak surface edge at every value of B will therefore indicate the position of incidence of ions with a fixed energy E along the MCP. A linear variation in B causes the same change in the ion trajectory radius as a variation in E according to $E^{-0.5}$. We define a variable ε as:

$$\varepsilon = \frac{E}{E_0} = \left(\frac{B_0}{B}\right)^2$$

where E_0 is the energy of an ion travelling along the central trajectory through flux density of B_0 and subsequently incidents onto the midpoint along the MCP. For every spectrum measured, the position of each surface edge was obtained by fitting it with error functions using Mathematica, and ε was calculated using the measured value of B. A graph of surface edge position vs ε was plotted and compared to the numerical and analytical calculated data using Mathematica and SIMION in the previous sections.

4.8 Direct, Matrix, Numerical calculations and Experimental data

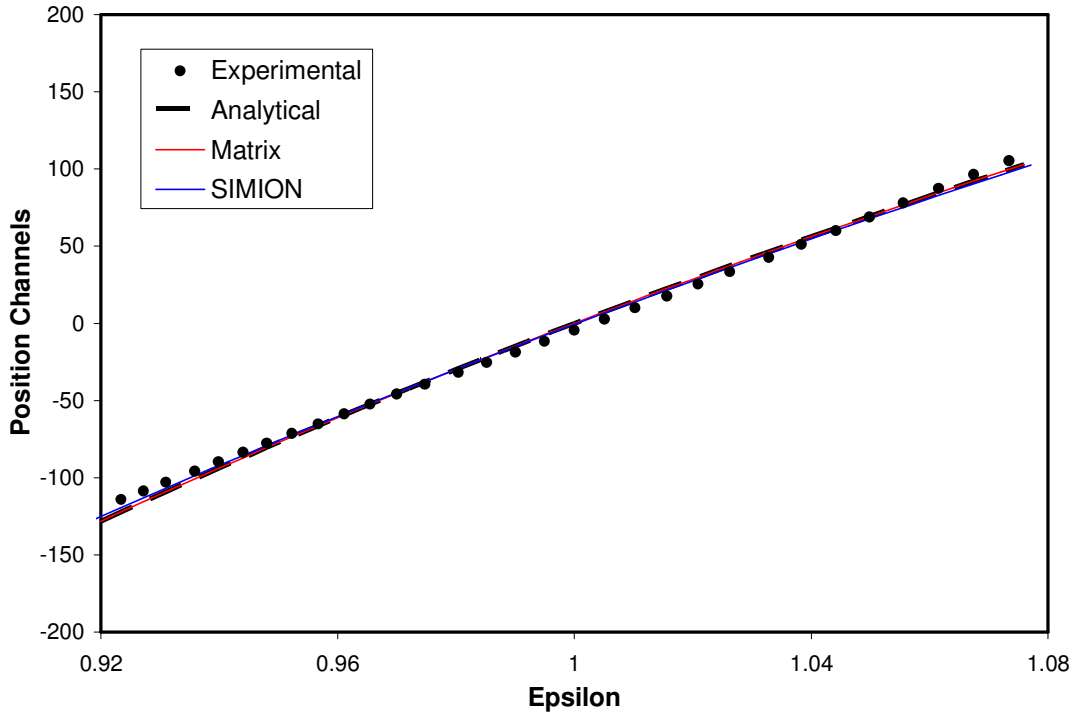

Fig. 4.24 The plot of position of ion incidence vs ε. The experimental data was compared to the SIMION and the analytical calculations.

The results in Fig. 4.24 show that the actual bending property of the magnet (experimental) is close to that predicted by the Numerical and analytical (Direct and Matrix) calculations. Numerical calculations show slightly better agreement to the experimental than the analytical calculations, due to more accurate modeling of the fringe field. Deviations are insignificant for $\varepsilon \in [0.95, 1.05]$, while deviations outside this range remain small.

4.9 Conclusion

In conclusion, the bending property of the magnet has been modeled using analytical and numerical calculations. The actual property show good agreement with the calculations, and we can conclude that the spectrometer works as expected.

Chapter 5

Spectrum processing and MCP Gain correction

5.1 Introduction

The HRBS calibration data allows for the conversion of measured "raw" position spectra to energy spectra. In this chapter, this conversion process is described in detail, followed by the development of a novel MCP gain correction process which makes use of a reverse conversion from energy to position spectra.

5.2 Consistency of HRBS Calibration process

The correlation between ε and position x is characteristic to the HRBS detection system, different calibration runs should yield the same correlation. Data collected from calibration runs performed on different days is plotted in Fig. 5.1(a). All data sets were measured with 500 keV He^+ incident beams at 65° scattering angle. A thick Au target was used on August 2008 while 50 Å TaN thin film targets were used for

the other two sets. The data show good agreement with each other, the data points forming almost the same ε-x relation. Fig. 5.1(b) shows the residual plot of the data points in Fig. 5.1(a) relative to a first order fit. A systematic non-linearity of within 0.15 % with a well defined shape is clearly reproduced among data from all runs, this is the characteristic spectrometer non-linearity. The calibration process is therefore highly reproducible, and the correlation between ε and x is consistent and well defined.

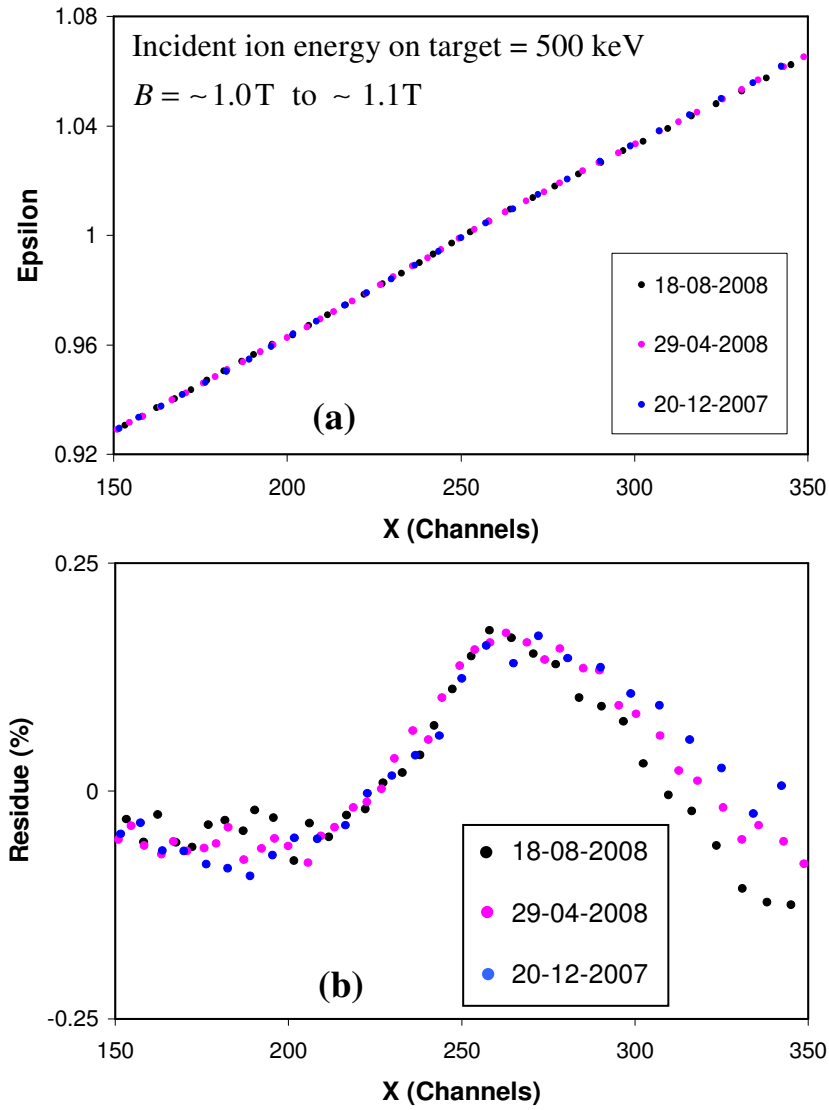

Fig. 5.1 **(a)** Plot of different sets of calibration data measured at approximately 4 months interval. **(b)** Plot of the residuals of data from all the sets relative to a single linear fit.

Using the data from the calibration run described in 4.5.1 in chapter 4, we re-plot the data as x vs ε (so as to facilitate the forward-binning process later in this chapter) in

Fig. 5.2(a) with a 6th order polynomial fit function $C_f(\varepsilon)$ in red. Fig. 5.2(b) and 5.2(c) show the residual plot and the normalized gradient $C'_f(\varepsilon)$ plot at fixed intervals of epsilon representing the equal 512 energy channels respectively.

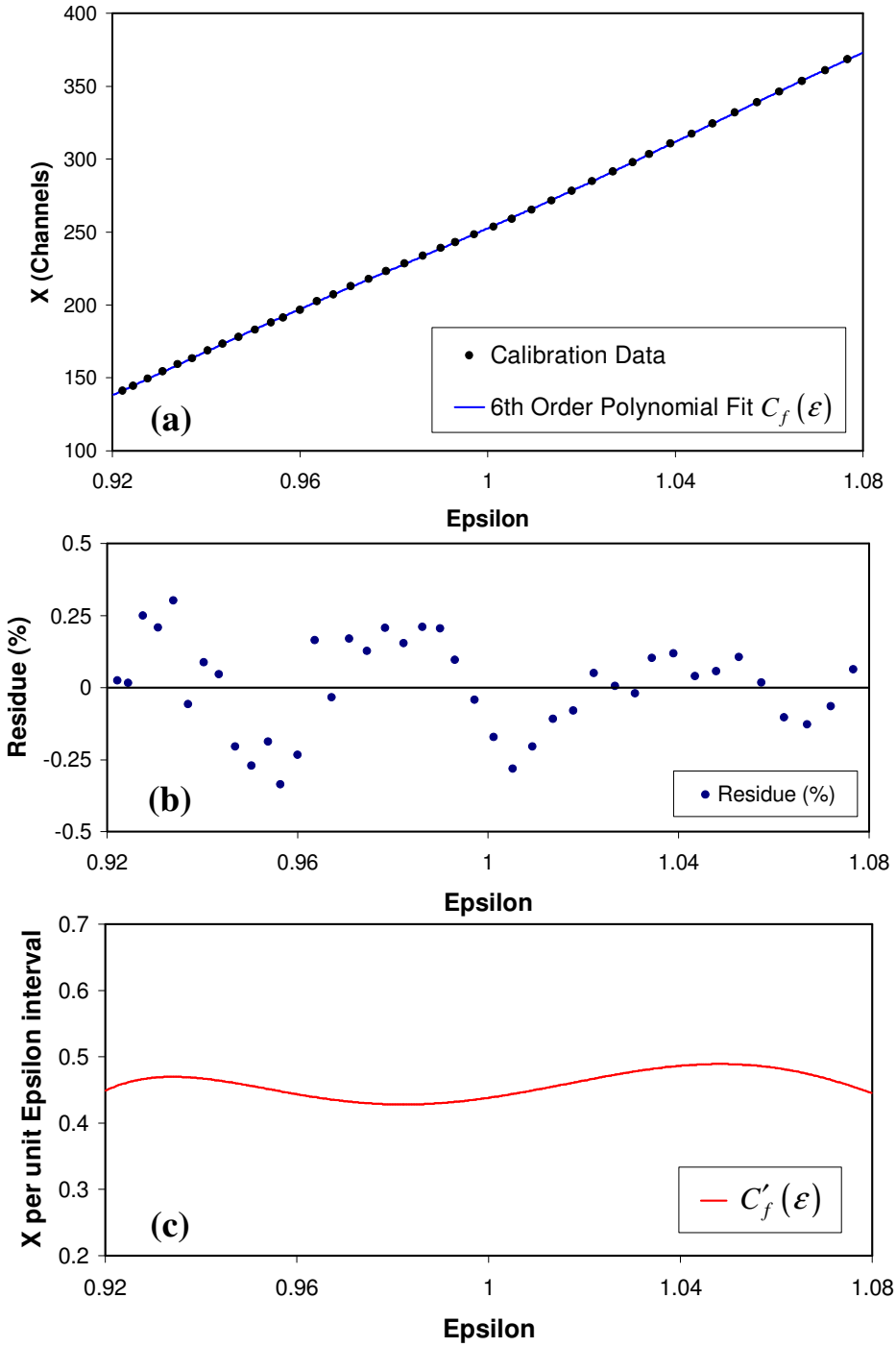

Fig. 5.2 **(a)** Plot of HRBS calibration data (surface edge position) along MCP vs ε with a smooth 6th order polynomial $C_f(\varepsilon)$ fit with the residuals plotted in **(b)**. The normalized gradient $C'_f(\varepsilon)$ vs ε is plotted in **(c)**.

Fig. 5.2(b) shows that the residues from the 6th order fit still show secondary structures, which can be eliminated with a higher-order polynomial fit. These residual structures are not well-understood yet. A 6th order fit is chosen as it takes into account the general trend of gradient variation while ignoring these minute residual structures.

The gradient $C'_f = \frac{dx}{d\varepsilon} = E_0 \frac{dx}{dE}$ of the polynomial fit represents the number of position channels corresponding to equal intervals of epsilon, and it is shown to vary with epsilon (energy) in Fig. 5.2(c). This gradient variation is used to "re-bin" counts in the position spectrum $F(x)$ into energy spectrum $f(E)$ using the relation $f(E) = \left.\frac{dx}{d\varepsilon}\right|_{\varepsilon_i} F(x)$.

5.3 Conversion of position spectra into energy spectra (FORBIN)

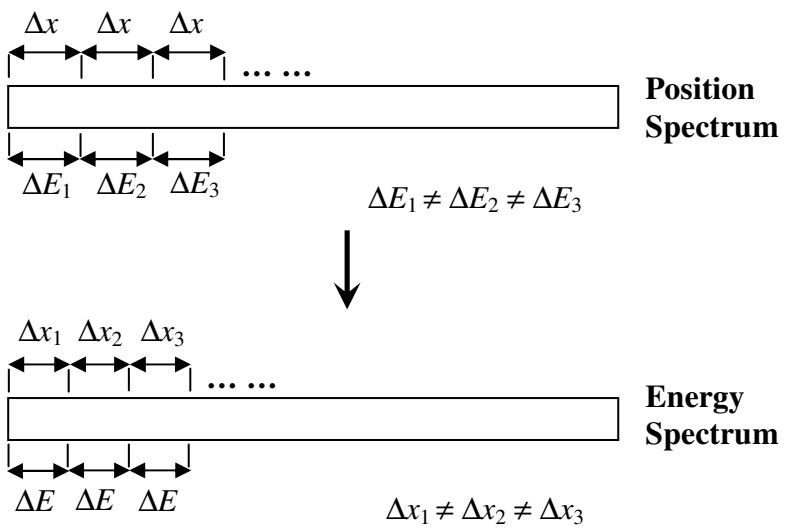

Fig. 5.3 Conversion of position to energy spectrum.

Different energy values ΔE_i are assigned to different regular intervals of position Δx in the position spectrum, as shown in Fig. 5.3. Conversion into an energy spectrum requires knowledge of the correlation between the absolute values of E and x (directly expressed in the calibration data plot), as well as the relationship between their intervals ΔE and Δx (given by the gradient variation). This is usually performed with software packages that were provided as part of a bundle with the HRBS endstation from Kobe Steel Ltd. Here we describe steps of the conversion in detail, and a Mathematica program "FORBIN" was written for this process. This is to ensure that the bundled conversion software works as expected from theory, as well as provide a foundation for the reverse conversion process (energy to position spectrum) needed for the MCP gain correction in the later part of this chapter.

5.3.1 Energy spectrum from multiple windows of position spectra

The energy range that can be extracted from a position spectrum window is limited, due to the nature of the spectrometer ion optics. The maximum reliable range of ε for each window is typically $[0.90, 1.10]$, which translates to an energy range of ~ 100 keV for incident beam energy of 500 keV. This is insufficient for a complete HRBS energy spectrum with a typical range of up to 250 keV that is required if peaks from both heavy and light elements are to be included. Therefore, up to 3 windows are usually taken at different spectrometer field strength for every sample, each window contributing different energy ranges which are subsequently combined into one single energy spectrum.

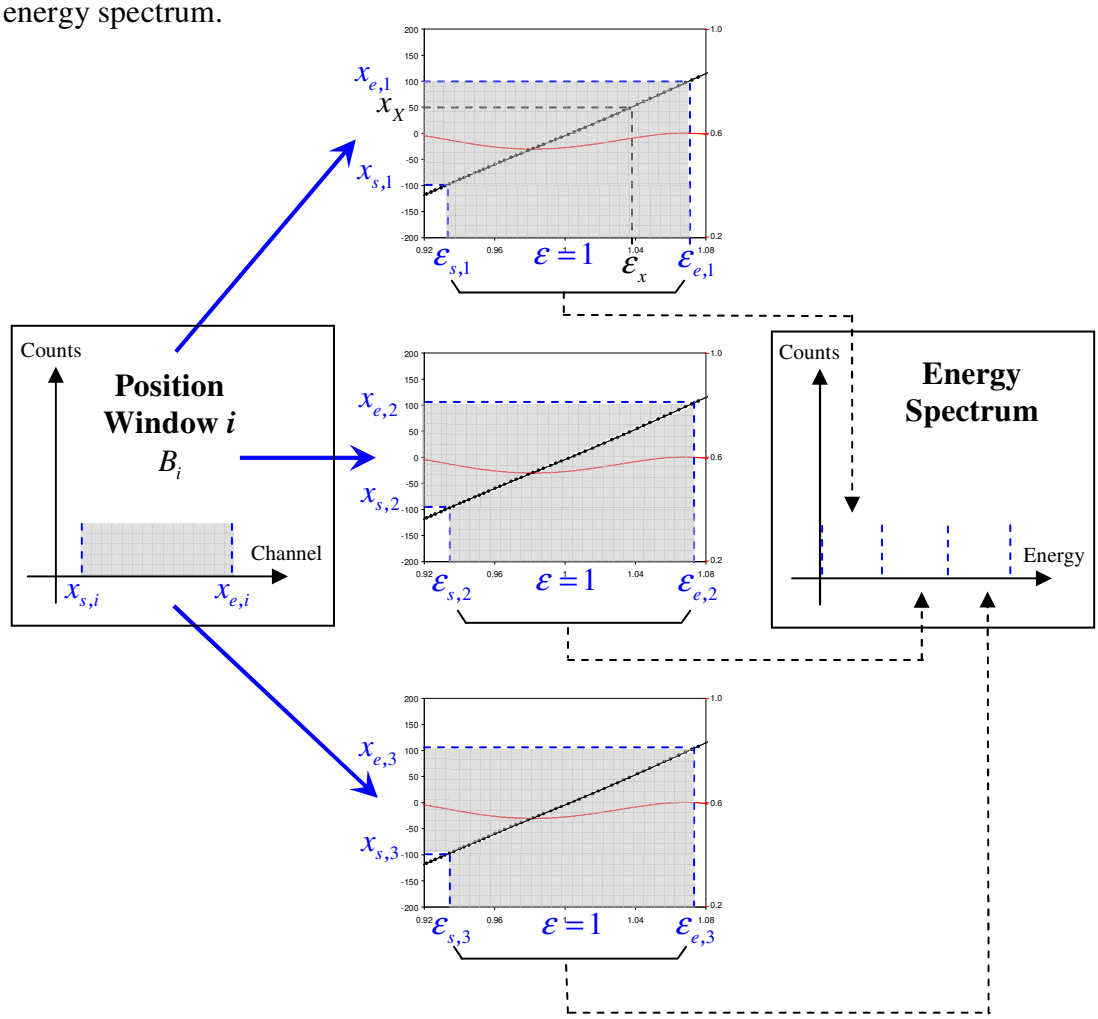

Fig. 5.4 Schematic of the process of combining several position windows into a single energy spectrum.

Let us assume that 3 windows of position spectra were measured (Fig. 5.4) at spectrometer field strengths B_i, $i = 1, 2, 3$. The same calibration curve applies to each of these windows, with the centre ($\varepsilon = 1$) of each curve corresponding to a backscattered ion travelling along the same central trajectory within the spectrometer magnet. This results in the relation $E_{0,i} \propto B_i^2$ where $E_{0,i}$ is the ion energy at the centre ($\varepsilon = 1$) of window *i*, which allows for the calculation of the energy at the centre of each window relative to that at the centre of all the other windows.

The absolute values of $E_{0,i}$ can be determined if at least one window contains the surface edge of an RBS signal from an element that exists on the surface of the target. Let window 1 contain a surface edge of an element *X* at channel x_X with a backscattered ion energy E_X . From the definition of ε , we express $\varepsilon_X = \frac{E_X}{E_{0,1}} = \frac{k_X E_{\text{incident}}}{E_{0,1}}$, where k_X is the kinematic factor of element *X* and E_{incident} is the incident beam energy on the target, both of which are known from experimental conditions. The value of ε_X is then obtained from the calibration curve as the epsilon corresponding to the position channel *X*. Therefore, $E_{0,1} = \frac{E_X}{\varepsilon_X}$ and hence

$$E_{0,2} = \left(\frac{B_2}{B_1}\right)^2 E_{0,1} \quad \text{and} \quad E_{0,3} = \left(\frac{B_3}{B_1}\right)^2 E_{0,1}$$

These values of $E_{0,i}$ are then used to determine the energy values *E* for all ε in each window *i* using the relation $E = \varepsilon E_0$.

5.3.2 Generating the required lists

Next, we choose regions $\left[x_{s,i}, x_{e,i}\right]$ containing $n_{x,i}$ position channels in every window i from which we piece out the final energy spectrum, where $x, n \in \mathbb{Z}^+$. Each channel x constitutes an interval along the x-axis which is bounded by half-integral values $x \pm \frac{1}{2}$. The set of bounds for each chosen region is therefore $\left\{x_{s,i} - \frac{1}{2}, x_{e,i} + \frac{1}{2}\right\}$, which corresponds to epsilon and energy bounds $\left\{\varepsilon_{s,i}^b, \varepsilon_{e,i}^b\right\}$ and $\left\{E_{s,i}^b, E_{e,i}^b\right\}$ respectively from their calibration data (Fig. 5.5).

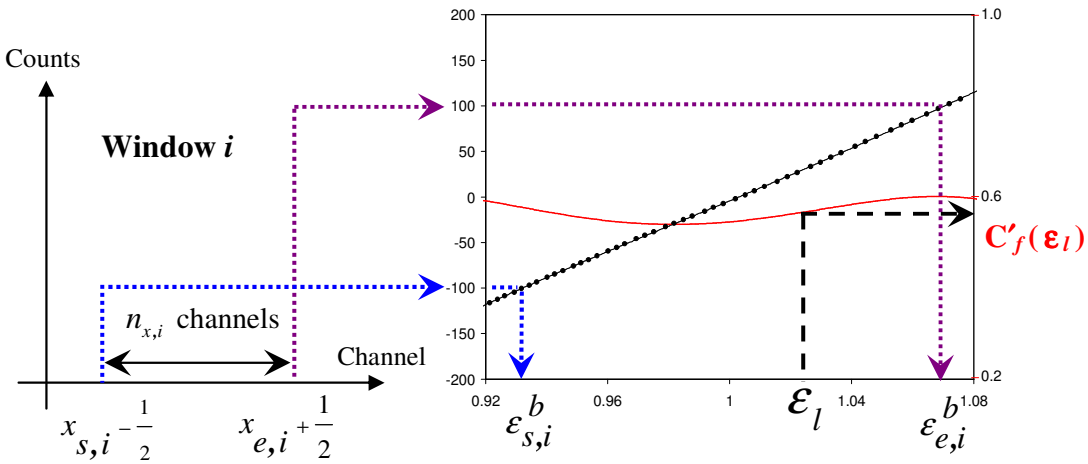

Fig. 5.5 Schematic of the position bounds and the corresponding epsilon bounds.

The bounds for the full energy range in the combined energy spectrum are $\left\{E_{s,1}^b, E_{e,3}^b\right\}$, which is divided into 512 equal intervals with a total of 513 bounds $\left\{E_1^b = E_{s,1}^b, E_2^b, E_3^b, \ldots, E_{513}^b = E_{e,3}^b\right\}$. The energy at the midpoint of these intervals are $\left\{E_1, E_2, E_3, \ldots, E_{512}\right\}$, which are assigned to be the energy of the channels in the combined spectrum.

The number of energy channels allocated to each position region is then determined by the positions of their boundary energies $E_{e,1}^{b} = E_{s,2}^{b}$ and $E_{e,2}^{b} = E_{s,3}^{b}$ in the list $\left\{E_j^b\right\}$ where $j = 1, 2, ..., 513$. Let $n_{E,i}$ be the number of energy channels allocated to each position interval $\left[x_{s,i}, x_{e,i}\right]$, so that $n_{E,1} + n_{E,2} + n_{E,3} = 512$. The epsilon bounds $\left\{\varepsilon_{s,i}^{b}, \varepsilon_{e,i}^{b}\right\}$ for each window *i* are then divided into $n_{E,i}$ intervals, with their midpoint values $\left\{\varepsilon_1, \varepsilon_2, ..., \varepsilon_{n_{E,i}}\right\}$ representing the values of ε of the energy channels in that region. The number of position channels that correspond to each energy channel $\left.\frac{dx}{d\varepsilon}\right|_{\varepsilon_l}$ is then obtained using the gradient of the calibration curve at every ε_l, where $l = 1, 2, ..., n_{E,i}$. These values are subsequently normalized so that

$$\sum_{l=1}^{n_{E,i}} \left.\frac{dx}{d\varepsilon}\right|_{\varepsilon_l} = n_{x,i} \quad \text{for} \quad i = 1, 2, 3.$$

Finally, we generate a list of cumulative position channel numbers $\left\{x_j^e\right\}$ for each region according to the distribution in the list $\left\{\left.\frac{dx}{d\varepsilon}\right|_{\varepsilon_l}\right\}$, so that:

$$x_1^e = \frac{1}{2} \quad \text{and} \quad x_{l+1}^e = x_l^e + \left.\frac{dx}{d\varepsilon}\right|_{\varepsilon_l} \quad , \quad l = 1, 2, ..., n_{E,i}$$

These lists form the boundaries, in terms of position channels, of the energy channels in each window *i*. They have the same starting and ending point as the half-integral boundaries of the real position channels in the position spectrum.

5.3.3 Re-binning process

Schematically, all position and energy channel bounds are plotted along the x line:

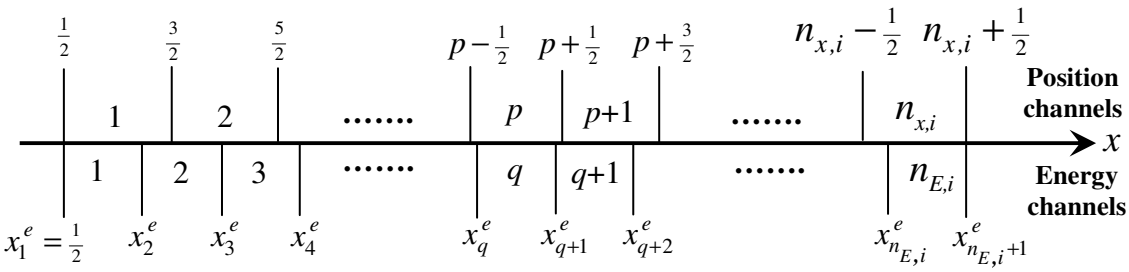

Fig. 5.6 Schematic of the re-binning process

Both position and energy channels are numbered with integers, with a common starting boundary of $\frac{1}{2}$ as the left bound of the first position and energy channel in the region. The right bound of the final energy channel $x_{n_{E,i}+1}^e$ also coincides with the final position channel bound $n_{x,i}+\frac{1}{2}$. Let $F(x)$ be the counts at channel x in the position spectrum, and $f(e)$ be the counts allocated to channel e in the energy spectrum. Since $n_{E,i} > n_{x,i}$ in general, $\left.\frac{dx}{d\varepsilon}\right|_{\varepsilon_j} < 1$, and each energy channel is sequentially formed from the position channels according to the cases:

(i) As in the case of $e = q$, where the entire energy channel correspond to part of a single position channel $x = p$ for some $p, q \in \mathbb{Z}^+$,

$$\Rightarrow \quad f(q) = \left(x_{q+1}^e - x_q^e\right) F(p)$$

(ii) As in the case of $e = q+1$, where the energy channel straddles regions in two consecutive position channels p and $p+1$.

$$\Rightarrow \quad f(q+1) = \left[\left(p+\frac{1}{2}\right) - x_{q+1}^e\right] F(p) + \left[x_{q+2}^e - \left(p+\frac{1}{2}\right)\right] F(p+1)$$

The energy spectrum fragments are formed once all energy channels are formed using the above process, and the re-binning process is complete.

5.3.4 Fragment scaling

Due to variations in experimental conditions, the position windows may be collected to slightly different incident integrated charge on the target. In such cases the energy spectrum fragments need to be scaled to the same integrated charge. As such, the average counts of *n* channels on each side of each of the 2 boundaries between the fragments are calculated and a linear scale factor is obtained. It is necessary to calculate the scale factor over a number of channels so as to minimize the statistical variation in the counts, but *n* must be kept small so as to ensure that this process do not affect the gradient of the final spectrum. The boundaries must therefore be chosen at regions without any abrupt change in gradient such as edges of elemental signals. At each boundary, the count in every channel in the fragment on the left (or right) is then scaled so that the average count is the same on each side of that boundary. Finally, these scaled spectrum fragments are then put together to form the full energy spectrum.

5.4 Spectrum conversion using software programs

In practice, the entire process of obtaining the spectrum is performed using software programs provided by Kobelco along with the HRBS endstation hardware. The calibration curve-fitting is performed by a program “CalibrateChB2”, while the re-binning of position spectra is done by the program “CompoundSP”. CalibrateChB2 user interface is shown in Fig. 5.7, which is divided into panels (a) – (d).

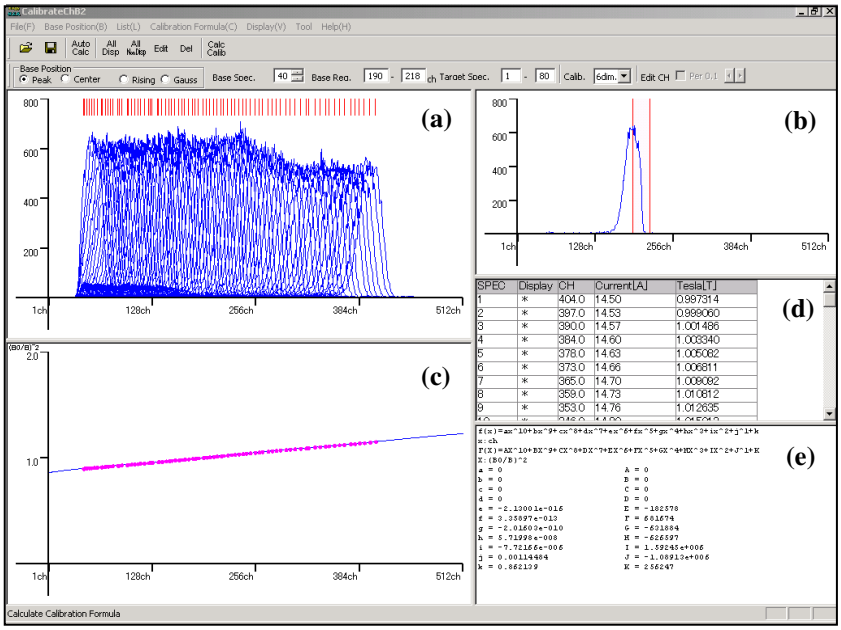

Fig. 5.7 CalibrateChB2 program user interface which consists of panels (a) – (d). The program allows for different calibration fit conditions and the graphical fit of the ε-x points is plotted out in (c) while the conditions are varied so as to allow for the identification of the best fit conditions.

The program reads in the raw calibration data file and plots the overlay of calibration peaks across the MCP in panel (a). The user defines the fit parameters in (b), which the program uses for the error function fit of each peak to determine the peak surface edge position. The ε for each peak is calculated using the measured magnetic field of the spectrometer magnet, after which the position-ε points are plotted in (c). The program allows for removal of unwanted data points by the user in (d), the remaining points are then fitted by a polynomial of up to the 10th order, and the coefficients of the fit are displayed in (e). Once the calibration fit is completed, CalibrateChB2 outputs a calibration text file which contains the calibration fit parameters as well as a list of 512 correction factors which the user can add in to correct for the non-linear MCP gain along its length.

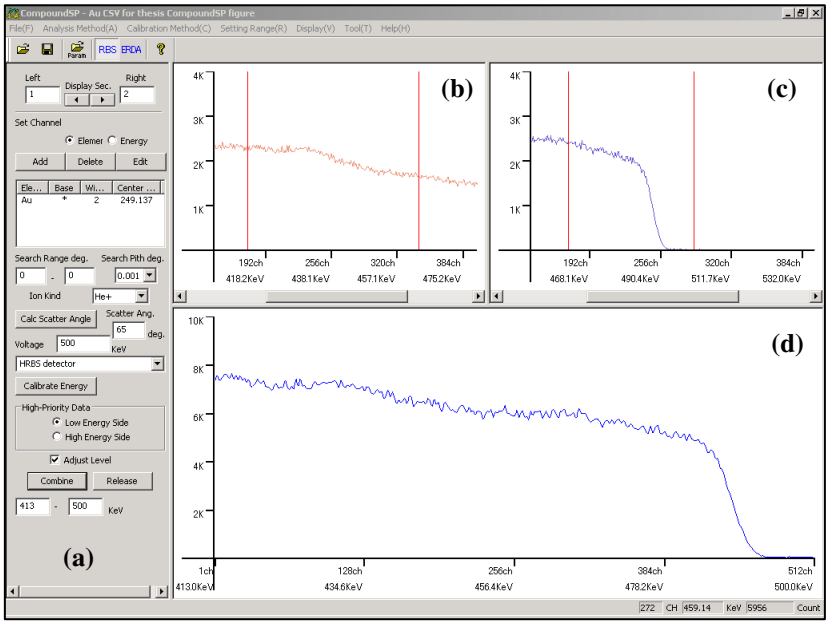

Fig. 5.8 User interface of CompoundSP. The experimental and re-binning conditions are entered in the side panel (a), the position windows and their respective chosen regions are displayed in (b) – (c) and the final combined energy spectrum is displayed in (d).

Next, the program CompoundSP (Fig. 5.8) is used to perform the re-binning and the combining of the position spectrum windows. Once the scattering angle, incident beam energy as well as an elemental surface edge position in one of the windows are defined, the program automatically uses the fit parameters in the calibration text file to assign absolute energy values to every ε of every window. Regions in different windows are then chosen to be combined into the final energy spectrum. In cases where the energy spectrum fragments scaling are required, the program includes an "Adjust level" function, where the fragments are scaled with the user defining the precedence that given to either the higher or lower energy side of every boundary. Once the final spectrum is formed, the program then outputs the spectrum in comma-separated values (.csv) format where it can be easily be changed to the required import format of RBS simulation programs like RUMP and SIMNRA.

5.5 Comparison of results from FORBIN and CompoundSP

The software programs allow for the energy spectra to be easily and efficiently obtained. However, it is necessary to check that the programs function as expected to ensure that the energy spectrum obtained is correct. This check is also essential to formulation of the reverse-binning process required in the next section. The Mathematica code FORBIN was written to duplicate the calibration, combining, re-binning and fragment scaling processes of two position windows into a single energy spectrum. The final output from FORBIN was then compared to that obtained using CompoundSP in Fig. 5.9. An almost perfect agreement is shown, allowing us to conclude that the software correctly performs calibration as well as the spectrum conversion.

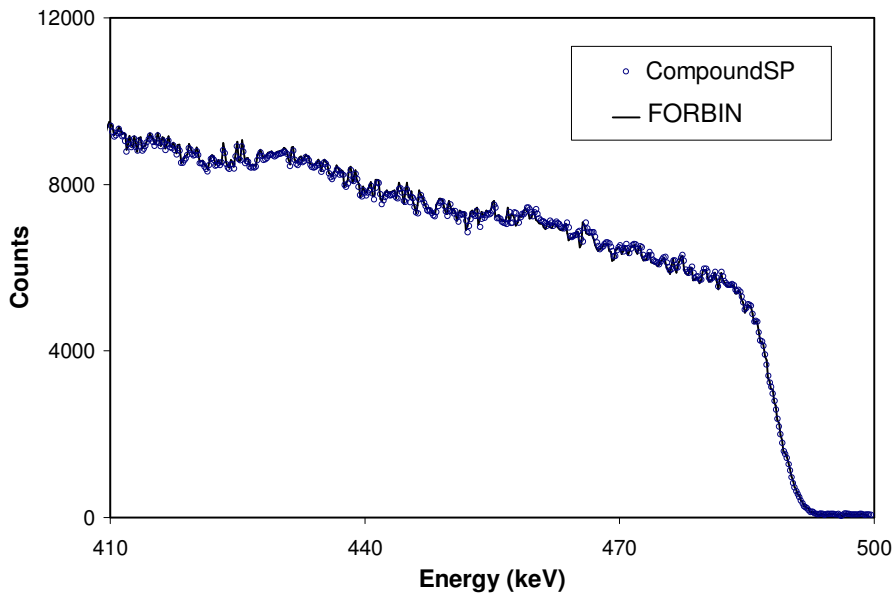

Fig. 5.9 Comparison between energy spectrum obtained using FORBIN and CompoundSP from regions in two separate position windows.

5.6 MCP Gain correction

The MCP provides amplification of the electrical signal from each incident backscattered ion using an electron multiplication process. Though every electron cascade event is expected to reach saturation in theory, the amplification gain of the MCP is observed to vary across its length. This may be due to a difference in the electron emission probabilities along the MCP or non-uniformities in the E field distribution. This would result in different efficiencies along different parts of the MCP. The variation in the size of the gap between the top and bottom plates of the MCP, as well as between the MCP and the FPD also contribute to the variation of the MCP gain along its length. This systematic variation is an artifact characteristic to the detection system, and may give rise to false signals and structures in the final HRBS spectrum obtained. Procedures to correct for this were developed as part of the work done for this thesis, and are presented in the following sections.

5.6.1 Reverse-binning process (REVBIN)

The normal procedure during spectrum processing is to convert a position spectrum into an energy spectrum. However, in order to correct for the characteristic variation in gain with position along the MCP, a theoretical response from an ideal MCP with uniform gain along its length is needed for comparison. The theoretical framework of RBS is built upon the energy distribution of backscattered ions and therefore theoretical simulations of ideal behaviour will be in form of energy spectra. It is therefore necessary to convert the theoretical ideal energy distribution into its equivalent (ideal) position distribution. It is then compared to the actual response of the detection system to correct for any deviation from the ideal behaviour. Here we

describe this reverse-binning process in detail using notations from section 5.3, and a Mathematica code "REVBIN" has been written for this process.

It is sufficient to consider the case of "reverse-binning" from a single window of energy spectrum back into its position equivalent. We first define the range of n_x channels $x \in [x_s, x_e]$ within the position spectrum that is to be corrected for, with $n_x, x_s, x_e \in \mathbb{Z}^+$. This translates to half-integral outer position bounds of $\left\{x_s - \frac{1}{2}, x_e + \frac{1}{2}\right\}$ and the corresponding epsilon and energy bounds $\{\varepsilon_s^b, \varepsilon_e^b\}$ and $\{E_s^b, E_e^b\}$ respectively from the inverse calibration fit function $C_R(x) = C_f^{-1}(x)$ such that $\varepsilon_s^b = C_R\left(x_s - \frac{1}{2}\right)$ and $\varepsilon_e^b = C_R\left(x_e + \frac{1}{2}\right)$. The epsilon bounds are unique to every chosen position region, but not the energy bounds as the energy at the centre of the window E_0 varies with the spectrometer field strength *B*. Here we shall work with the epsilon channels and bounds only, the correlation between energy and epsilon can be obtained for different experimental settings using the procedure as described in section 5.3.1.

During the FORBIN process, the position region $[x_s, x_e]$ containing the channel numbers $\{x_1, x_2, ..., x_{n_x}\}$ is re-binned into 512 equal channels of energy (epsilon). Our task here is therefore to convert a single spectrum of 512 epsilon channels back into n_x position channels in the region of $[x_s, x_e]$ in its corresponding position spectrum. We start with 512 equal intervals in the epsilon region $\left[\varepsilon_s^b, \varepsilon_e^b\right]$, with a set

of 513 bounds $\left\{\varepsilon_s^b = \varepsilon_1^b, \varepsilon_2^b, \varepsilon_3^b, \ldots, \varepsilon_{513}^b = \varepsilon_e^b\right\}$. The normalized inverse gradient $C_R'(x_i) = \left.\frac{d\varepsilon}{dx}\right|_{x_i}$ (right ordinate axis of Fig. 5.10) is calculated at every position channel number $x_i \in \left\{x_1, x_2, \ldots, x_{n_x}\right\}$ and normalized so that $\sum_{i=1}^{n_x} \left.\frac{d\varepsilon}{dx}\right|_{x_i} = \varepsilon_e^{\,b} - \varepsilon_s^{\,b}$.

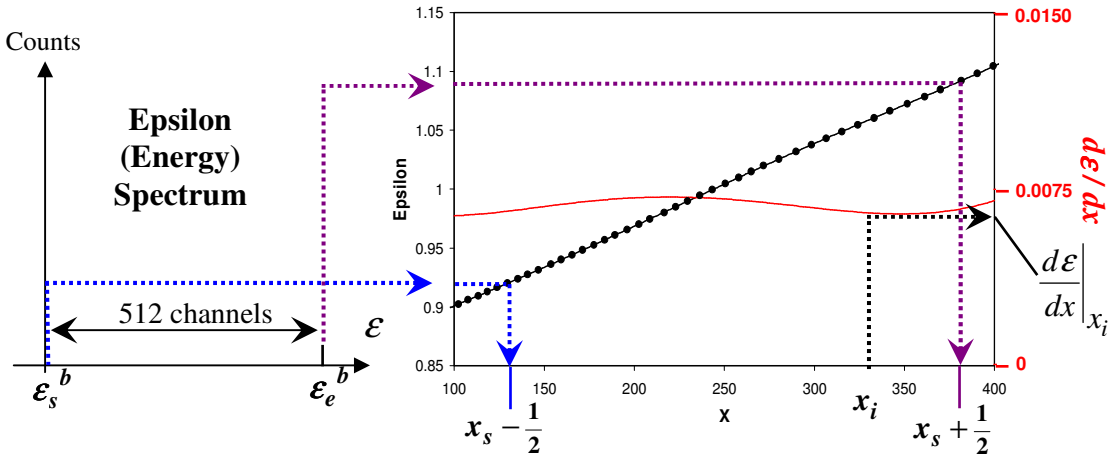

Fig. 5.10 Schematic of the epsilon bounds and the corresponding position bounds.

Each of the n_x normalized gradients $\left.\frac{d\varepsilon}{dx}\right|_{x_i}$ represents the unequal size of the epsilon interval corresponding to every equal position channel which we wish to obtain. From these we construct a list of epsilon values $\left\{\varepsilon_i^{\,x}\right\}, i = 1, 2, \ldots, n_x + 1$ which form the bounds of each of these epsilon intervals. The equal epsilon channels of the epsilon spectrum (which we began with) and the unequal epsilon intervals of the required position channels are shown in Fig 5.11:

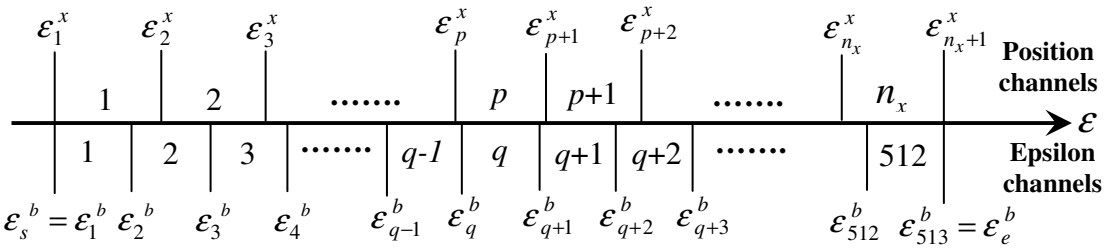

Fig. 5.11 Schematic of the REVBIN process.

Let $f(e)$ be the counts in channel e in the epsilon spectrum and $F(x)$ be the counts to be allocated to channel x in the position spectrum (Fig. 5.11). Since $n_x < 512$, each position channel x is sequentially formed from the epsilon channels, in a manner similar to the forward-binning process, according to the following cases:

(i) As in the case of $x = p$, where position channel contains an entire epsilon channel $e = q$ ($p, q \in \mathbb{Z}^+$) and corresponds to two more on each side,

$$\Rightarrow \quad F(p) = \frac{\varepsilon_q^b - \varepsilon_p^x}{\varepsilon^e} f(q-1) + f(q) + \frac{\varepsilon_{p+1}^x - \varepsilon_{q+1}^b}{\varepsilon^e} f(q+1)$$

(ii) As in the case of $x = p+1$, where the position channel straddles regions in only two consecutive epsilon channels $q+1$ and $q+2$,

$$\Rightarrow \quad F(p+1) = \frac{\varepsilon_{q+2}^b - \varepsilon_{p+1}^x}{\varepsilon^e} f(q+1) + \frac{\varepsilon_{p+2}^x - \varepsilon_{q+2}^b}{\varepsilon^e} f(q+2)$$

where $\varepsilon^e = \varepsilon_{j+1}^b - \varepsilon_j^b$, $j = 1, 2, ..., 512$ is the size of the equal epsilon intervals representing the channels in the epsilon spectrum.

5.6.2 Installation of electrostatic plates

Work has been done by C. S. Ho [45] recently to install a pair of electrostatic plates between the spectrometer magnet and the MCP chamber, as shown in Fig. 5.12.

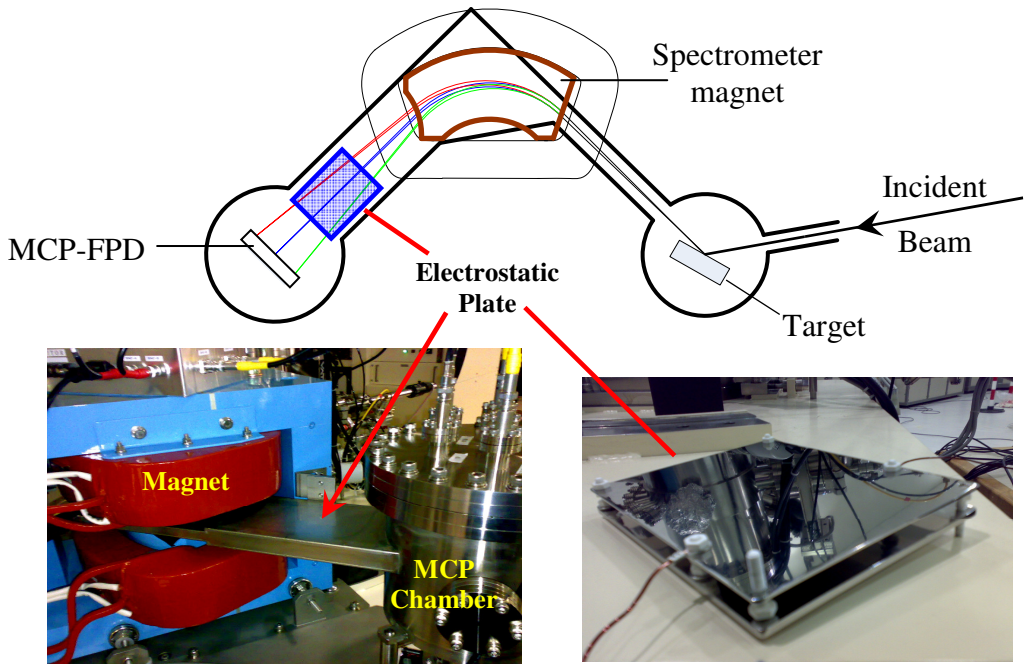

Fig. 5.12 Schematic and layout of the installation of the electrostatic plates

The plates were carefully adjusted to be horizontal, so that all ions are deflected only in the vertical direction and the $x-\varepsilon$ characteristics of the detection system remains unaffected. The electrostatic field serves to eliminate low-energy stray ions that have scattered off the collimator, floor, walls or ceiling of the conduit along any part of the ion trajectory between the target and the MCP. The paths of these stray ions may be systematic or random, depending on how they are generated. Fig 5.13 illustrates the vertical plane of the electrostatic plate layout in relation to the MCP. The trajectories of ions with different backscattered energies were calculated at a fixed electrostatic potential difference of ~ 1kV.

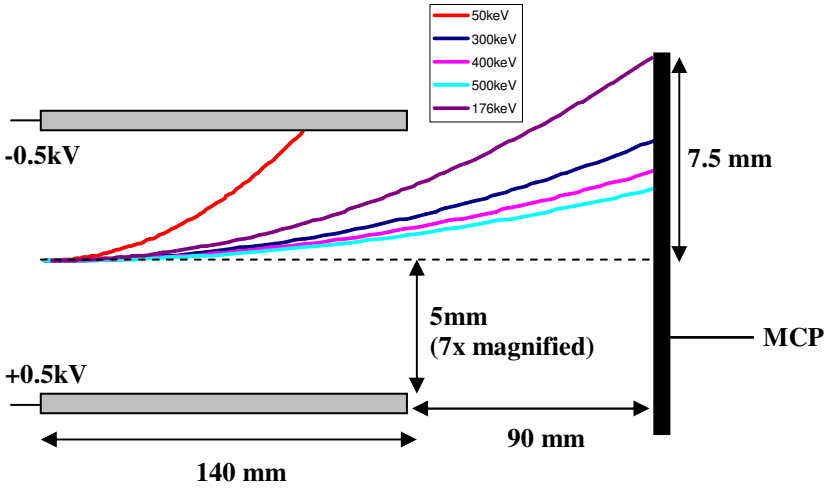

Fig. 5.13 Scaled diagram of the layout of the electrostatic plates relative to the MCP, as well as the calculated ion trajectories between the plates at different ion energies at a potential difference of 1 kV. Source : [45]

The random strays are mainly created by scattering events off the collimator or walls within the magnet and in the MCP chamber. They may hit anywhere along the MCP, contributing to “noise” in the spectra obtained. The systematic strays may be due to part of the main energy-analyzed ion beam hitting a particular section of the vacuum conduit as it exits the spectrometer magnet, scattering off once to directly hit the MCP. Since the beam profile through the magnet remains the same regardless of the spectrometer field strength, the beam will always hit that particular section in the same manner, scattering off in certain preferential directions towards the MCP and causing systematic false signals along the MCP. These then produce a background in the actual spectra. The addition of the electrostatic plates minimised these, removing a large part of this background. In this section we present the characterization of the overall MCP response before and after the installation of the electrostatic plate.

5.6.3 Methods of gain variation characterization

Before any corrections to the gain can be made, it is first necessary to characterize the actual MCP gain response along its length. It is theoretically possible to extract the MCP gain variation from the variation in the height of the Ta peak from a thin Ta/Si sample as it is swept across the MCP by a variation in *B* during the calibration process described in section 4.7.

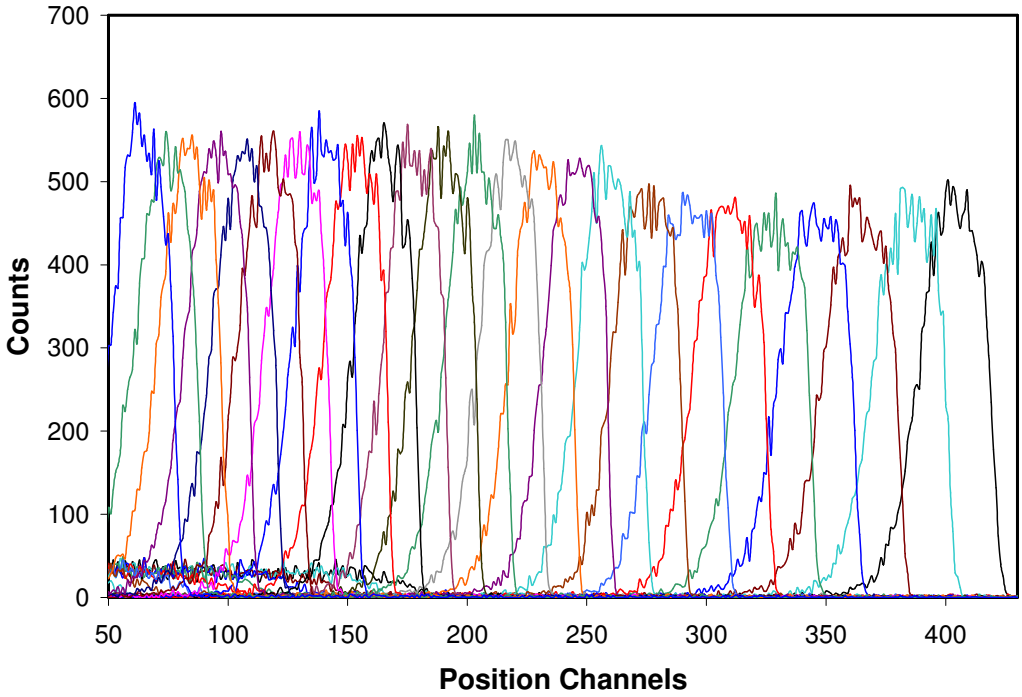

Fig. 5.14 The calibration data (also shown in Fig. 4.23) showing the variation in the height of the Ta peaks at different parts of the MCP.

However, there are several disadvantages to this approach. The calibration data only samples the MCP gain at fixed intervals along its length, so the gain at all other points has to be interpolated. Also, the height of each Ta peak is affected by the error in the incident accumulated beam charge reading from the charge digitizer, as well as the error-function fit for different peaks at different parts of the MCP which extracts the height information from each peak.

The alternative to the calibration data is to use a thick standard of uniform composition. A single spectrum of the thick standard will simultaneously measure the MCP gain at every part of the MCP. This eliminates both the problem of gain sampling at fixed intervals of MCP and the error in the measurement of accumulated incident charge for different Ta peaks. Also, a single spectrum of thick Au / Ni standard measured to an accumulated charge of ~ 15 μC is sufficient to reduce the statistical error to ~ 1 %. This approach is fast and solves the problems of accumulated incident charge error and individual peak height fitting. Here the MCP gain characterization is performed using spectra of a thick Au / Ni standard.

5.6.4 MCP Gain characterization using thick Au / Ni standard

An incident beam of 500 keV He^+ ions was collimated to an area of ~ 1 mm × 1 mm with a divergence of 0.5 mrad on a BCR CRM 328 Au / Ni standard tilted at 45º in IBM geometry. Ions backscattered at 65º are analyzed by the spectrometer and are collected by the MCP-FPD after passing between the electrostatic plates. Spectra at different field strength *B* were measured with and without an application of a 200 kVm^{-1} electrostatic field at accumulated target incident charge of 15 μC each, and the results are shown in Fig. 5.15.

The spectra taken at different *B* show the same structures at the same part of the MCP. This proves that these structures are not due to stoichiometric variations in the standard. The results show that the presence of an applied electrostatic field eliminated several small structures, the most prominent are those near position channels 240 and 350 as indicated in the figure.

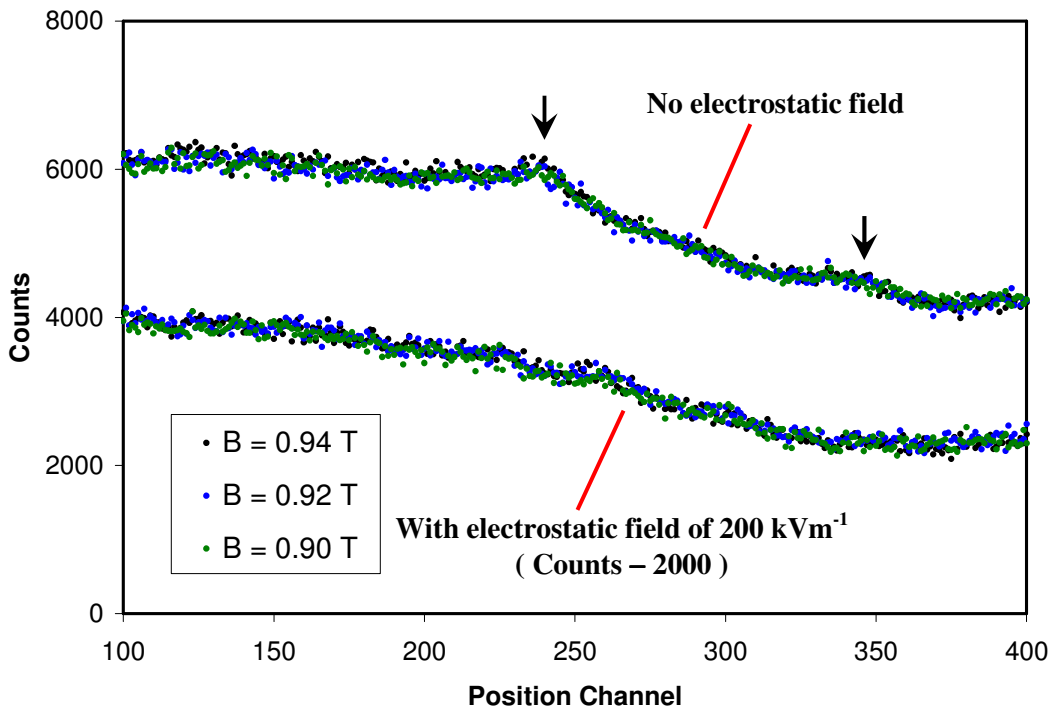

Fig. 5.15 Au / Ni position spectra taken at different spectrometer *B* with no applied field at the electrostatic plates and where there is an applied field of 200 kVm^{-1} between the plates. All spectra were taken to the same accumulated incident charge of 15 μC but the spectra taken with an applied field were shifted down vertically for easy comparison of the difference in the MCP response.

This means that a systematic error in the MCP response due to systematic stray ions were eliminated, leaving behind the true variation in the MCP amplification gain. All corrections developed in this section are for MCP responses with applied electrostatic field.

5.6.5 MCP Gain correction

The overview of the gain correction procedure is as follows:

i. Two windows of position spectra of the Au / Ni standard are taken at different *B*, one of which containing the surface edge of the Au RBS signal.

ii. Epsilon and energy values are assigned to the centre of each window.

iii. The ideal energy spectrum of Au is simulated using SIMNRA and reverse-binned into its position spectrum equivalent using REVBIN.

iv. The ratio of the ideal spectrum to the smoothed actual data in the window not containing the Au surface edge gives a list of correction factors that can be subsequently applied to all other position spectra measured.

Here, 4 position spectra of the Au / Ni standard are taken at different B_i, where $i = 1,2,3,4$. Window 1 contains the Au surface edge, window 2 will be used to calculate the gain correction factors, which will subsequently be applied to windows 3 and 4 for confirmation. Using the Au surface edge in window 1 and the procedure detailed in section 5.3.1, we assign values to the centre each window $E_{0,i}$. We choose the region from position channels $x_s = 100$ to $x_e = 400$ to correct for in each window (i.e. $n_x = 301$) and discard the fringe channels at the ends of the MCP with the sharp signal drop-off. The windows and their energies are shown in Fig. 5.16.

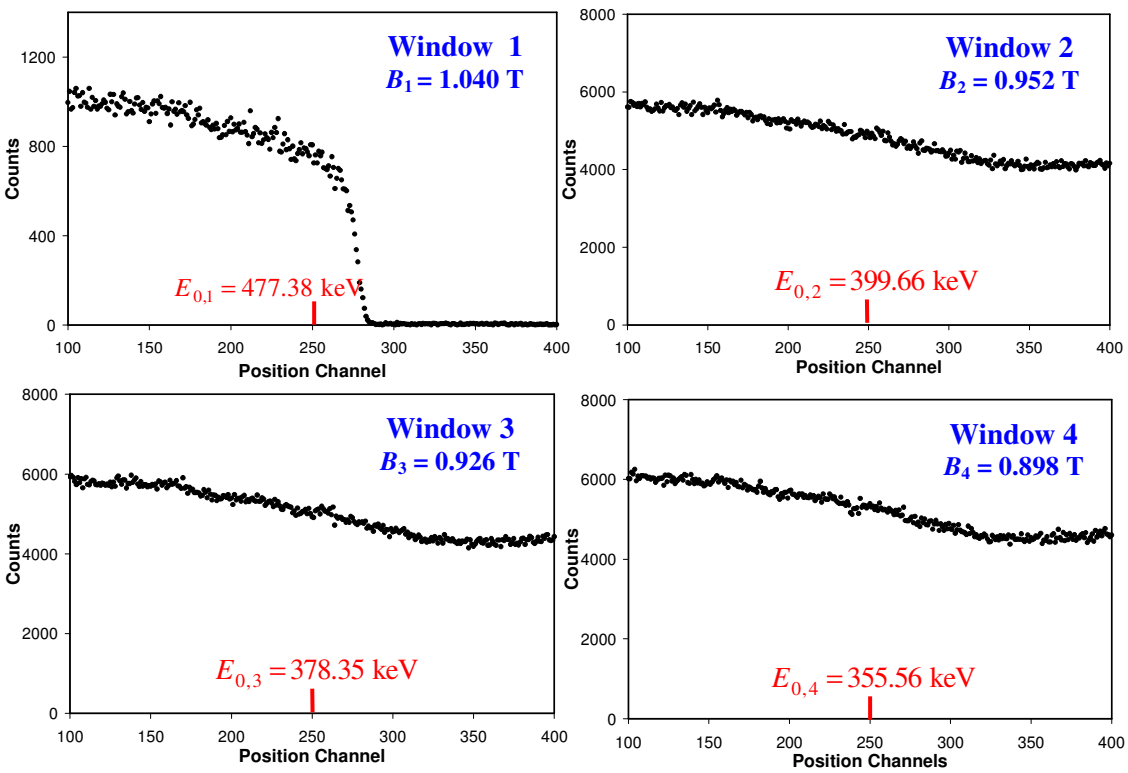

Fig. 5.16 Position spectra of all 4 windows at different spectrometer field strengths B_i, $i = 1,2,3,4$ with energy at centre of each window $E_{0,i}$.

Next, we calculate the energies $E_s^b = E_{0,2}\, C_R\left(100 - \frac{1}{2}\right)$ and $E_e^b = E_{0,2}\, C_R\left(400 + \frac{1}{2}\right)$ at the bounds corresponding to the chosen position region $\left[x_s, x_e\right]$, which we use to derive the energy per channel (keV/ch) and the energy offset (keV(0)) values of the ideal Au energy spectrum with 512 energy channels simulated using SIMNRA:

$$\mathbf{keV/ch} = \frac{E_e^b - E_s^b}{512} \quad \text{and} \quad \mathbf{keV(0)} = E_s^b - \frac{1}{2}\left[\mathbf{keV/ch}\right]$$

The ideal energy spectrum is then reverse-binned using REVBIN back into its equivalent position spectrum within the region $\left[x_s, x_e\right]$. A list of gain correction factors is then obtained at every position channel by taking the ratio of the (reverse-binned) ideal position spectrum to the smoothed actual data (so as to smoothen out the statistical interferences), as shown in Fig. 5.17.

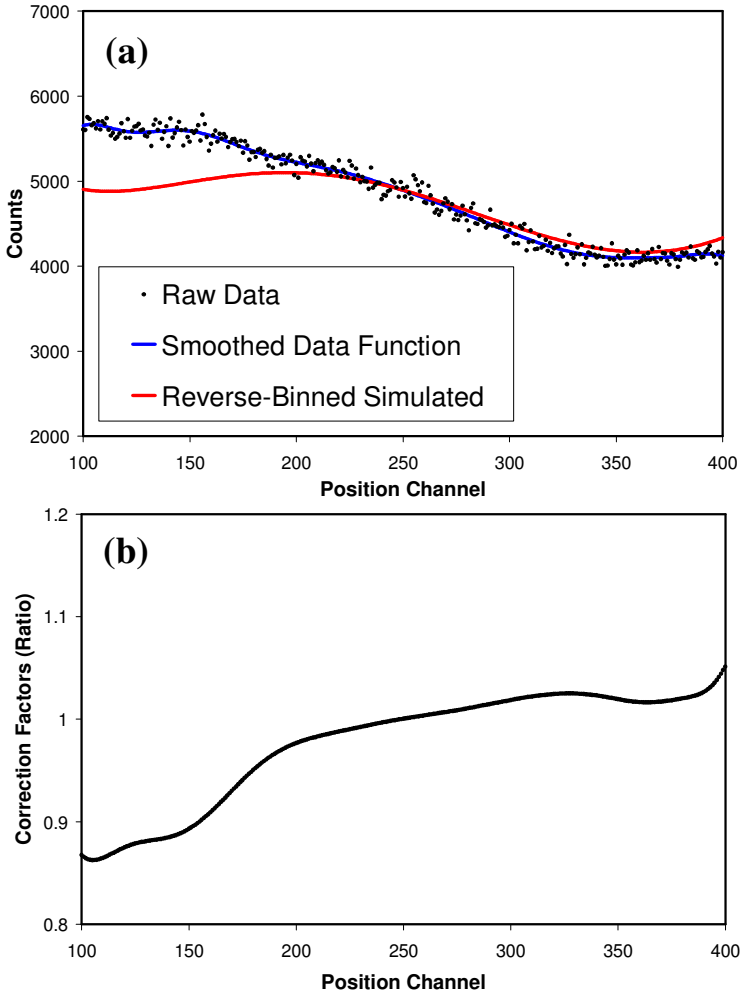

Fig. 5.17 **(a)** Plot of raw and smoothed data with the reverse-binned ideal position spectrum **(b)** Plot of the correction factors as a function of MCP position.

In theory, these correction factors can be applied to all raw position spectra output from the HRBS endstation to correct out effects from the MCP gain variation. To check that this is indeed the case, the correction factors are applied to each of the windows 2 to 4, before they undergo the forward binning process to be converted into energy spectra. If the correction factors work as expected, the energy spectra of all windows will show good agreement with their respective ideal energy spectrum simulated using SIMNRA. Each individual position window is forward-binned into energy spectra with and without the applied corrections, and are compared to the ideal simulated energy spectrum using SIMNRA in Fig. 5.18.

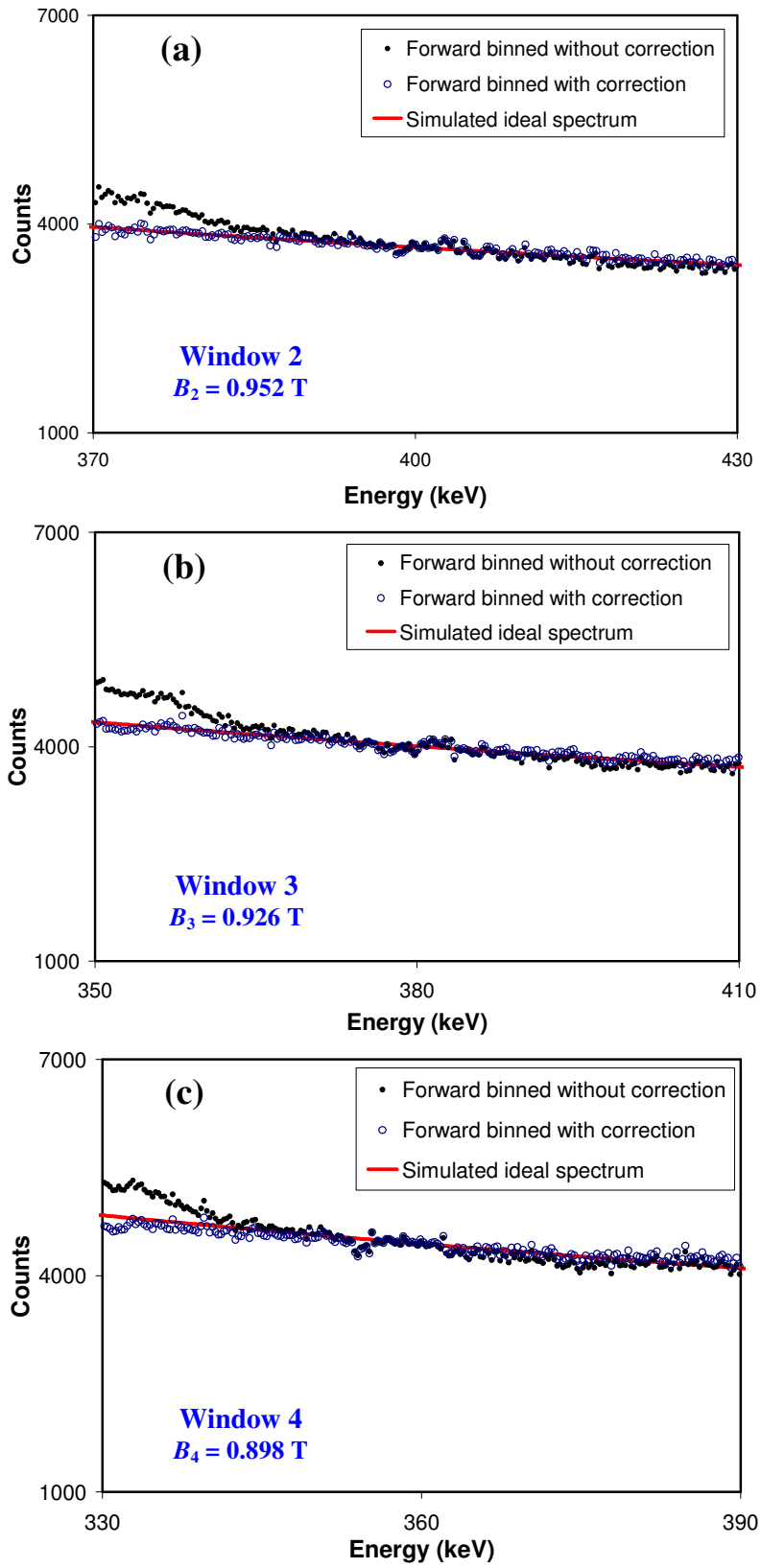

Fig. 5.18 Forward-binned energy spectra of individual windows with and without applied correction with simulated ideal energy spectra for individual position windows.

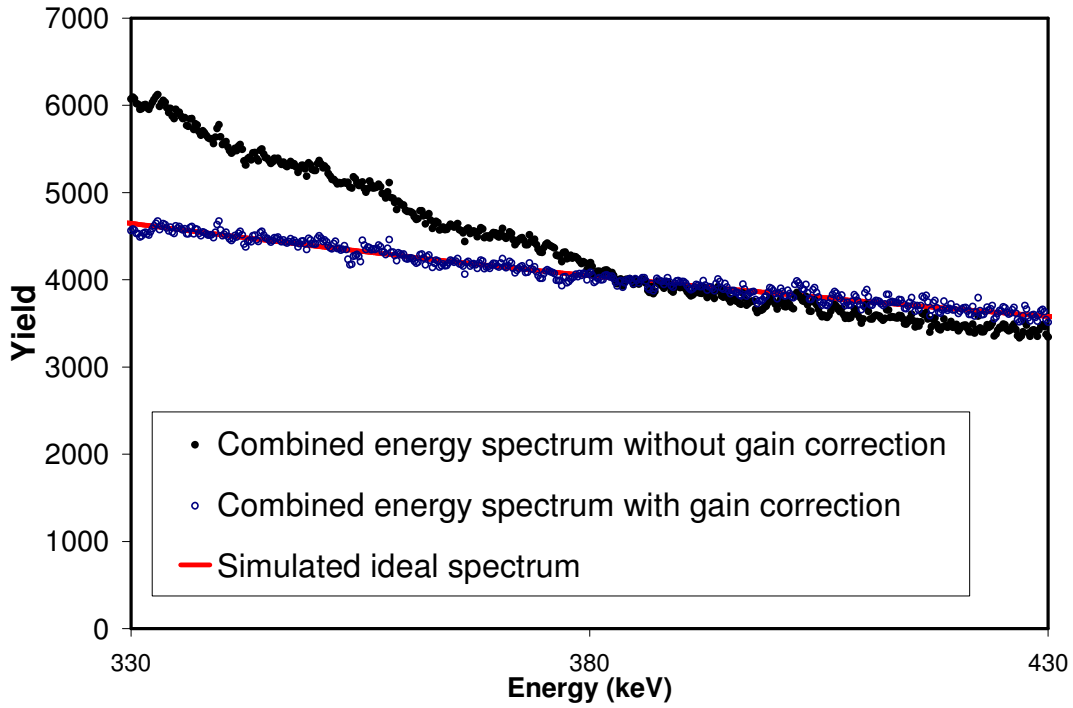

Fig. 5.19 The combined energy spectra from windows 2 - 4 with and without gain correction compared with the theoretical simulated spectrum.

The correction factors are self-consistent, as the corrected data forward-binned from position window 2 (from which we obtained the factors) show good agreement with the simulated ideal spectrum. Application of the same correction factors to data in other position windows also give energy spectra which are in good agreement to their respective ideal energy spectra. Fig. 5.19 shows the combined energy spectrum from all three windows. The spectrum applied with the gain correction shows much improved agreement with the simulated spectrum as compared with that without correction. We conclude that the correction factors work as expected and can be applied to any raw position spectra measured, though care must be taken to measure them with the same applied electrostatic field strength. The list of correction factors obtained with this procedure can be entered into the CompoundSP software provided by Kobelco and automatically applied to all other measured position spectra during the FORBIN process.

Chapter 6

Depth profiling and Strain analysis of Lu_2O_3 ultra-thin films

6.1 Equivalent Oxide Thickness (EOT)

In this chapter, the results of elemental depth profiling and interfacial Si lattice strain – depth analyses of Lu_2O_3/Si ultra-thin films are presented. All results were published in [21]. We first define a common quantity used in high-k dielectric studies: the Equivalent Oxide Thickness (EOT), where the EOT of a dielectric is defined to be the thickness of an equivalent SiO_2 layer which has the same value of capacitance per unit area, given by:

$$\frac{C}{A} = \frac{k_{\text{high-k}}\varepsilon_0}{t_{\text{high-k}}} = \frac{k_{\text{SiO}_2}\varepsilon_0}{t_{\text{SiO}_2}} \qquad \Rightarrow \qquad \text{EOT} = t_{\text{SiO}_2} = \frac{k_{\text{SiO}_2}}{k_{\text{high-k}}} \times t_{\text{high-k}}$$

where $t_{\text{high-k}}$ and $k_{\text{high-k}}$ are the thickness and dielectric constant of the high-k dielectric, while $t_{\text{SiO}_2} = \text{EOT}$ is the equivalent thickness of an SiO_2 layer with dielectric constant $k_{\text{SiO}_2} = 3.9$ and ε_0 is the permittivity of free space.

6.2 Film deposition using Pulsed Laser Deposition

The Lu_2O_3 thin films used in this study were deposited by the Micro-Electronics laboratory in the School of Materials Science and Engineering at the Nanyang Technological University of Singapore. The Lu_2O_3 ultra-thin films were deposited directly on p-type < 100 > Si substrate using Pulsed Laser Deposition (PLD) at a base pressure of 4.5×10^7 Torr. A 248 nm KrF excimer laser of frequency 5 Hz and an energy density of 1.5 J/cm^2 was used. The Si substrates were first cleaned using standard cleaning SC1 and SC2 solutions of Radio Corporation of America (RCA), and then dipped in a 1% HF solution to remove the native oxide. The substrates were then loaded into the deposition chamber immediately after the cleaning step to minimize the SiO_x formation. After deposition, the samples were subjected to Rapid Thermal Anneal (RTA) at temperatures ranging from 400 ºC to 800 ºC for 1 min in oxygen ambient, so as to test the stability of the film at various temperatures since the fabrication of the transistor would involve annealing process at as high as 1000 °C.

6.3 Elemental depth profiling of Lu_2O_3/Si film and interface

6.3.1 Experimental

The Lu_2O_3/Si samples were measured using a 500 keV He^+ beam which was collimated to 2×2 mm size with a divergence angle of less than 1 mrad. The beam was incident on the Lu_2O_3/Si sample and ions scattered at 65º were analyzed by the spectrometer and were collected by the MCP-FPD. Non-aligned (random) HRBS spectra of these samples were measured at a sample tilt of 40º under the IBM geometry, which were then simulated and fitted using the SIMNRA program to obtain the elemental depth profiles.

6.3.2 Depth profiling results

The non-aligned spectra of all samples are shown in Fig 6.1:

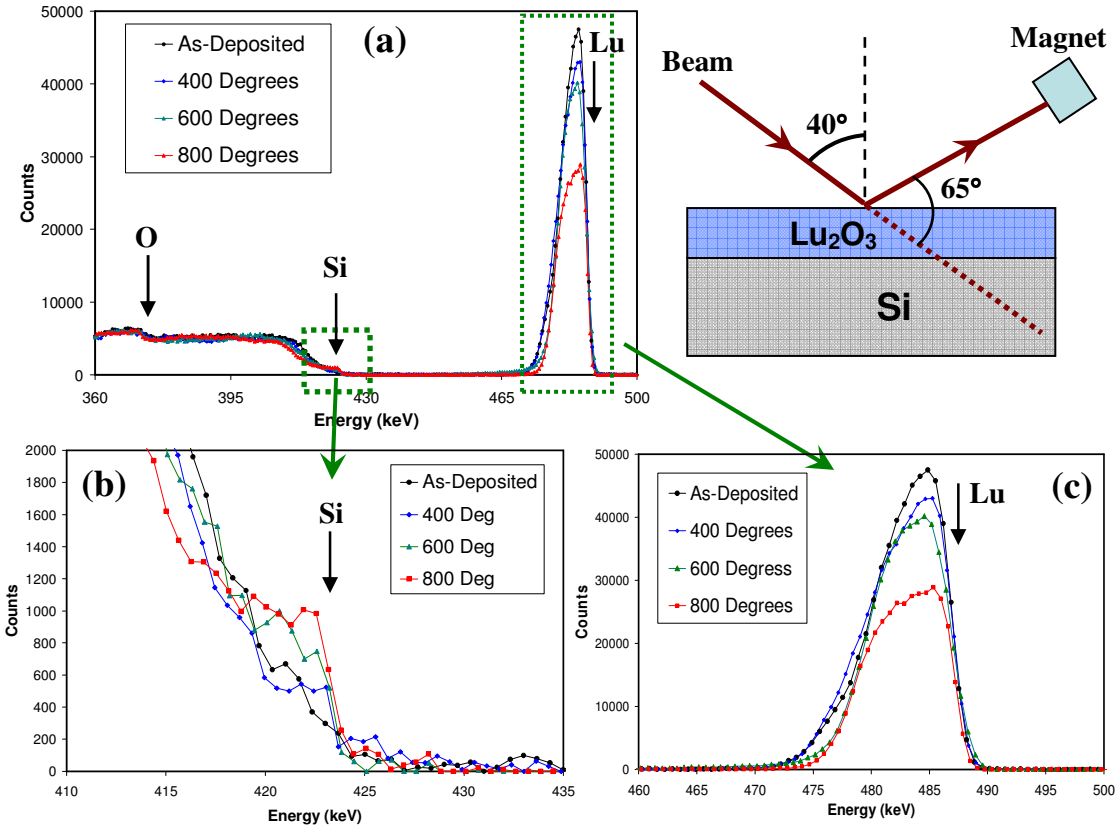

Fig 6.1 **(a)** HRBS non-aligned spectra of all samples and the schematic of the scattering geometry. **(b)** Expanded region at the Si surface edge. **(c)** Expanded region at Lu surface edge.

The spectra were forward-binned and processed with the MCP gain correction procedure described in the last chapter, but without an applied electrostatic field between the spectrometer and the MCP as the plates were yet to be installed at that time. The low-level linear background was subtracted from all spectra before they were plotted and compared. Fig. 6.1(a) shows an overview of the spectra and the scattering geometry, while the surface edges of Si and Lu were expanded and plotted in Fig. 6.1(b) and 6.1(c) respectively. Fig. 6.1(b) indicates a rising step at the Si surface energy, suggesting a movement of Si to the surface and the film with annealing. An increasing amount of Si on the surface and in the film as the annealing

temperature increases leads to a decreasing Lu stoichiometric ratio within the ultra-thin film, which is reflected in Fig 6.1(c) with a decrease in Lu peak height.

The spectra were separately fitted using SIMNRA, with the spectrum of the 400 ºC annealed sample and its fit shown in Fig 6.2. Care was taken to find the best fit for the Lu peak as well as the Si surface edge and interface. All the other samples are fitted in a similar manner. During the SIMNRA fits of the spectra, the interface layer roughness is taken into account: the fit assumes a broadening of the Lu inner edge only from the detection resolution and straggling. In order to describe the measured slope, an additional term for the roughness is introduced.

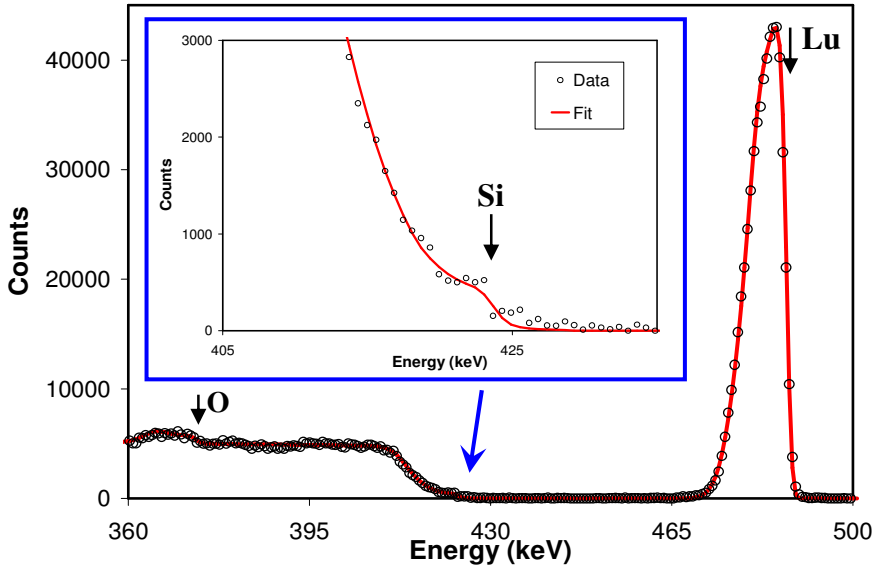

Fig 6.2 The spectrum of the sample annealed at 400 ºC fitted with SIMNRA, with an inset showing the detailed fit of the Si surface edge.

The elemental profiles of each sample were extracted directly from their respective target descriptions which provide a best fit for each of the separate spectra, which are then separately plotted in Fig. 6.3. The results indicate a ~ 5 nm film with a ~ 3 nm interface layer for the as-deposited sample, though the presence of Si is detected at ~ 3 nm below the surface with a stoichiometric ratio of 0.1, going up to ~ 0.5 at the interface layer.

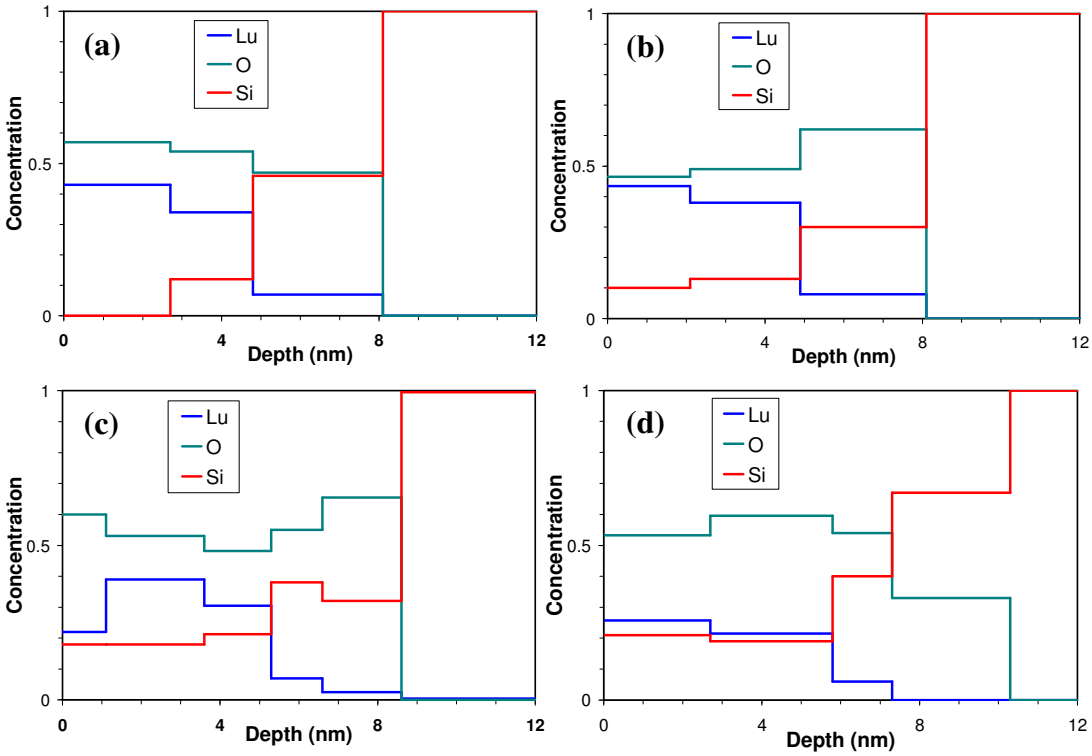

Fig 6.3 Elemental depth profiles of **(a)** as-deposited sample, as well as samples annealed at **(b)** 400 ºC **(c)** 600 ºC and **(d)** 800 ºC.

All annealed samples show the presence of Si on the surface, with a surface ratio of ~ 0.1 for the 400 ºC sample, going up to ~ 0.2 at the surface of the 600 ºC and 800 ºC samples. The slope of the low-energy edge of the Lu and the high-energy edge of Si indicates that the interface region is rough, and its thickness increases for annealing temperatures above 600 ºC. Also, a rough SiO_2 oxide interfacial layer is detected for the 800 ºC annealed sample. These results suggest that the quality of the interface region might be affected for annealing temperatures of 600 ºC and above. Uncertainties might arise from the simulation fit error, beam stopping power, counting statistics and beam straggling. The linear depths are also determined using an assumed value of film density that is calculated using the weighted average of the individual elemental densities. At the surface, the combined error for Lu is expected to be ~ 0.5%. This error will increase with depth due to straggling and the stopping power uncertainties.

6.4 Interfacial lattice strain measurement with HRBS channeling

The amorphous Lu_2O_3 film is expected to impose strain on the Si lattice at the interface region. Measurement of lattice strain at the interface of Lu_2O_3/Si was performed by HRBS using the channeling technique.

6.4.1 Ion channeling within a crystal

Ions incident onto a target with a lattice structure along a major crystalline axis may be steered into channels (i.e. "channeled") where they undergo a series of correlated, small angle collisions with the nuclei that line the channels.

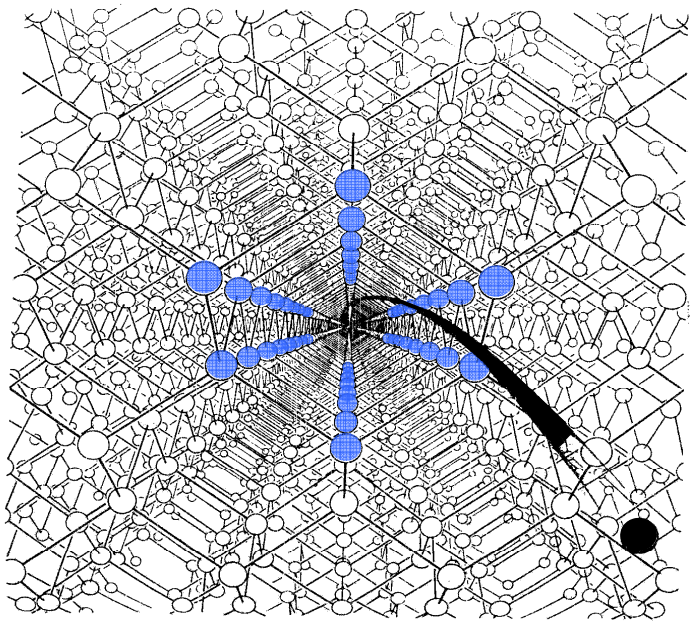

Fig. 6.4 Schematic of ion channeling. Source: [46]

The incident ions will be deflected by the first atom on the surface atomic layer, forming a "shadow cone" which shields the rest of the atoms lining the channel from head-on and close-encounter (low impact factor) approach by the ions (Fig. 6.5(a)). Subsequent encounters of channeled ions with lattice atoms will be small-angled collisions with large impact factors, with the ion trajectory exhibiting oscillatory behaviour within the channel (Fig. 6.5(b)) in near-surface regions. The backscattering

cross-section of channeled ions are therefore greatly reduced, the RBS signal from the crystalline (Si) substrate may fall by up to 98% of the random yield for pure crystals with clean surfaces along major axes.

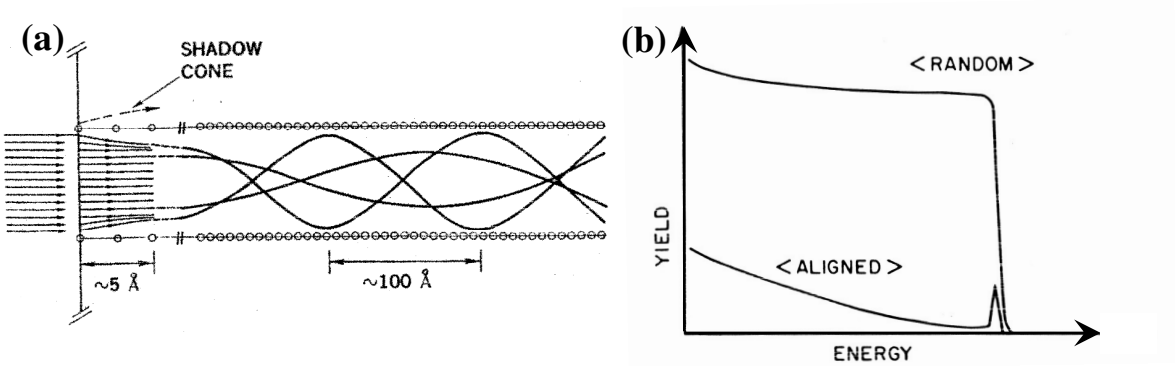

Fig 6.5 **(a)** Schematic of the formation of the shadow cone at the surface and the trajectories of channeled particles. The horizontal scale on the right is compressed in relation to the vertical scale to show the trajectory oscillations. **(b)** The comparison between the channeled and the non-aligned RBS spectrum. The channeled spectrum shows a drastically reduced substrate signal. Source: [46]

For amorphous thin films on a (single-crystal) Si substrate, lattice strain at the interface will be along the vertical direction, assuming that the film is laterally uniform. The angular broadening of the incident beam due to its passage through the amorphous thin film layer is not significant and the beam divergence should remain within the channeling critical angle when the beam encounters the Si substrate. A schematic of Si lattice under vertical strain as viewed along the < 110 > direction is shown in Fig 6.6(a). Interfacial lattice strain causes a shift in the < 111 > channeling direction with decreasing distance from the interface. A compressive strain causes a shift towards larger sample tilt while a tensile strain causes a shift towards a smaller sample tilt. A stereographic projection of a cubic Si lattice in the < 001 > direction is shown in Fig 6.6(b), which indicates an angular displacement of 54.74° between < 111 > and < 001 >. The projection is useful during experimental determination of the exact sample tilt in order to align the beam to the < 111 > axis.

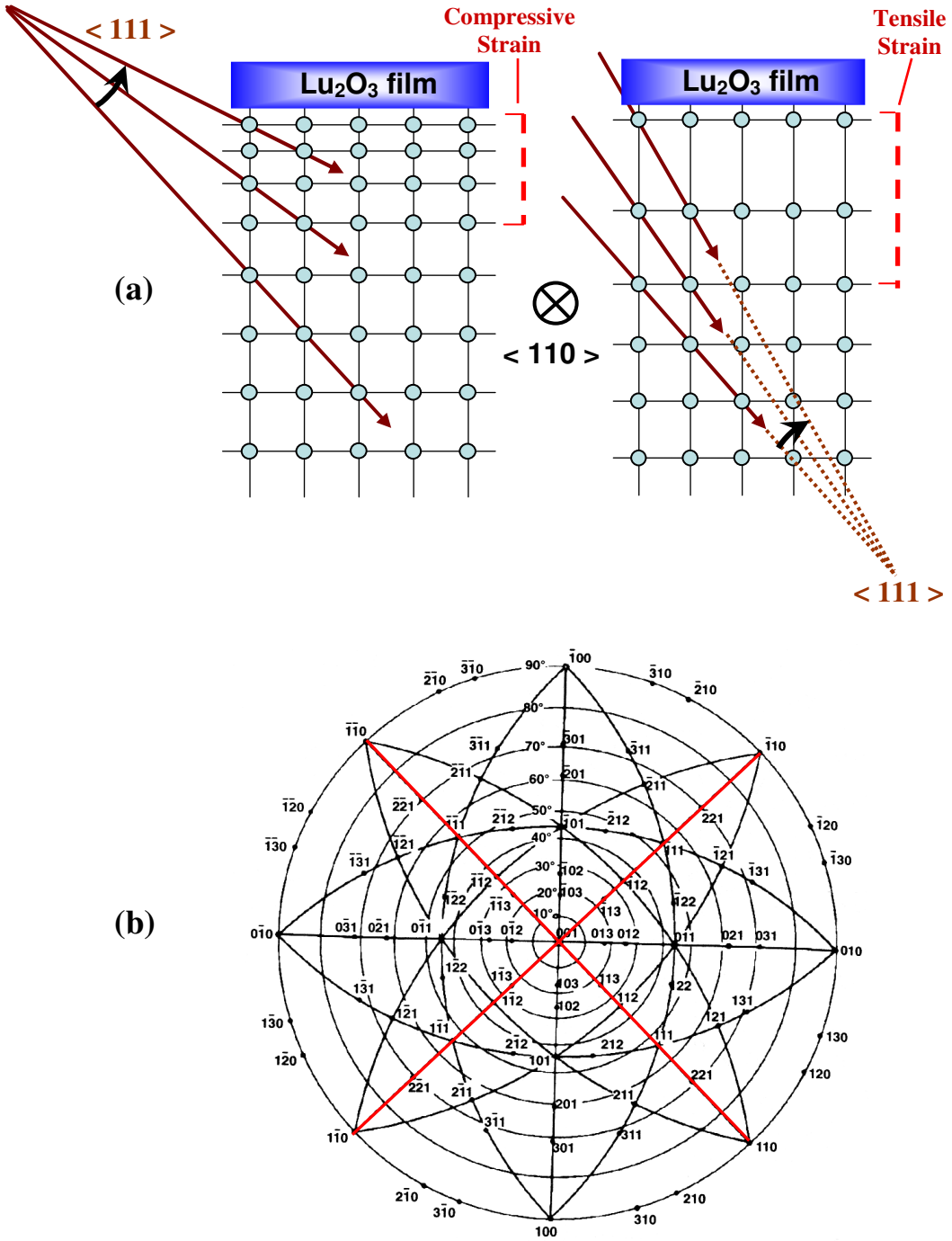

Fig 6.6 **(a)** Schematic angular shift of the < 111 > channeling direction with decreasing depth in Si lattice under vertical compressive and tensile strain at the film-substrate interface as viewed in the < 110 > direction. Sample tilt is defined as the angle between the < 111 > direction and the sample normal, which is along < 001 >. **(b)** The stereographic projection of a cubic < 001 > Si lattice showing the angular displacement of < 111 > from < 001 > along (110) or equivalent planes (red).

6.4.2 Estimation of lattice strain

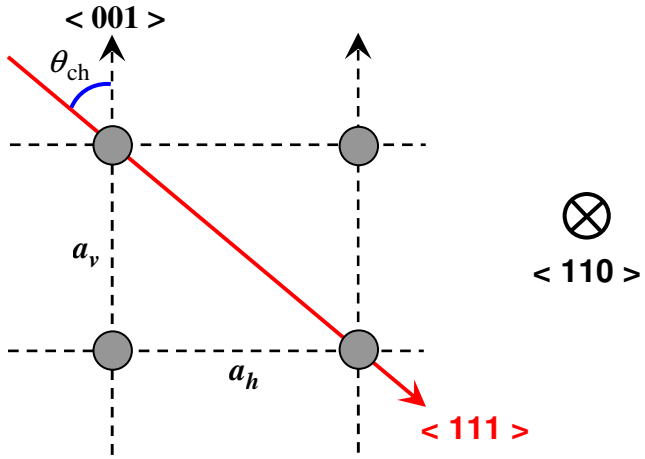

Fig. 6.7 Schematic of the lattice strain calculations.

From Fig. 6.7, the angle θ_{ch} between the target normal along < 001 > and the < 111 > axis of the unstrained Si lattice is related to the horizontal and vertical Si lattice constants a_h and a_v along the (110) plane by:

$$\tan\theta_{ch} = \frac{a_h}{a_v}$$

Therefore,

$$\sec^2\theta_{ch}\ \mathrm{d}\theta_{ch} = \frac{\mathrm{d}a_h}{a_h} - \left(\frac{a_h}{a_v}\right)\frac{\mathrm{d}a_v}{a_v} = \frac{\mathrm{d}a_h}{a_h} - \varepsilon_v \tan\theta_{ch}$$

where $\mathrm{d}a_h$ and $\mathrm{d}a_v$ are small changes in the Si lattice constants and ε_v is the vertical lattice strain. Assuming strain exists only in the vertical direction, $\mathrm{d}a_h = 0$ and hence

$$|\varepsilon_v| = \frac{\mathrm{d}\theta_{ch}}{\sin\theta_{ch}\cos\theta_{ch}} = 2\,\mathrm{cosec}\left(2\theta_{ch}\right)\mathrm{d}\theta_{ch}$$

where $\theta_{ch} = 54.74^\circ$ and $\mathrm{d}\theta_{ch}$ is the measured angular shift in the channeling dip.

6.4.3 HRBS angular scans of Lu_2O_3/Si samples

During angular scans, the sample tilt θ was varied using the goniometer along the (110) plane, and RBS spectra were measured at angular steps of 0.1° across the < 111 > axis schematically shown in Fig. 6.8(a).

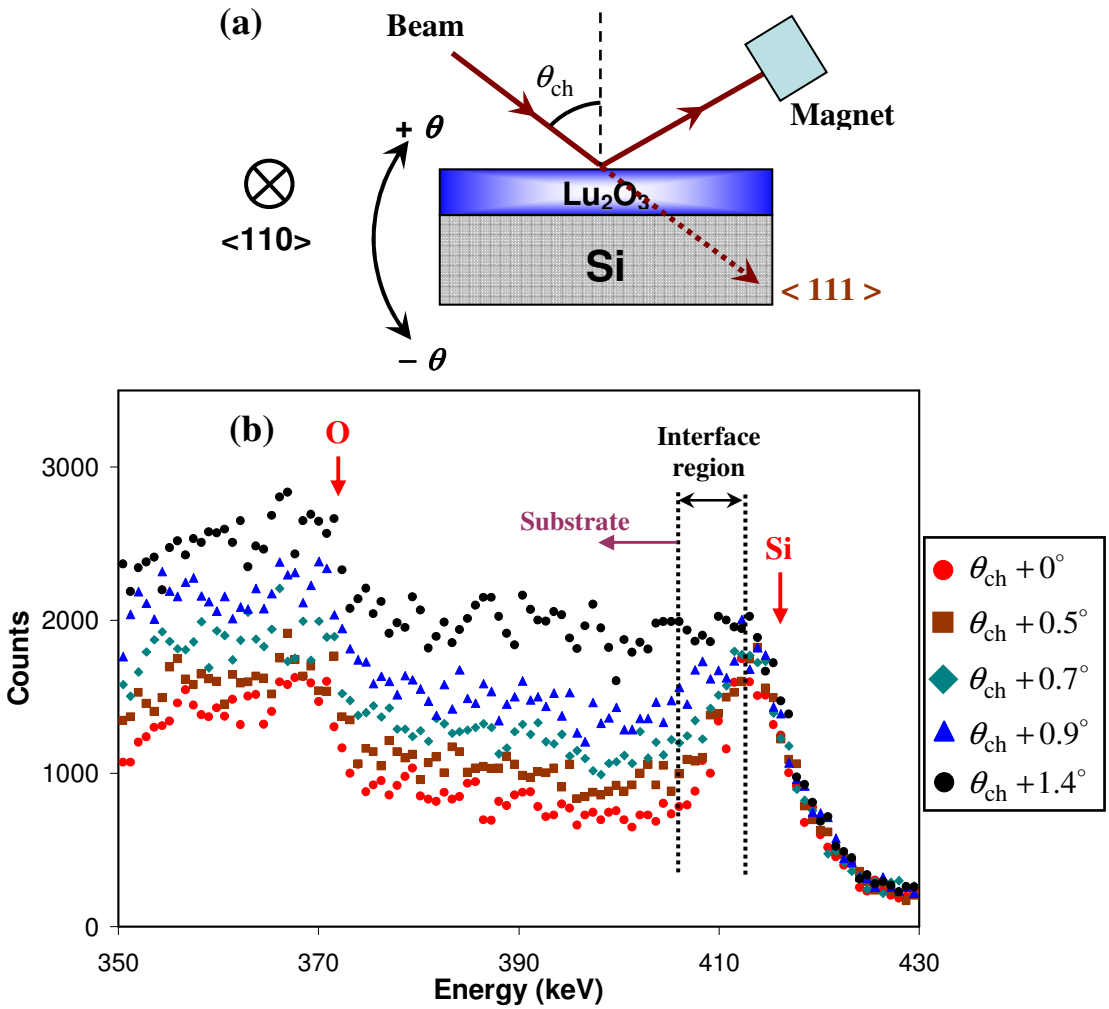

Fig 6.8 **(a)** Layout of the scattering geometry during angular scans. Increasing sample tilt angles is in the direction of $+\theta$. **(b)** Spectra taken at different sample tilt for the 400 °C annealed sample along the (110) plane. The Si substrate signal decreases near the < 111 > direction (θ_{ch}).

The interface region for every spectrum (Fig 6.8(b)) is divided into 5 strips of equal energy width corresponding to consecutive regions of ~ 1.5 nm thickness beneath the film-substrate interface. The total yield within each strip is calculated at every angular step θ and strips corresponding to different depth regions from the film–substrate

interface are plotted together as a function of angular displacement $\theta_1 = \theta - \theta_{ch}$ from the < 111 > direction for each of the four samples in Fig 6.9 (a) – (d), with positive θ_1 defined to be in the direction of larger sample tilt.

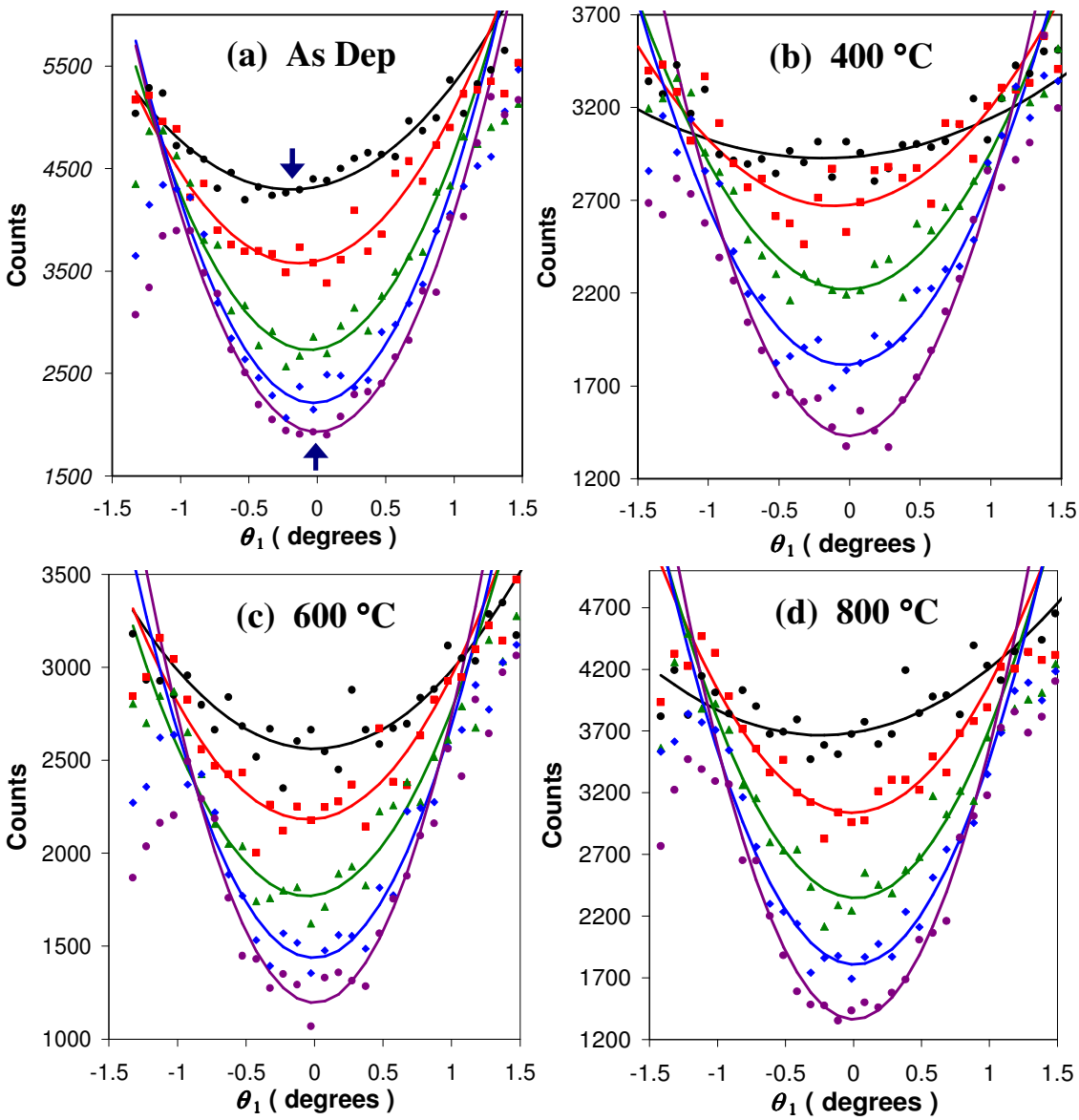

Fig 6.9 Angular scans for **(a)** As-deposited sample and samples annealed at **(b)** 400 °C, **(c)** 600 °C and **(d)** 800 °C. Each dip is fitted with a 2nd order polynomial function to determine its position.

Each set of data is fitted with a quadratic polynomial function, and the minimum of each fit is taken to be the position of that set. A shift in the < 111 > channeling dip position towards negative θ can be seen for the as-deposited sample as indicated in

Fig. 6.9(a), and shifts of decreasing magnitude in the same direction are seen for samples annealed at increasing temperature. This indicates a local tensile strain in the Si lattice at depths up to ~ 6 nm from the film-substrate interface. The estimated strain-depth variation for all samples are plotted in Fig 6.10.

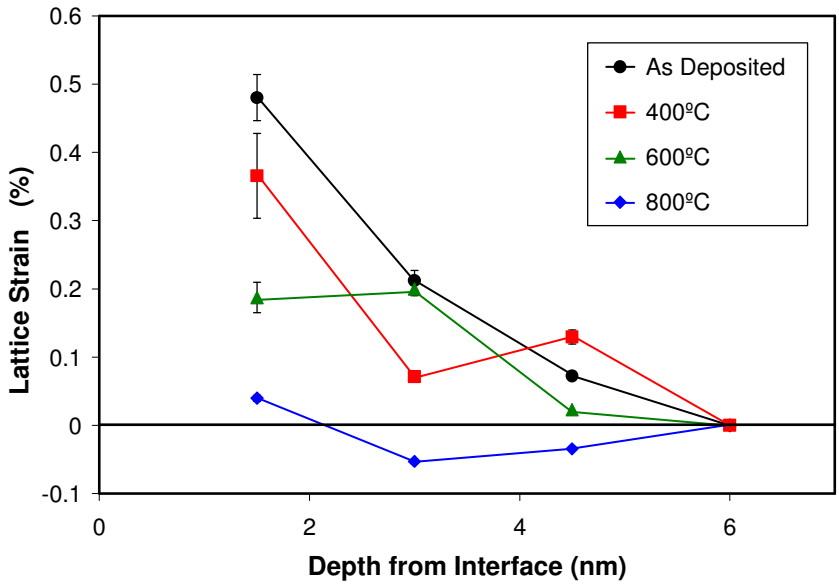

Fig 6.10 Plot of estimated lattice strain (%) vs depth in Si beneath the film-substrate interface.

The strain is largest at regions next to the interface in all samples, and decreases in magnitude with increasing distance from the interface, reducing to below detection limit at distances beyond 6 nm. Magnitude of interface lattice strain is largest in the as-deposited sample at ~ 0.5 %, decreasing with samples annealed at increasing temperature, so that the strain in the 800 ºC annealed sample is below detection limit.

6.5 Conclusion

The elemental depth profiling of ultra-thin Lu_2O_3/Si films and strain-depth profiling of the Si lattice beneath the film-substrate interface have been performed. Si is found to have diffused to the surface after annealing, and a rough interface region with

intermixing of Lu, O and Si exists for all films. Angular scans across < 111 > axis along the < 110 > plane show channeling dip shifts towards smaller sample tilt angles, indicating a tensile strain of the Si lattice at the interface. The lattice strain magnitude is largest in the as-deposited sample and decreases with annealing temperature with strain in the 800 ºC below detection limits.

Chapter 7

Conclusion and Future directions

7.1 Conclusion

The HRBS detection system was carefully characterized in order to ensure the accuracy and quality of the output spectra. The ion optics was studied using analytical approaches, as well as full numerical modeling using SIMION. The results from these calculations show good agreement with experimental data, and the design of the spectrometer was validated.

The code FORBIN was written in Mathematica in order to process the final output position spectra into energy spectra, and another code REVBIN was written to reverse this process. A novel method to correct for the non-uniformities of the MCP gain using REVBIN was developed. This process is self-consistent and was shown to have eliminated artefacts and signals in the position spectra. The correction procedure can be applied to all position spectra, since the MCP gain response is found to be time independent.

With these studies and corrections, we conclude that both the spectrometer and MCP-FPD functions within theoretical and design expectations, and the output spectra are accurate.

Ultra-thin Lu_2O_3/Si films were studied using HRBS as candidates for next-generation MOSFET gate dielectrics. Lu_2O_3 films deposited on Si using PLD and annealed at different temperatures were shown by HRBS depth profiling to have formed rough interfaces with Si whose thicknesses increase with increasing annealing temperature. Angular scans during HRBS strain analysis have been conducted to measure the lattice strain of Si at the film interface. Dip shifts towards smaller angles were observed, indicating that the Si lattice is under vertical tensile strain at the film interface, assuming that the lattice and film are laterally uniform. The lattice strain of the as-deposited sample was measured to be ~ 0.5%. Samples annealed at increasing temperature showed decreasing lattice strain.

In conclusion, the HRBS is a highly useful spectrometric method to probe the composition and structure of thin films. The HRBS endstation in CIBA at NUS works correctly and the accuracy of the output spectra is further enhanced by this work. Studies performed on ultra-thin Lu_2O_3/Si films has shown the formation of a rough interfacial layer and vertical Si lattice strain at the interface of each sample.

7.2 Future directions

Two ways forward from this point are immediately obvious:

- Two-dimensional Data Acquisition system
- Investigation of ultra-thin Lu_2O_3/Ge films

Two-dimensional Data Acquisition system

Currently, the HRBS endstation can only acquire one type of data at any one time: either the position output or the energy (SUM) output from the PSDA (Fig. 3.13). Currently, only the position output is used during measurements, and the spectra obtained are counts sorted according to the position of ion incidence along the MCP. The SUM output gives us counts sorted according to the magnitude of the total charge collected from both ends of the MCP during every ion incidence event. Events with low SUM signals might be due to stray ions or cross-channel effects in the MCP. A data acquisition system which can simultaneously process both outputs in a two-dimensional display will allow the mapping of both position and energy (SUM) to every count. It will then be possible to perform SUM discrimination where counts of low SUM signals are ignored, further eliminating noise and background from the output spectra.

Investigation of ultra-thin Lu_2O_3/Ge films

Recently, there has been interest in investigating Ge as an alternative channel material for future MOSFET downscaling [47 – 48], due to its higher electron and hole mobilites as compared to Si. HRBS depth profiling has already been performed in CIBA on thin Al_2O_3/Lu_2O_3/Ge films annealed at different temperatures [49]. Possible future work include interfacial strain profiling of such systems to investigate the lattice strain imposed on the Ge channel by the Lu_2O_3 dielectric which will alter the carrier mobilities. It would also be interesting to investigate the effect of the metal gate on the depth profiles of the dielectric by performing HRBS measurements of systems with a thin layer of metal gate material deposited on such systems.

Biliography

[1] K. Kimura, K. Ohshima, M. Mannami, Applied Physics Letters 64 (1994) 2232.

[2] L. Byoung Hun, S. Seung Chul, C. Rino, P. Kirsch, IEEE Transactions on Electron Devices 55 (2008) 8.

[3] J.P. Locquet, C. Marchiori, M. Sousa, J. Fompeyrine, S. Jin Won, Journal of Applied Physics 100 (2006) 51610.

[4] H. Wong, H. Iwai, Microelectronic Engineering 83 (2006) 1867.

[5] P. Ranade, T. Ghani, K. Kuhn, K. Mistry, S. Pae, L. Shifren, M. Stettler, K. Tone, S. Tyagi, M. Bohr, High performance 35 nm LGATE CMOS transistors featuring NiSi metal gate (FUSI), uniaxial strained silicon channels and 1.2 nm gate oxide, Institute of Electrical and Electronics Engineers Inc., Piscataway, NJ 08855-1331, United States, 2005, pp. 217.

[6] K. Mistry, et al., A 45 nm logic technology with high-k+ metal gate transistors, strained silicon, 9 Cu interconnect layers, 193 nm dry patterning, and 100% Pb-free packaging, Institute of Electrical and Electronics Engineers Inc., Piscataway, NJ 08855-1331, United States, 2007, pp. 247.

[7] H. Iwai, et al., Advanced gate dielectric materials for sub-100 nm CMOS, Institute of Electrical and Electronics Engineers Inc., 2002, pp. 625.

[8] H. Wu, Y. Zhao, M.H. White, Solid-State Electronics 50 (2006) 1164.

[9] A.V. Prokofiev, A.I. Shelykh, B.T. Melekh, Journal of Alloys and Compounds 242 (1996) 41.

[10] P. Darmawan, P.S. Chia, P.S. Lee, Journal of Physics: Conference Series 61 (2007) 229.

[11] P. Darmawan, P.S. Lee, Y. Setiawan, J. Ma, T. Osipowicz, Applied Physics Letters 91 (2007) 092903.

[12] P. Darmawan, C.L. Yuan, P.S. Lee, v 138 (2006) 571.

[13] K. Nakajima, M. Suzuki, K. Kimura, M. Yamamoto, A. Teramoto, T. Ohmi, T. Hattori, Japanese Journal of Applied Physics, Part 1 45 (2006) 2467.

[14] K. Kimura, K. Nakajima, H. Kobayashi, S. Miwa, K. Satori, SIMS and high-resolution RBS analysis of ultrathin SiO_xN_y films, Elsevier, Netherlands, 2003, pp. 418.

[15] K. Kimura, K. Nakajima, Y. Okazaki, H. Kobayashi, S. Miwa, K. Satori, Japanese Journal of Applied Physics, Part 1: Regular Papers and Short Notes and Review Papers 39 (2000) 4663.

[16] K. Nakajima, S. Joumori, M. Suzuki, K. Kimura, T. Osipowicz, K.L. Tok, J.Z. Zheng, A. See, B.C. Zhang, Applied Physics Letters 83 (2003) 296.

[17] M. Zhao, et al., Oxidation process of $HfO_2/SiO_2/Si$ structures observed by high-resolution RBS, IEEE, Piscataway, NJ, USA, 2006, pp. 4 pp.

[18] M. Zhao, K. Nakajima, M. Suzuki, K. Kimura, M. Uematsu, K. Torii, S. Kamiyama, Y. Nara, K. Yamada, Applied Physics Letters 88 (2006) 153516.

[19] K. Kimura, Z. Ming, K. Nakajima, M. Suzuki, High-resolution rutherford backscattering spectroscopy for Nano-CMOS applications, Institute of Electrical and Electronics Engineers Computer Society, Piscataway, NJ 08855-1331, United States, 2006, pp. 89.

[20] T. Osipowicz, H.L. Seng, T.K. Chan, B. Ho, Nuclear Instruments and Methods in Physics Research, Section B: Beam Interactions with Materials and Atoms 249 (2006) 915.

[21] T.K. Chan, P. Darmawan, C.S. Ho, P. Malar, P.S. Lee, T. Osipowicz, Nuclear Instruments and Methods in Physics Research Section B: Beam Interactions with Materials and Atoms 266 (2008) 1486.

[22] M. Natasi, J.W. Mayer, J.K. Hirvonen, Ion-Solid Interactions: Fundamentals and Applications, Cambridge University Press, New York, 1996.

[23] H.H. Andersen, F. Besenbacher, P. Loftager, W. Moller, Physical Review A (General Physics) 21 (1980) 1891.

[24] J. L'Ecuyer, J.A. Davies, N. Matsunami, Nuclear Instruments and Methods 160 (1979) 337.

[25] M. Mayer, SIMNRA User's Guide, Max-Plank-Institut Fur Plasmaphysik, Garching, Germany, 2006.

[26] J.F. Ziegler, Helium-Stopping powers and ranges in all elemental matter, Pergamon, Oxford, UK, 1977.

[27] J.F. Ziegler, J.P. Biersack, U. Littmark, Stopping and range of ions in solids, Pergamon Press, New York, NY, USA, 1985.

[28] J.F. Ziegler, J.M. Manoyan, Nuclear Instruments & Methods in Physics Research Section B-Beam Interactions with Materials and Atoms 35 (1988) 215.

[29] W.K. Chu, Physical Review A (General Physics) 13 (1976) 2057.

[30] E. Szilagyi, F. Paszti, G. Amsel, Nuclear Instruments & Methods in Physics Research, Section B: Beam Interactions with Materials and Atoms 100 (1995) 103.

[31] Q. Yang, D.J. O'Connor, Z. Wang, Nuclear Instruments & Methods in Physics Research, Section B: Beam Interactions with Materials and Atoms 61 (1991) 149.

[32] W.K. Chu, Backscattering Spectrometry, Academic Press, New York, 1978.

[33] HVEE, 3.5 MV Singletron Accelerator Manual, Netherlands, 1998.

[34] F. Watt, M.B.H. Breese, A.A. Bettiol, J.A. van Kan, Materials Today 10 (2007) 20.

[35] F. Watt, T. Osipowicz, T.F. Choo, I. Orlic, S.M. Tang, Nuclear Instruments & Methods in Physics Research, Section B: Beam Interactions with Materials and Atoms 136-138 (1998) 313.

[36] HVEE, HVE Documentation, Ion Source Model 173 Manual, Netherlands, 1998.

[37] KOBELCO, High Resolution RBS End Station System Documentation, Kobe, 2003.

[38] S. Wolfram, The Mathematica Book, third edition., Cambridge University Press, Cambridge, 1996.

[39] S. Penner, The Review of Scientific Instruments 32 (1961) 150.

[40] D.A. Dahl, SIMION 7 User Manual, Idaho National Laboratory, Idaho, 2000.

[41] D.L. Judd, The Review of Scientific Instruments 21 (1950) 213.

[42] M. Camac, The Review of Scientific Instruments 22 (1951) 197.

[43] G.C. William, The Review of Scientific Instruments 22 (1951) 717.

[44] J.P. Biersack, S. Berg, C. Nender, Nuclear Instruments & Methods in Physics Research, Section B: Beam Interactions with Materials and Atoms 59-60 (1991) 21.

[45] C.S. Ho, The Study of Ultra-thin Diffusion Barriers in Copper Interconnect System, Dissertation, NUS, 2009.

[46] L.C. Feldman, J.W. Mayer, S.T. Picraux, Materials Analysis By Ion Channeling: Submicron Crystallography, Academic Press, New York, 1982.

[47] C. Beer, et al., Applied Physics Letters 91 (2007) 263512.

[48] G. Mavrou, S. Galata, P. Tsipas, A. Sotiropoulos, Y. Panayiotatos, A. Dimoulas, E.K. Evangelou, J.W. Seo, C. Dieker, Journal of Applied Physics 103 (2008) 014506.

[49] P. Darmawan, M.Y. Chan, T. Zhang, Y. Setiawan, H.L. Seng, T.K. Chan, T. Osipowicz, P.S. Lee, Applied Physics Letters 93 (2008) 062901.

[50] J.F. Ziegler, R.F. Lever, Calculations of elastic scattering of ^{4}He projectiles from thin layers, Switzerland, 1973, pp. 291.

Appendices

A1 Central force elastic binary scattering in CM frame

Due to the absence of transverse forces, the entire scattering event happens along a plane defined by the initial velocity vector of the ion and the initial target nuclei position. Consider the orthogonal coordinates r and Θ_c (Fig. A.1), where $r = r_1 + r_2$ such that:

$$r_1 = \frac{M_2}{M_1 + M_2} r \qquad \text{and} \qquad r_2 = \frac{M_1}{M_1 + M_2} r$$

and Θ_c is the angle between r and the line perpendicular to $r_{\min}$.

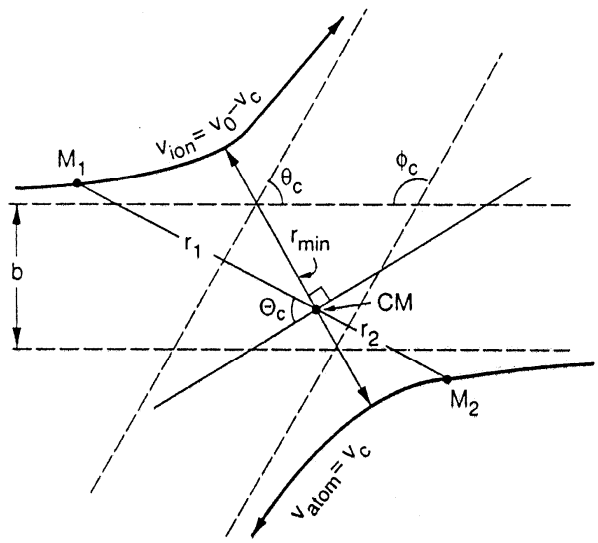

Fig. A.1 Schematic of binary scattering. Source: [22]

Conservation of angular momentum relates the angular momentum $l = M_c r^2 \dot{\Theta}_c$ to its asymptotic value at large r:

$$l = M_c r^2 \dot{\Theta}_c = M_c v_0 b$$

$$\therefore \quad \dot{\Theta}_c = \frac{v_0 b}{r^2}$$

Conservation of Energy then yields:

$$E_c = \frac{1}{2}M_c v_0^{\,2} = \frac{1}{2}M_c\left(\dot{r}^2 + r^2\dot{\Theta}_c^{\,2}\right) + V(r)$$

$$= \frac{1}{2}M_c\left(\dot{r}^2 + r^2\left(\frac{v_0 b}{r^2}\right)^2\right) + V(r)$$

Solving for $\dot{r}$, we obtain

$$\dot{r} = v_0\sqrt{1 - \frac{V(r)}{E_c} - \left(\frac{b}{r}\right)^2}$$

$$\Rightarrow \quad \frac{d\Theta}{dr} = \frac{\dot{\Theta}_c}{\dot{r}} = \frac{b}{r^2\sqrt{1 - \frac{V(r)}{E_c} - \left(\frac{b}{r}\right)^2}}$$

The trajectory of both M_1 and M_2 are symmetric about $r_{\min}$. Integrating over the second half of the trajectory of M_1,

$$\int_{\frac{\pi}{2}}^{\pi-\frac{\theta_c}{2}} d\Theta_c = \int_{r_{\min}}^{\infty} \frac{b\,dr}{r^2\sqrt{1 - \frac{V(r)}{E_c} - \left(\frac{b}{r}\right)^2}}$$

$$\therefore \quad \theta_c = \pi - 2b\int_{r_{\min}}^{\infty} \frac{dr}{r^2\sqrt{1 - \frac{V(r)}{E_c} - \left(\frac{b}{r}\right)^2}}$$

A2 Conversion of scattering cross-section from CM to Lab frame

The Rutherford Scattering Cross-section in the CM reference frame is:

$$\left.\frac{d\sigma(\theta_c)}{d\Omega}\right|_{\text{Rutherford,CM}} = \left(\frac{\alpha}{4E_c}\right)^2 \frac{1}{\sin^4\left(\frac{\theta_c}{2}\right)}$$

where $\alpha = Z_1 Z_2 e^2$, E_c and θ_c are the CM energy and scattering angles respectively.

To convert this to the Lab frame equivalent [50], we note the fact that the number of ions scattered into per unit solid angle is the same in both frames:

$$\frac{d\sigma}{d\Omega_{\text{Lab}}}\left(d\Omega_{\text{Lab}}\right) = \frac{d\sigma}{d\Omega_{\text{CM}}}\left(d\Omega_{\text{CM}}\right)$$

$$\frac{d\sigma}{d\Omega_{Lab}}\left(2\pi\sin\theta d\theta\right) = \frac{d\sigma}{d\Omega_{CM}}\left(2\pi\sin\theta_c d\theta_c\right)$$

$$\therefore \frac{d\sigma}{d\Omega_{Lab}} = \frac{d\sigma}{d\Omega_{CM}}\left(\frac{\sin\theta_c}{\sin\theta}\right)\left(\frac{d\theta_c}{d\theta}\right)$$

But since $\theta_c = \theta + \theta'$ and $\sin\theta' = \mu\sin\theta$ (Fig. 2.2), we have

$$\frac{d\theta_c}{d\theta} = 1 + \frac{d\theta'}{d\theta} = 1 + \frac{\mu\cos\theta}{\cos\theta'} = \frac{\sin\theta_c}{\sin\theta\cos\theta'}$$

where $\cos\theta' = \sqrt{1-\mu^2\sin^2\theta}$.

$$\therefore \frac{d\sigma}{d\Omega_{\text{Lab}}} = \frac{d\sigma}{d\Omega_{\text{CM}}}\left(\frac{\sin\theta_c}{\sin\theta}\right)^2 \frac{1}{\cos\theta'}$$

$$= \left(\frac{Z_1 Z_2 e^2}{4E_0}\right)^2 \left[\frac{(1+\mu)\sin\theta_c}{\sin^2\left(\frac{\theta_c}{2}\right)}\right]^2 \frac{1}{\sin^2\theta\cos\theta'}$$

Noting that

$$\frac{\sin\theta_c}{\sin^2\left(\frac{\theta_c}{2}\right)} = 2\cot\left(\frac{\theta_c}{2}\right) \qquad \text{and} \qquad \frac{\cos\theta + \cos\theta'}{\sin\theta + \sin\theta'} = \cot\left(\frac{\theta_c}{2}\right),$$

we have

$$\left[\frac{(1+\mu)\sin\theta_c}{\sin^2\left(\frac{\theta_c}{2}\right)}\right] = \left[2(1+\mu)\cot\left(\frac{\theta_c}{2}\right)\right] = 4\left[\frac{\cos\theta + \cos\theta'}{\sin\theta}\right]$$

so that finally,

$$\begin{aligned}
\frac{d\sigma}{d\Omega_{Lab}} &= \left(\frac{Z_1 Z_2 e^2}{4E_0}\right)^2 \left[\frac{\cos\theta + \cos\theta'}{\sin\theta}\right]^2 \frac{4}{\sin^2\theta\cos\theta'} \\
&= \left(\frac{Z_1 Z_2 e^2}{2E_0}\right)^2 \frac{\left[\cos\theta + \cos\theta'\right]^2}{\sin^4\theta\cos\theta'} \\
&= \left(\frac{Z_1 Z_2 e^2}{2E_0}\right)^2 \frac{[\cos\theta + \sqrt{1-\mu^2\sin^2\theta}]^2}{\sin^4\theta\sqrt{1-\mu^2\sin^2\theta}}
\end{aligned}$$

A3 Impulse approximation

For collisions where $M_1 \gg M_2$ or when b is large, the trajectory of M_1 is only slightly perturbed. This results in small scattering angle θ_c as well as small change in ion speed during the collision.

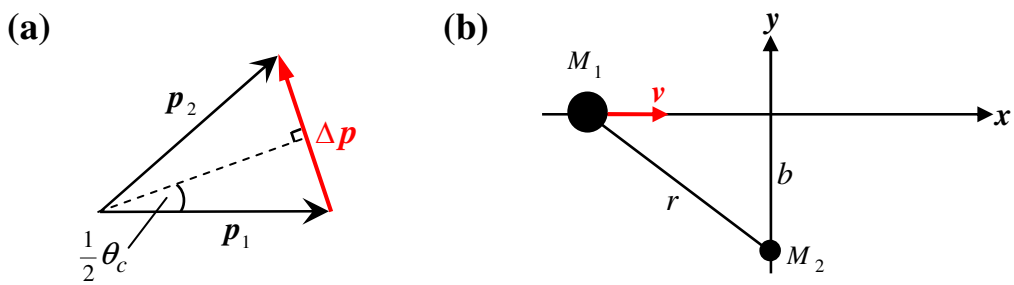

Fig. A.2 Schematics of impulse approximation calculations.

Let $\boldsymbol{p}_1$ and $\boldsymbol{p}_2$ be the momentum of M_1 before and after collision with M_2, resulting the change in momentum $\Delta \boldsymbol{p}$. The ion speed is assumed to be unchanged during the collision, therefore from Fig. A.2(a), we have

$$\sin\left(\frac{\theta_c}{2}\right) = \frac{\frac{1}{2}\Delta p}{|p|} = \frac{\Delta p}{2M_1 v}.$$

The symmetry of the collision (Fig. A.2(b)) allows us to write

$$\Delta p = \int_{-\infty}^{\infty} F_y \, dt = \int_{-\infty}^{\infty} \frac{F_y}{v} \, dx,$$

where $F_y = -\frac{dV(r)}{dy} = -\frac{dV(r)}{db}$ is the component of the force acting on M_1 (and hence on M_2) along the y direction.

$$\therefore \Delta p = -\frac{1}{v}\frac{d}{db}\int_{-\infty}^{\infty} V(r)\, dx \quad \text{with} \quad r = \sqrt{x^2 + b^2}.$$

Using this expression of Δp for an ion of mass M_1 and charge $Z_1 e$ undergoing small-angle Coulomb scattering with a target electron of mass m_e, the momentum imparted onto the stationary electron is:

$$\begin{aligned}
\Delta p &= -\frac{1}{v}\frac{d}{db}\int_{-\infty}^{\infty}\frac{Z_1 e^2}{\sqrt{x^2+b^2}}\,dx \\
&= \frac{Z_1 e^2}{vb}\int_{-\infty}^{\infty}\frac{b^2}{\left(x^2+b^2\right)^{3/2}}\,dx \\
&= \frac{Z_1 e^2}{vb}\left[\frac{x}{\sqrt{x^2+b^2}}\right]_{-\infty}^{\infty} \\
&= \frac{2Z_1 e^2}{vb}
\end{aligned}$$

Therefore, energy imparted into the electron is

$$E_{\perp} = \frac{(\Delta p)^2}{2m_e} = \left(\frac{2}{m_e}\right)\left(\frac{Z_1 e^2}{bv}\right)$$